RCA Review

A technical journal published quarterly by RCA Research and Engineering in cooperation with the subsidiaries and divisions of RCA.

Contents

June 1977 Volume 38 Number 2

Cross-polarization Performance of the RCA Satcom System

M. K. Lee

RCA American Communications, Inc., Piscataway, N. J. 08854

Abstract—To significantly increase the efficiency of the available spectrum and the use of the orbital arc, the RCA Satcom system employs the technique known as "Spectrum Reuse," whereby two or more separate channels within the same frequency band are transmitted (or received) on two separate orthogonal linearly polarized beams. Since polarization isolation between the orthogonally polarized beams is not perfect due to various depolarization mechanisms, the desired channel will receive some interference from adjacent cross-polarized channels, causing interference to the desired channel which may result in degraded performance. Since this degradation can not be allowed to compromise the system performance, the amount of interference must be determined so that allowances can be made for its effect on system design. This paper describes the loss of polarization isolation that occurs when a signal travels from transmitter to receiver, with emphasis on the depolarization caused by the propagation medium. A statistical estimation (availability) is made of the overall polarization isolation for various earth station locations throughout the United States. Additionally, some examples of how this isolation is translated into signal interference and then allocated relative to the overall interference to the signal are given.

1. Introduction

An ever increasing requirement for channel capacity in the satellite common carrier band, together with the need to minimize cost, is the reason for employing a spectrum reuse technique. The RCA Satcom System accomplishes this by use of a cross-polarized antenna system to divide the 24 channels into two groups that are carried on two or-

thogonal linearly polarized beams. Each channel is offset 40 MHz from the adjacent copolarized channel, with an interleaving offset of 20 MHz.

This configuration doubles the capacity achieved in 12-channel domestic and international satellite systems over the same allocated 500 MHz band. An ideal doubling of the total information capacity in the given frequency band is based on the assumption that the isolation of the two orthogonal linearly (horizontally and vertically) polarized waves has a value that will result in negligible interference to the cross-polarized channel. Polarization isolation between the orthogonally polarized beams is not perfect in practice due (1) to various depolarization mechanisms caused by system imperfections and (2) to propagation effects that may result in a degradation of performance of the desired channel or a reduction of the channel capacity for a given performance, depending on the severity of depolarization. To meet specified performance objectives, one of three approaches can be taken: (1) a corrective procedure may be incorporated in the system, (2) allowance can be made in the systems margin of performance for depolarization, or (3) a traffic configuration can be established that results in negligible degradations. To evaluate these alternatives, an understanding of the various depolarization mechanisms and the prediction of their magnitudes are essential.

What follows is a description of each of the depolarization mechanisms encountered in the entire transmission system, the prediction of their magnitudes, and an estimation of the overall polarization isolation for various earth-station locations and for different climatological conditions. Based on the predicted cross-polarization isolation, interference from adjacent cross-polarized channels is evaluated for a certain traffic model in order to determine the effect of this interference upon the signal performance.

2. Antenna

2.1 Earth Station Antenna

When a signal propagates between an earth station and a satellite, the earth station or satellite antenna itself is the first source of depolarization. Cross-polarization generated at an earth-station antenna is due to antenna imperfections, and is a function of the basic design of the feed and the sophistication of various add-on circuits. The following factors must be considered:

- TE/TM_{11} cross-polarized lobes as a result of nonsymmetries in the square portion of the feed. This is the main contributor to the generation of cross-polarized radiation, and the major source of this

mode in the feed subsystem is the orthomode transducer (orthocoupler or zero-dB coupler).

- Cross-polarized lobes generated by nonequal amplitude of higher-order modes (such as TE/TM_{12} modes) when a multimode horn is used for optimum excitation of the symmetrical reflector.
- TE_{10} cross-polarized lobes when a horn is fed with the E-field on the diagonal.
- Generation of a cross-polarized component by the curved surface of the reflector.
- Cross-polarization radiation produced by feed support.
- Scattering in a conventional front-fed paraboloid (for front-fed antenna).
- Mechanical disturbance of the antenna or feed (wind, ice, rain, and thermal expansion and contraction).

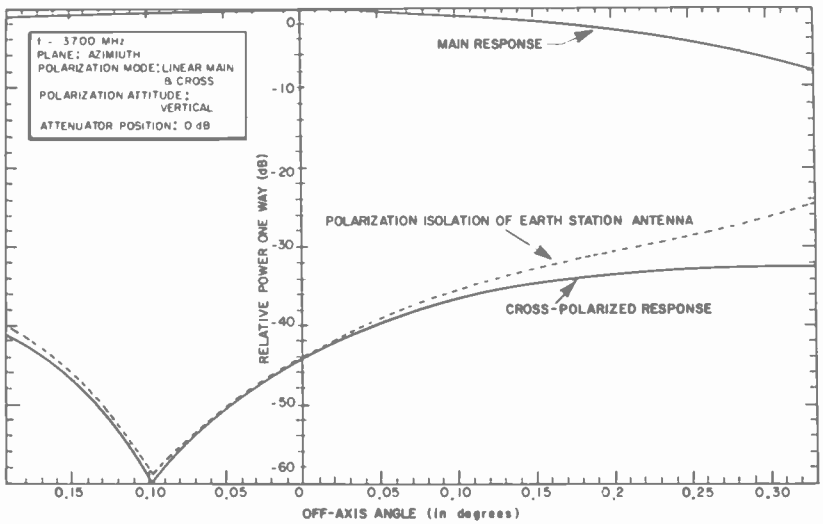

Fig. 1—Secondary patterns measured with 33.3-foot (10-meter) diameter main reflector; 3700 MHz; main and cross polarization, vertical; α = 0 dB main lobe region, θ = 0.

Considering the factors listed above, it is clear that a theoretical prediction[1,2] of antenna performance is of limited value, and measurements must be made. Figs. 1 and 2 are the co- and cross-polarized responses of a typical 10-meter spectrum-reuse antenna at 3.7 GHz and 6.425 GHz, respectively. These are the measured secondary patterns that have been expanded for the range of off-axis angles of interest. The cross-polar-

ization isolation of the earth-station antenna, which is the difference between the main polarized response and the cross-polarized response, is indicated by dotted lines in each figure. As shown in these figures, the polarization isolation of a state-of-the-art earth station antenna is about 40 dB or greater on the main beam axis, and it decreases as the off-axis angle increases. Unequal cross-polarization levels on opposite sides of the antenna axis are due to the way the TE_{10} lobes combine with TE/TM_{11} lobes. The off-axis null of cross-polarized response is generally sensitive to frequency and mechanical stability.

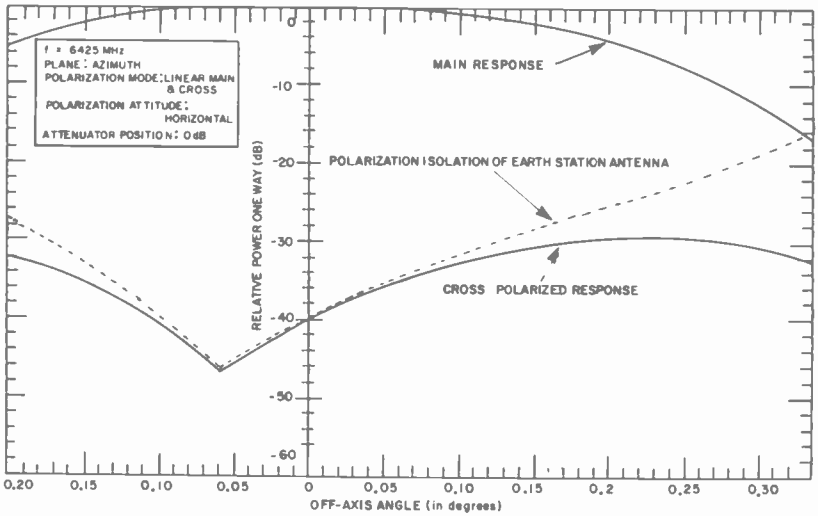

Fig. 2—Secondary patterns measured with 33.3-foot (10-meter) diameter main reflector; 6425 MHz; main and cross polarizations, horizontal; α = 0 dB main reflector region; θ = 0.

Notice that cross-polarization levels in the 4-GHz band are lower than for the 6-GHz band. As a result of this and because the 6-GHz main response decreases more rapidly than 4-GHz response, the cross-polarization isolation at 4 GHz is considerably higher than that at 6 GHz, i.e., 4 dB to 8 dB as the off-axis angle increases. Therefore, the pointing error between the earth station antenna and the spacecraft, which is discussed later, must be calculated in order to determine the magnitude of the cross-polarization isolation.

1.2 Satellite Antenna

The RCA Satcom spacecraft antenna complement consists of four separate grated reflectors overlapping in orthogonally polarized pairs with

offset feed horns mounted on the earth-facing platform. Two of the antennas generate vertically polarized beams and the remaining two antennas produce horizontally polarized beams, each beam providing 8.4° × 3.2° elliptical coverage (of the continental U.S. and Alaska) with the major axis rotated 20.5° with respect to the equatorial plane after achieving proper azimuth and elevation angles. The polarization vector of a horizontally polarized beam is parallel to the major axis of the ellipse.

According to specification, the cross-polarization isolation of the given beam from any other beam that is nominally orthogonally polarized shall be at least 33 dB at any point within the specified coverage of any given beam and at any frequency within the specified frequency band. By proper setting of the *F/D* ratio (focal length/diameter) of the reflector and the amount of offset and by incorporating a polarization filter (filtering screens forming the actual reflecting surface of the antenna) to suppress the unfiltered lobes,[3] an isolation of the order of 39 dB can be achieved, which is more than sufficient to meet the specification.

Table 1—Cross-Polarization Isolation (dB) of the Satellite Antenna (Y_1 horn, N-S Polarization, Satellite at 124°W)

City	Down Link			Up Link		
	3700 MHz	3950 MHz	4200 MHz	5925 MHz	6195 MHz	6425 MHz
	Inside 8.4° × 3.2° Contour					
Boston	43.2	49.0	42.8	33.7	37.6	42.5
New York	43.1	49.9	42.2	33.8	37.1	41.6
Chicago	42.7	45.0	52.5	33.5	33.6	52.3
Denver	36.7	41.6	49.7	36.1	34.6	43.0
San Diego	38.6	37.5	41.9	34.1	34.0	33.1
Los Angeles	39.3	37.8	43.6	35.4	34.5	33.2
San Francisco	43.3	40.8	48.7	36.0	38.4	36.0
Seattle	37.7	39.7	41.5	37.2	45.2	48.4
Prudhoe Bay	35.5	34.3	35.1	42.8	48.8	43.0
	Outside the Contour					
Tampa	36.9	49.5	44.1	39.2	39.4	45.1
King Salmon	39.4	42.1	34.3	40.1	45.9	46.7
Nome	37.5	39.7	34.3	39.2	46.0	46.8

Full spatial cross-polarization measurements made on the breadboard antenna SW (south-west) reflector, "vertical" N-S polarization, (fed by the dual band Y_1 horn) at band center and edges for both bands showed that at cities within the beam coverage the cross-polarization isolation is greater than 33 dB as shown in Table 1. The SW reflector was utilized for the measurements because it is the worst of the four reflectors. The

wide variation in magnitude shown in the table, depending on the frequency and the location, is further confirmed by the measured data on the antenna test range. Fig. 3 shows such a measurement of a vertically polarized beam of the SW reflector of the RCA Satcom F-2 spacecraft taken on an antenna range.[3,4] In-orbit test data[5] has shown a better performance than the range tests, which unavoidably include scatter from near-field surfaces. A two-way link (from South Mountain, L.A. to Vernon Valley, N. J.) demonstrates isolation of greater than 34 dB over the whole 500 MHz on channel 12, which is the channel with the lowest isolation.

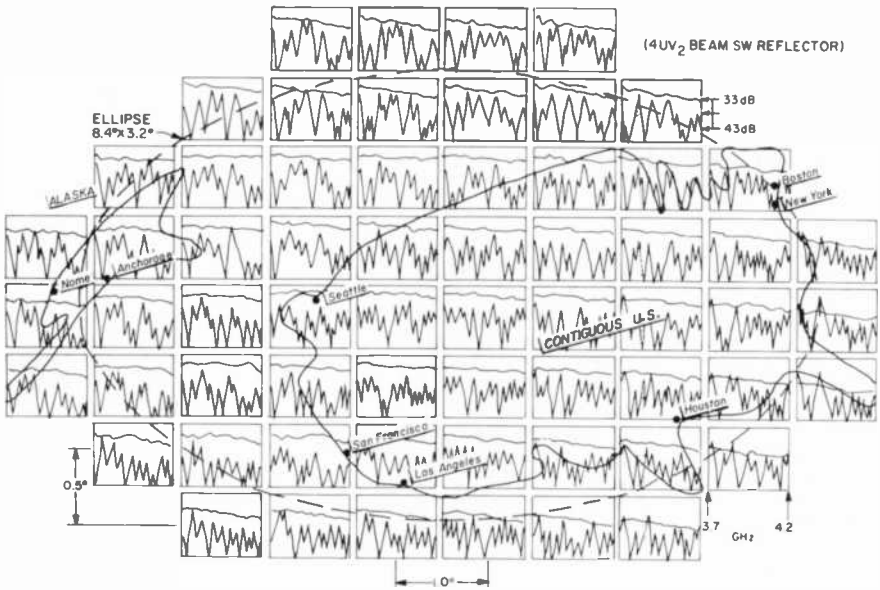

Fig. 3—Measured swept-frequency cross-polarization isolation of an overlapped N-S polarized beam over 8.4 × 3.2° elliptical coverage.

3. Angular Misalignment and Pointing Error

3.1 Angular Misalignment Due to Spacecraft Movement

Movements of the satellite and imperfect pointing to the satellite by ground stations result in off-axis arrival of the signal, causing a loss in gain as well as degradation of the isolation (See Figs. 1 and 2).

Conservative estimates derived from analytical and statistical data indicates that the nominal control maintains the spacecraft within

±0.042° E-W and ±0.069° N-S for approximately 85% of the time (corresponding to normal operation period), whereas the spacecraft is at the specification limit (±0.1° E-W and ±0.1° N-S) for less than 5% of the time (corresponding to the station keeping period). The maximum pointing error (space angle γ shown in Fig. 4) can then be calculated

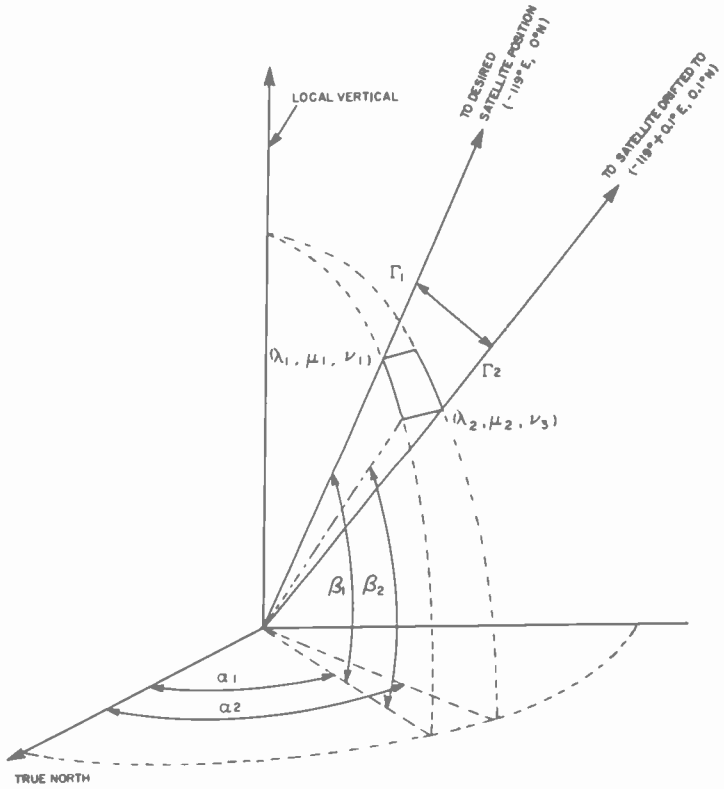

Fig. 4—Pointing error due to spacecraft movement.

using the four corner positions of the spacecraft:

$$\gamma = \cos^{-1}(\lambda_1\lambda_2 + \mu_1\mu_2 + \nu_1\nu_2). \quad [1]$$

Here,

$$\begin{aligned} \gamma &= \text{space angle (pointing error) in degree in Fig. 4} \\ \lambda_1 &= \sin(90 - \beta_1)\cos\alpha_1 \\ \mu_1 &= \sin(90 - \beta_1)\sin\alpha_1 \quad [2] \\ \nu_1 &= \cos(90 - \beta_1) \end{aligned}$$

where α_1, β_1 are the initial azimuth and elevation angles, and

$$\begin{aligned} \lambda_2 &= \sin(90 - \beta_2)\cos\alpha_2 \\ \mu_2 &= \sin(90 - \beta_2)\sin\alpha_2 \\ \nu_2 &= \cos(90 - \beta_2) \end{aligned} \qquad [3]$$

where α_2, β_2 are the azimuth and elevation angles corresponding to the new position of the satellite (one of the four corner positions). (λ_1, μ_1, ν_1) and (λ_2, μ_2, ν_2) are the direction cosines of vectors Γ_1 and Γ_2 as shown in Fig. 4.

The desired location of the satellite is assumed to be (−119°E, 0°N). We substitute α_1, β_1, α_2, and β_2, which are evaluated from a computer program, into Eqs. [1], [2], and [3], and calculate the pointing errors for fifteen earth station locations throughout the United States. The results are summarized in Table 2.

Table 2—Maximum Pointing Error Due to Spacecraft Movement (Assume Initial Operation Has Zero E.S. to S/C Pointing Error) for Several Representative Stations

	Under Normal Operation (85% of the time)*	During Station Keeping (5% of the time)*
Los Angeles	0.1°	0.17°
New York	0.077°	0.14°
Average Station in the 48 Contiguous States	0.092°	0.156°
Average Station in Alaska	0.083°	0.144°
Hawaii	0.084°	0.145°

* For 10% of the time, pointing errors are between the two limits given above.

As can be seen from the table, the pointing errors are different for different earth station locations. Los Angeles shows the largest pointing error, and the pointing error that the New York earth station antenna will experience is small compared to those for other stations. This can easily be understood from the fact that Los Angeles is closer to the satellite than New York and thus, experiences more angle error due to spacecraft movement.

3.2 Earth-Station Pointing Accuracy and Total Pointing Error

Besides the pointing error due to spacecraft movement, there is a pointing error associated with the earth station itself due to various error sources such as gravity, wind, thermal differentials, and foundation displacement. The analysis of this pointing error is beyond the scope of

this paper and accordingly, for the purpose of the analysis, the pointing error that current antenna manufacturers can achieve will be used. A 33.3-foot (10 m) antenna can be installed with an initial pointing accuracy of 0.01° and will maintain its accuracy to within 0.1° in a 60 MPH (96 km/h) wind. For smaller size antennas, the pointing accuracy can be maintained to within 0.2° in an 87 MPH (139 km/h) wind with 0.5 inch (1.3 cm) of ice.

Let θ_1 be the pointing error due to spacecraft movement when the earth station is initially aligned to the desired satellite position (i.e., 119° W, 0° N), and θ_2 the pointing error of the earth station itself with respect to its initial setting due to gravity, wind, and the various other sources of error. Then the combined pointing error can be as high as $\theta_1 + \theta_2$ or as low as the difference between θ_1 and θ_2, depending on the relative movement of the spacecraft and earth station. Based on Table 2, the

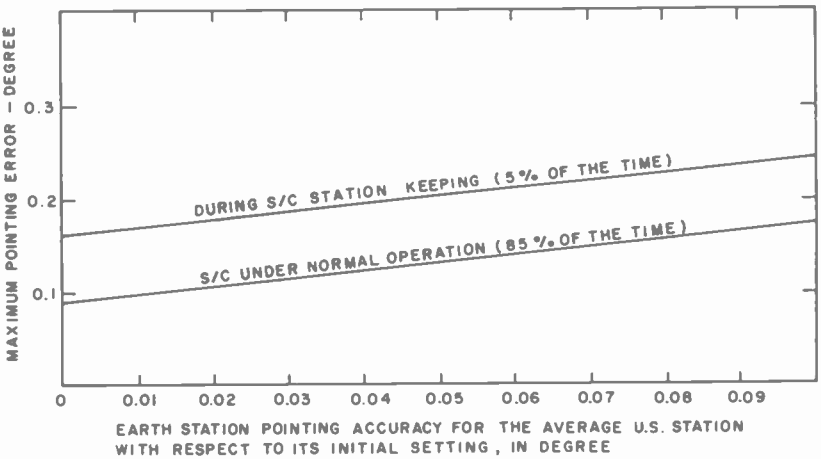

Fig. 5—Maximum pointing error between the earth station antenna and the satellite.

maximum angle error, $\theta_1 + \theta_2$, is shown in Fig. 5 for spacecraft normal operation and for station keeping. The term pointing error as used hereafter in this paper will refer to the combined error.

3.3 Spacecraft Pointing Error

Even though the polarization vector of the earth-station antenna is initially aligned to that of the satellite antenna, without assuming any effects caused by the propagation medium, two polarization vectors can be misaligned due to the movement of the spacecraft about its yaw axis. Pitch and roll angle errors of the spacecraft merely cause a slight shift of the beam in east-west and north-south direction, respectively, but yaw

error causes a rotation of the beam. This rotation causes the polarization vector of the spacecraft antenna to be misaligned relative to the polarization vector of the earth-station antenna. Therefore, polarization isolation on the link can be degraded depending on the magnitude of the yaw error of the spacecraft.

Analysis indicates that the yaw angle error is of the order of ±0.25° under normal operation. This corresponds to a cross-polarization isolation of 45.6 dB (±0.3°). However, when the Faraday rotation angle (rotation due to the ionisphere) is taken into consideration, we find that

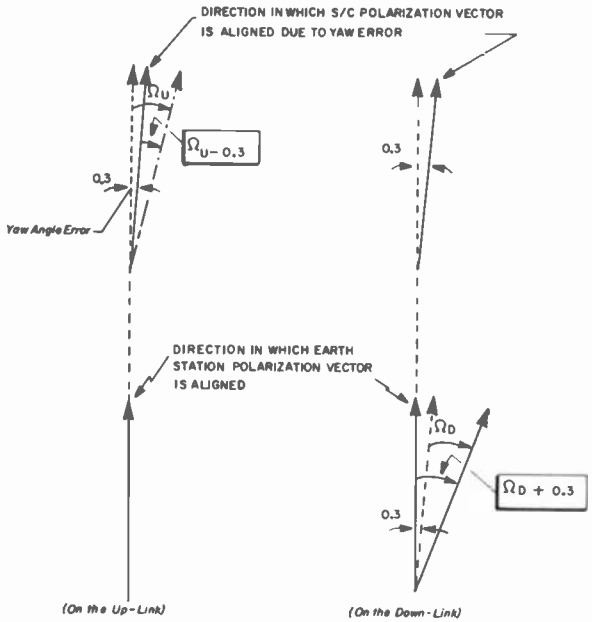

Fig. 6—Effective rotation angle of the polarization vector (as viewed from the spacecraft) when the spacecraft experiences yaw angle error.

the yaw angle error effectively decreases the Faraday rotation of the polarization vector on the uplink, while it increases it on the downlink (or vice versa). Assume that the uplink Faraday rotation angle is Ω_U and the downlink Faraday rotation angle is Ω_D. Then, for a yaw error of ±0.3, the uplink polarization rotation angle becomes $\Omega_U \pm 0.3$ while the rotation angle on the downlink becomes $\Omega_D \mp 0.3$, depending on the direction of the spacecraft movement about the yaw axis as shown in Fig. 6. Thus, yaw-angle error effectively decreases the polarization isolation on one link while it increases the polarization isolation on the other. An example

Table 3—Numerical Example to Show the Effect of Yaw Angle Error

No Yaw Angle Error	
$\Omega_U = 1.14°$	34.0 dB (uplink isolation)
$\Omega_D = 2.58°$	26.9 dB (downlink isolation)
	26.12 dB (overall isolation)
Yaw Angle Error of 0.3°	
$\Omega_U - 0.3° = 0.84°$	36.7 dB (uplink isolation)
$\Omega_D + 0.3° = 2.88°$	26.0 dB (downlink isolation)
	25.65 dB (overall isolation)
Yaw Angle Error of −0.3°	
$\Omega_U + 0.3° = 1.44°$	32.0 dB (uplink isolation)
$\Omega_D - 0.3° = 2.28°$	28.0 dB (downlink isolation)
	26.54 dB (overall isolation)

of this is shown in Table 3. The results verify that the effect of yaw-angle error on the overall system polarization isolation is negligible.

4.0 Rain-Induced Depolarization

The propagation medium between the satellite and the earth station can modify the polarization status of the wave. The ionosphere will cause Faraday rotation of the polarization vector. Heavy rain is likely to convert linear polarization to elliptical polarization with a significant cross-polarized component. Atmospheric turbulence and the fluctuation in the angle of arrival also introduce linear cross-polarization, but calculation shows this effect to be negligible.[1] In addition, depolarization due to the propagation medium shows strong time variations, whereas the imperfections in the earth station and the satellite antennas are nearly independent of time.

The effect of rain on polarization is discussed in this section. Faraday rotation is discussed in Section 5.

4.1 Theory

Depolarization due to rain is caused by the non-spherical nature of the rain drop and the geometrical orientation of the rain drop with respect to the incoming field vector of a given polarization.

The incoming linearly polarized field vector can be resolved into two components polarized along the major axis $O\bar{X}$ and the minor axis $O\bar{Y}$ (or $O\bar{C}$ direction for the satellite-earth path with an elevation angle of

β) of the rain drop as shown in Fig. 7. The two components orthogonal to each other will experience different attenuation and different phase shifts relative to each other, due to the nonspherical nature of the raindrop. This effect is measured by two parameters called differential attenuation and differential phase shift, which result in a change of polarization status of the incoming wave depending on how the rain drop is canted with respect to the wave field vector.

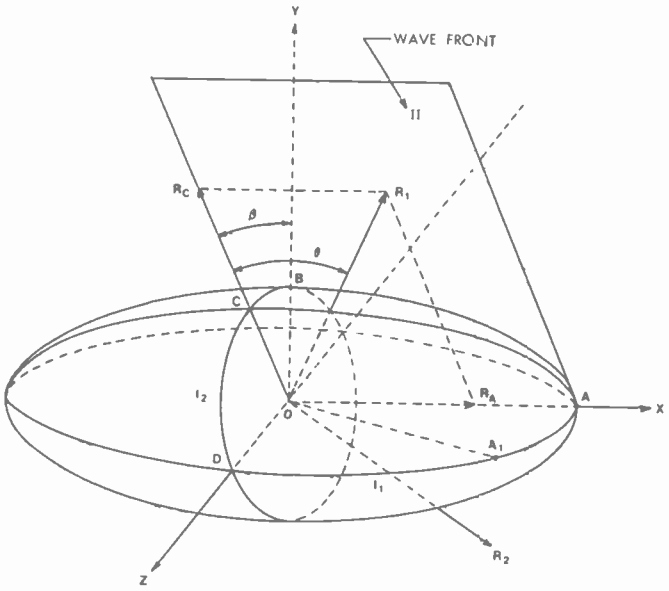

Fig. 7—Geometrical orientation of rain drop with respect to linearly polarized field vectors.

Assume the following geometrical orientation of the rain drop with respect to the polarization vector shown in Fig. 7, where,
$O\vec{Y}$ = Local vertical perpendicular to the ground (XZ plane)
π = wave front inclined by $\beta°$ from XY plane
β = elevation angle
$O\vec{B}$ = minor axis of the horizontally disposed spheroidal rain drop. Therefore, $\overline{OB}$ is the shortest distance from the center of the rain drop.
$O\vec{A}$ = major axis of the horizontally disposed spheroidal rain drop. Therefore, $\overline{OA}$ is the longest distance from the center of the rain drop.
l_1 = circular contour made cutting the rain drop horizontally. Therefore,

$\overline{OA} = \overline{OA}_1$. $O\vec{A}_1$ can also be a major axis, but assume $O\vec{A}$ as the major axis for the purpose of this discussion.
l_2 = elliptical contour made by cutting the rain drop perpendicularly to the XY plane. Therefore, $\overline{OB} < \overline{OC} < (\overline{OD} = \overline{OA}_1$ or $\overline{OA})$
R_1 = one of the two linear orthogonally polarized wave vectors, R_1 and R_2.
R_C = component vector of R_1 resolved in $O\vec{C}$ direction.
R_A = component vector of R_1 resolved in $O\vec{A}$ direction.
θ = angle between vector R_1 and R_C. It will be called canting angle hereafter.

As outlined in Appendix 1, the differential attenuation causes the original linearly polarized field vector, R_1, to rotate from its original attitude. The angle of rotation, δ, is

$$\delta = \theta - \tan^{-1}\left(\tan\theta \cdot \log^{-1}\left[\frac{-(\alpha'_A - \alpha'_C)L}{20}\right]\right)$$

where,

θ = canting angle defined in Fig. 7.
$\alpha'_A - \alpha'_C$ = differential attenuation in [dB/km], α'_A and α'_C are attenuation coefficients [dB/km] of the waves polarized along the $O\vec{A}$ and $O\vec{C}$ directions.
L = effective rain path length

For frequencies of 4 and 6 GHz, the cross-polarization generated by angle δ is negligible. In this frequency range, the effect of differential phase shift is more important. The differential phase shift converts the linear polarization of the original wave into elliptical polarization. At the same time, the major axis of the polarization ellipse rotates relative to the original attitude of the linearly polarized field vector. This is shown in Fig. 8. The axial ratio and δ are as follows (also see Appendix 1):

$$\delta = \theta + \frac{1}{2}\tan^{-1}\left[\frac{2\cot\theta\cos\phi}{1 - \cot^2\theta}\right] - 90° \qquad [5]$$

$$\text{AR} = \text{Major Axis/Minor Axis}$$

$$= \tan\left[\frac{1}{2}\sin^{-1}(\pm \sin 2\theta \sin\phi)\right] \qquad [6]$$

where,

$\phi = (\beta_A - \beta_C)L$, differential phase shift through the effective rain path length, L. β_A and β_C are the phase shifts in deg/km of the waves polarized along $O\vec{A}$ and $O\vec{C}$ direction.

For AR > 1, $90° \leq \sin^{-1}(\sin 2\theta \sin\phi) \leq 180°$.

Since δ, in this case, is extremely small in the frequency range of interest, the major effect of the differential phase shift is the conversion of linear polarization to elliptical polarization with a significant cross-polarized component depending on rainfall rate. The cross-polarization isolation then is expressed as

$$XPI = 20 \log AR \text{ [dB]} \qquad [7]$$

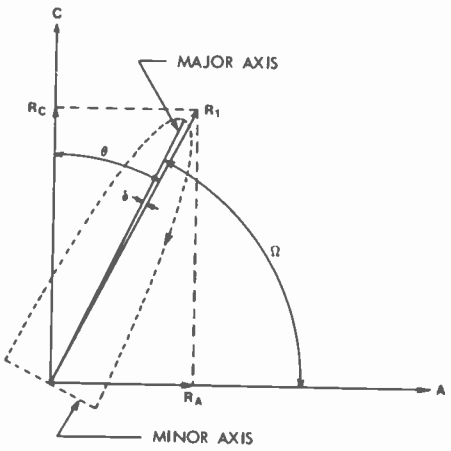

Fig. 8—Axial ratio deterioration due to differential phase shift.

4.2 Prediction

If the elevation angle is not zero, the differential phase shift to be used in Eqs. [5] and [6] is $\beta_A - \beta_C$ [deg/km]. Limited data for this case is available. However, the data for $\beta_A - \beta_B$, which is the phase difference between components of the field vector polarized along the major axis and the minor axis of the rain drop, is available from perturbation calculations and point-matching procedure.[6-8] Results from Oguchi are reproduced in Fig. 9.[9] Since $(\beta_A - \beta_B)$ is greater than $(\beta_A - \beta_C)$, the worst-case results are predicted using $\beta_A - \beta_B$, even though there exists an approximate relationship[10] such as $\beta_A - \beta_C = (\beta_A - \beta_B) \sin^2(90 - \beta)$.

The effect of canting angle distribution on the resultant cross-polarized signal strength is also taken into consideration. The canting angle distribution measured by Saunders[11] was assumed around $\theta_C = 20°$, $\theta_C = 30°$, and $\theta_C = 45°$ (note that Saunders' distribution was centered at zero degrees, but the same distribution is assumed to be centered at 20°, 30°, and 45° in this analysis). In this case, Eq. [6] becomes

$$AR = \tan\left[\frac{1}{2}\sin^{-1}\left(\pm\sum_i f_i \sin 2\theta_i \sin\phi\right)\right] \quad [8]$$

where f_i is the fraction of the nonspherical drops having canting angle θ_i, and $\sum_i f_i = 1$.

The effective rain path length, L, is assumed to be related to the rainfall rate as follows:

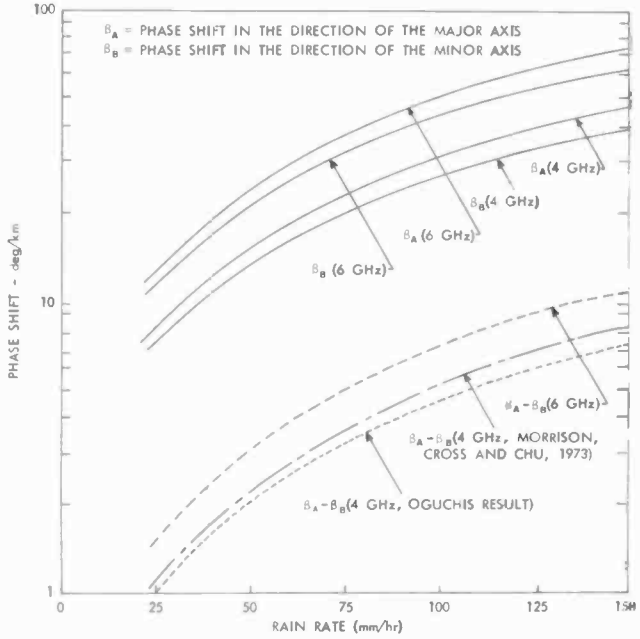

Fig. 9—Phase shift versus rain rate.

$$\text{Vertical Extent} = 5.34 - 1.67 \log P \text{ [km]}$$
$$\text{Horizontal Extent} = 17.18 - 5.13 \log P \text{ [km]} \quad [9]$$

where P is rain rate in mm/hr, the statistics of which are shown[12] in Figs. 10 and 11.

The cross-polarization isolations thus calculated are shown in Figs. 12 and 13 for 4 and 6 GHz, respectively. When Saunders' canting angle distribution is used in the calculation, the canting angle distribution around $\theta_C = 30°$ gave a worse result than that for the canting angle distribution around $\theta_C = 45°$, while constant canting angle $\theta = 30°$

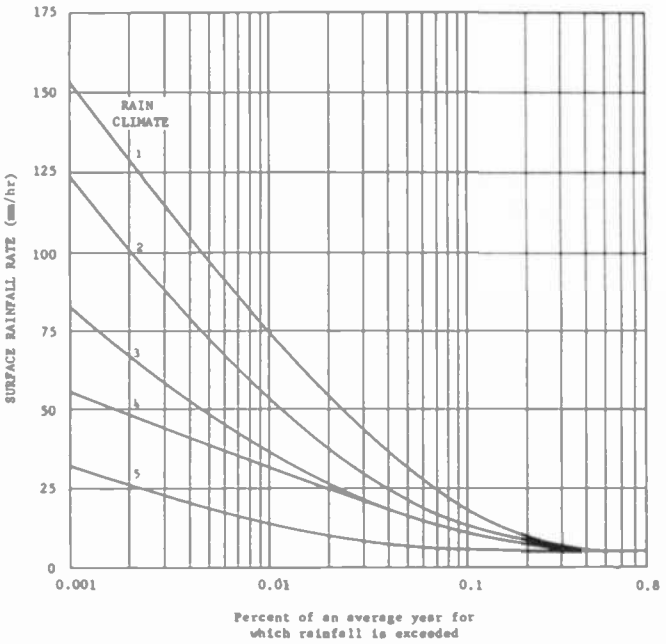

Fig. 10—Rainfall versus time curves.

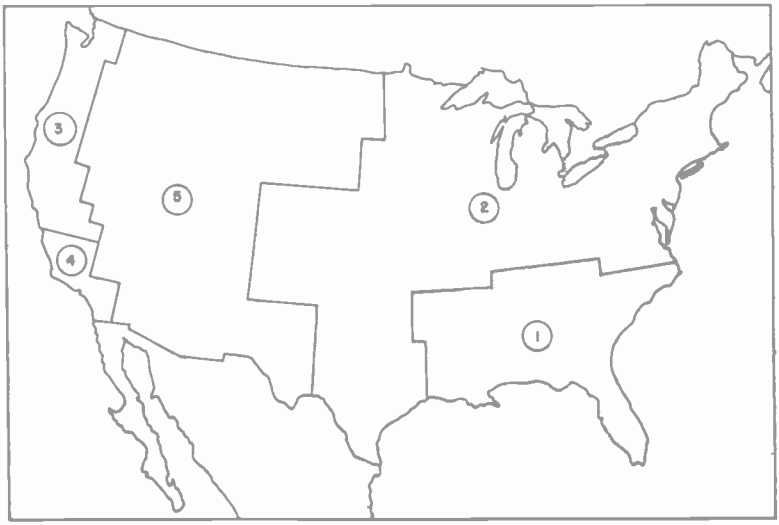

Fig. 11—Rain climates of the United States.

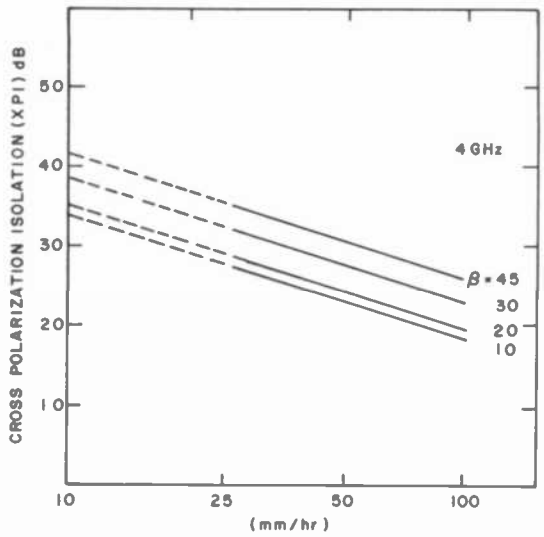

Fig. 12—Depolarization caused by differential phase shift for the distribution of canting angles around $\theta_c = 30°$ (4 GHz).

yielded a better result[6] than that for $\theta = 45°$. This is due to the assumed distribution of the canting angle. Since contributions from positive and negative canting angles cancel ($\sin 2\theta_i$ changes sign), the resultant cross-polarization isolations for the canting angle distribution around

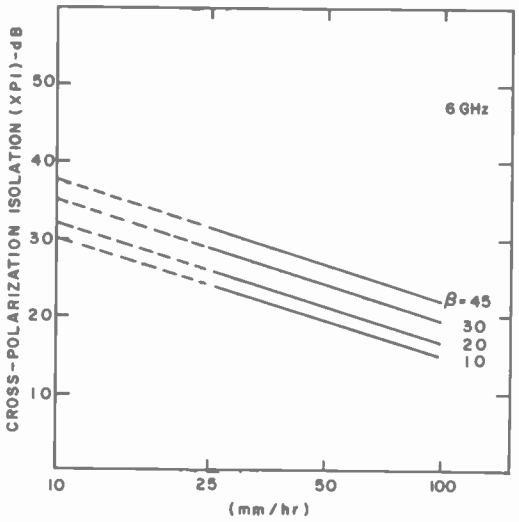

Fig. 13—Depolarization caused by differential phase shift for the distribution of canting angles around $\theta_c = 30°$ (6 GHz).

$\theta_C = 30°$ are improved by approximately 6 dB from those for the constant angle distribution $\theta = 30°$. The estimated cross-polarization isolations for various earth-station locations throughout the United States are also tabulated in Table 4.

5. Faraday Rotation

5.1 Theory

When a linearly polarized radio wave is incident upon a homogeneous anisotropic ionized medium, such as the ionosphere, it splits into two characteristic waves (or modes), the ordinary and extraordinary waves of the magneto-ionic theory. These waves are generally elliptically polarized with opposite senses of rotation and travel independently with different phase velocities. For a sufficiently high frequency (i.e., a wave frequency much larger than the plasma, collision, and gyromagnetic frequencies) and a direction of propagation that is not too nearly normal to the magnetic field (quasi-longitudinal approximation), these waves will be nearly circularly polarized. They also have complex, anisotropic,

Table 4—Estimated Cross-polarization Isolation for Various U.S. Sites Due to Rain (Distribution of Rain Drop Canting Angles Assumed)

Category	Site	β	4 GHz 0.01%	4 GHz 0.1% (dB)	4 GHz 1%	6 GHz 0.01%	6 GHz 0.1% (dB)	6 GHz 1%
2	Boston	21.58	24.5	34.1	40.5	21.2	30.5	37.2
2	New York	24.50	25.5	35.1	41.4	22.1	31.4	38.2
2	Houston	46.72	30.6	39.9	46.3	26.5	36.1	42.6
2	Chicago	32.16	27.8	37.3	43.0	24.1	33.5	40.3
2	Denver	41.79	29.6	39.0	45.4	25.7	35.2	41.8
4	San Diego	51.87	34.9	41.7	47.4	30.8	37.8	43.4
4	Los Angeles	50.47	34.6	41.4	47.1	30.5	37.5	43.1
3	San Francisco	46.10	32.9	40.6	46.2	28.8	36.8	42.5
3	Seattle	35.22	30.8	38.6	44.0	26.9	34.9	40.8
1	Tampa	38.37	26.7	36.9	44.7	22.8	33.2	41.3
Average (Canting Angle Distribution)			29.7	38.5	44.6	25.9	34.7	41.1
Average (Constant Canting Angle). . . .			23.7	32.5	38.6	19.9	28.7	35.1

refractive indices, i.e., they are absorbed as they propagate, and for neither characteristic wave do the wave-normal and ray directions coincide. Since the refractive indices are different, i.e., the two components have different phase velocities, the plane of polarization of the resultant wave field gradually rotates as the wave progresses through the ionosphere. This phenomenon is known as the ionospheric Faraday rotation.

If the wave frequency is much higher than the plasma frequency and gyromagnetic frequency (above 100 MHz), both ordinary and extraordinary rays can be assumed identical to a straight line joining the transmitter and receiver (first-order approximation). To a first-order approximation, the angle between the ray and the wave normal is also approximately equal to zero. In this case, the Faraday rotation in radians is expressed by[13, 14]

$$\Omega = 2.365 \times 10^4 f^{-2} \int N(B \cos\theta) ds \qquad [10]$$

or

$$= 2.97 \times 10^{-2} f^{-2} \int N(H \cos\theta) ds$$

where

f = wave frequency, Hz,
N = electron density, electrons/m^3
B = magnetic flux density, Wb/m^2 = $\mu_0 H$
$\mu_0 = 1.257 \times 10^{-6}$ henry/m
H = magnetic field intensity, ampere-turns/m
θ = angle between the wave normal and the geomagnetic field vector.
s = ray-path length, meters

Thus, the rotation of the plane of polarization is proportional to the product of the electron content and the magnetic field component along the path of ray propagation and inversely proportional to the square of the radio frequency.

For convenience, Eq. [10] can be written in terms of a differential length of height h above the earth instead of an element of ray-path lengths. Thus, from Fig. 14,

$$\Omega = \frac{2.365 \times 10^4}{f^2} \int_0^{h_t} (B \cos\theta) \csc(\zeta + \beta) N(h) dh \qquad [11]$$

$$= \frac{2.365 \times 10^4}{f^2} \int_0^{h_t} \Psi(h, \Gamma) N(h) dh$$

$$= \frac{2.365 \times 10^4}{f^2} \Psi(h_m, \Gamma) \int_0^{h_t} N(h) dh$$

where

$$\Psi(h_m, \Gamma) = \frac{\int_0^{h_t} N(h) \Psi(h, \Gamma) dh}{\int_0^{h_t} N(h) dh}$$

and h_m is some intermediate value of height between zero and h_t, called "mean ionospheric height." $B\cos\theta\csc(\zeta+\beta)$ calculated at this mean ionosphere height approximates the weighted mean value of the product $B\cos\theta\csc(\zeta+\beta)$ over the signal path for targets beyond the ionosphere. The mean height of the ionosphere is normally assumed to be around 340 to 400 km, which is near the centroid of the electron

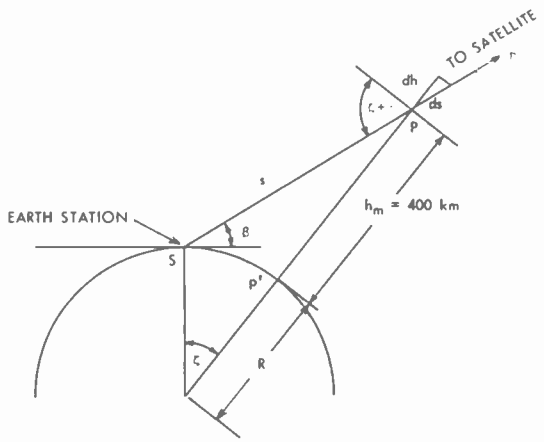

Fig. 14—Ray path geometry.

concentration distribution. Then Eq. [11] becomes

$$\Omega = \frac{2.365 \times 10^4}{f^2}\,\Psi(400, \Gamma)\int_0^{h_t} N dh \qquad [12]$$

where 400 km is taken as the mean height.

The sense of polarization rotation of the wave as it travels toward the satellite is CCW and as it travels toward the earth station is CW. Viewed from the receiving end, obviously, the sense of rotation of the wave is reversed, i.e., viewed from the earth station it is CCW and from the satellite it is CW.

5.2 Prediction

Using the theoretical ionospheric model available,[15,16] the integrated electron density, $\int N(h)dh$ (usually called electron content or columnar electron content, electrons/m^2 column) was predicted for various locations, time of the day, season of the year, and solar activity. It is important to note that the behavior of the Faraday rotation angles follows exactly that of the electron content. One example of such predictions

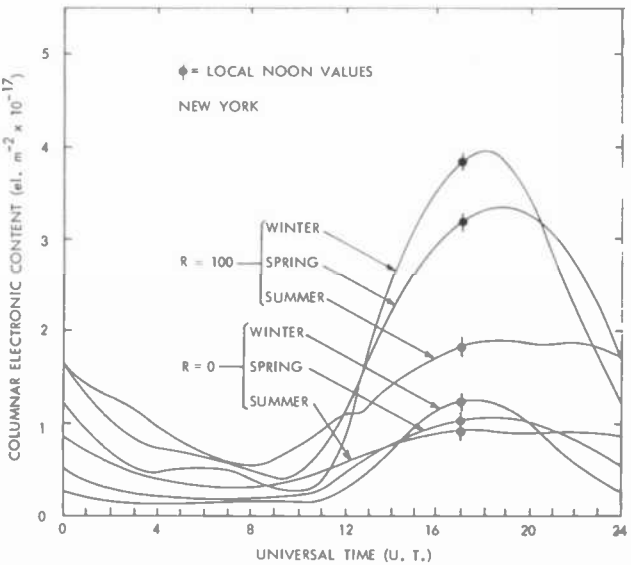

Fig. 15—Diurnal, seasonal, and solar cycle variations of the electron content at New York.

is shown in Fig. 15 for an earth station in New York. The $\Psi(400, \Gamma)$ function is also evaluated, as shown in Appendix 2, for various earth-station locations using the earth's magnetic field model described by Jensen and Cain[17] and Chapman and Bartels.[18] The Ψ function evaluated in Appendix 2 is shown in Table 5. With this Ψ function and the electron content predicted by the theoretical ionospheric model, the

Table 5—Calculations of $\Psi(400,\Gamma)$ for Various Earth Station Sites (For Satellite at 119°W)

Station	β	ζ	$\cos\theta$	B (in 10^{-4} Wb/m^2)	$\Psi(400, \Gamma)$ (in 10^{-4} Wb/m^2)
Boston	21.58	7.3717	−0.612	0.47	0.594
New York	24.50	6.6007	−0.659	0.46	0.587
Houston	46.72	3.1063	−0.943	0.41	0.506
Chicago	32.16	5.0328	−0.802	0.47	0.623
Denver	41.79	3.6551	−0.945	0.45	0.597
San Diego	51.87	2.6084	−0.996	0.40	0.490
Los Angeles	50.47	2.7373	−0.993	0.40	0.496
San Francisco	46.10	3.1710	−0.965	0.42	0.535
Seattle	35.22	4.5398	−0.866	0.46	0.623
Juneau	22.26	7.1814	−0.693	0.47	0.663
Hawaii	38.36	4.0912	−0.522	0.31	0.240

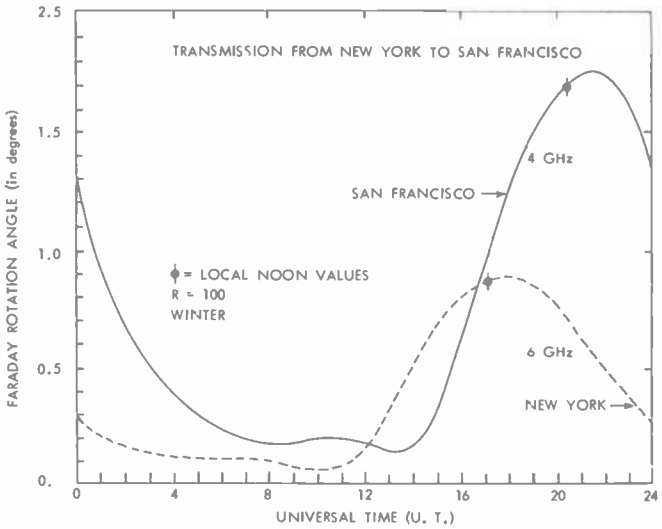

Fig. 16—Faraday rotation angles for the transmission path from New York to San Francisco for winter solstice in the year of sunspot maximum.

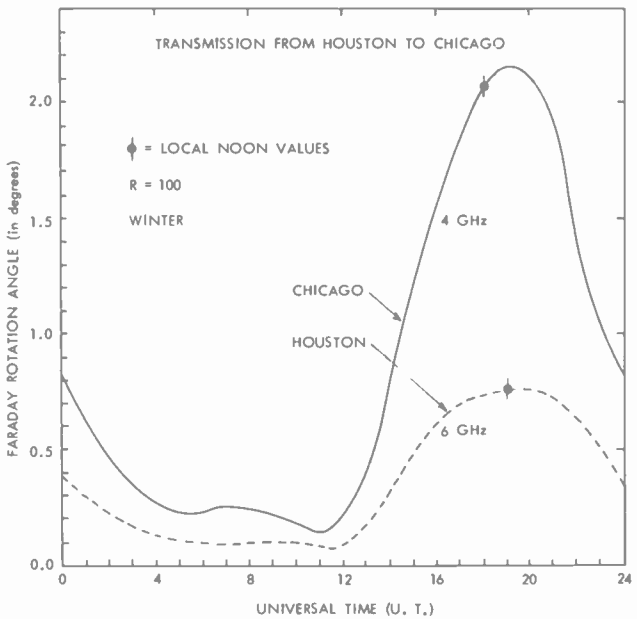

Fig. 17—Faraday rotation angles for the transmission path from Houston to Chicago for winter solstice in the year of sunspot maximum.

Faraday rotation angle can be calculated. Figs. 16 and 17 are some of the results of the model calculations for transmission paths between New York–San Francisco and Chicago–Houston. These predictions were made for winter in a year of high solar activity (Wolf sunspot number, $R = 100$).

It is important to make an estimation of the maximum or minimum values of the Faraday rotation angles for the system design so that proper compensation techniques can be implemented or allowances can be made for its effect in the system design. In order to predict the magnitude of Faraday rotation angles, the solar activity in the year of interest must first be predicted. Fig. 18 shows the predicted sunspot numbers for solar

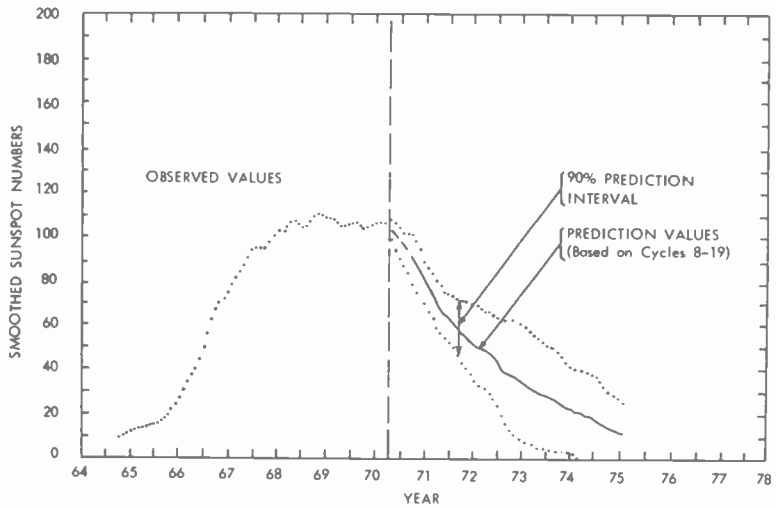

Fig. 18—Predicted sunspot numbers for cycle 20.

cycle 20. This prediction made by the Ionospheric Propagation Prediction Group of ITS, ESSA Research Laboratories, is derived from a regression analysis based on the previous solar cycle.[19] The maximum of the next cycle will be expected to occur somewhere around 1980 with the sunspot number $R \approx 100$ or above. Therefore, in years around 1980 the Faraday rotation angle will also show its maximum value throughout the solar cycle. Table 6 shows the daytime maximum and nighttime minimum values of the Faraday rotation angles at 4 GHz for three seasons and two solar activities. The results shown in this table are for the mean variations of the electron content for one month. If these monthly

mean values of electron content are assumed to be exceeded by 20% on a particular day of the month for various reasons, such as magnetic storm and solar flare effect, the corresponding mean values of the Faraday rotation will also be exceeded by 20%. The Faraday rotation angle at 6 GHz is 0.40629 times the 4-GHz rotation based on the frequency dependence, $(1/f^2)$.

Cross-polarization isolation (XPI) due to the Faraday rotation effect is then defined as follows:

Table 6—Daytime Maximum and Nighttime Minimum Values of the Mean Faraday Rotation Angle, Ω (in degrees) at 4 GHz (Satellite at 119° W)

Station	$R = 0$		$R = 100$	
	Daytime Max. Ω	Nighttime Min. Ω	Daytime Max. Ω	Nighttime Min. Ω
		Spring Equinox		
Boston	0.53	0.11	1.70	0.22
New York	0.53	0.11	1.68	0.22
Houston	0.74	0.15	2.04	0.28
Chicago	0.56	0.11	1.78	0.35
Denver	0.62	0.15	1.89	0.27
San Diego	0.66	0.16	1.94	0.28
Los Angeles	0.67	0.16	1.96	0.29
San Francisco	0.63	0.16	1.89	0.27
Seattle	0.53	0.11	1.63	0.22
Juneau	0.24	0.05	1.31	0.15
Hawaii	0.87	0.07	1.72	0.12
		Summer Solstice		
Boston	0.47	0.18	0.95	0.29
New York	0.47	0.18	0.94	0.28
Houston	0.59	0.17	1.23	0.34
Chicago	0.49	0.18	0.98	0.28
Denver	0.51	0.19	1.05	0.30
San Diego	0.51	0.18	1.14	0.32
Los Angeles	0.52	0.18	1.15	0.33
San Francisco	0.50	0.19	1.10	0.33
Seattle	0.47	0.20	0.94	0.31
Juneau	0.47	0.22	0.87	0.33
Hawaii	0.62	0.09	1.24	0.20
		Winter Solstice		
Boston	0.63	0.07	2.00	0.16
New York	0.62	0.07	1.98	0.15
Houston	0.63	0.12	1.73	0.18
Chicago	0.66	0.07	2.15	0.23
Denver	0.65	0.10	2.03	0.15
San Diego	0.55	0.10	1.62	0.16
Los Angeles	0.56	0.11	1.64	0.16
San Francisco	0.56	0.10	1.74	0.15
Seattle	0.58	0.04	1.99	0.09
Juneau	0.49	0.02	1.77	0.07
Hawaii	0.58	0.06	1.26	0.09

$$\text{XPI} = 10 \log \left(\frac{\text{received power polarized orthogonally to the transmitted power}}{\text{received power polarized in the same sense as the transmitted power}} \right)$$

$$= 20 \log \left(\frac{|\vec{E}| \sin\Omega}{|\vec{E}| \cos\Omega} \right)$$

$$\approx 20 \log(\sin\Omega), \text{ for small } \Omega$$

where $\vec{E}$ is the original transmitted E field vector.

Based on Table 6, the daytime minimum and nighttime maximum values of the cross-polarization isolation, XPI, at 4 and 6 GHz are shown in Tables 7 and 8, respectively.

6. Overall Cross-polarization Isolation and Its Effect on Signal Performance

6.1 Overall Cross-polarization Isolation

Cross-polarization is the transfer of energy from one state of polarization to the other orthogonal state. Therefore, summation of cross-polarization is carried out in terms of the total transmission loss of the desired signal due to depolarization.

For the purpose of this discussion, it is assumed that the original E field vector rotates by $\alpha°$ (see Fig. 19) at the first cross-polarizing stage

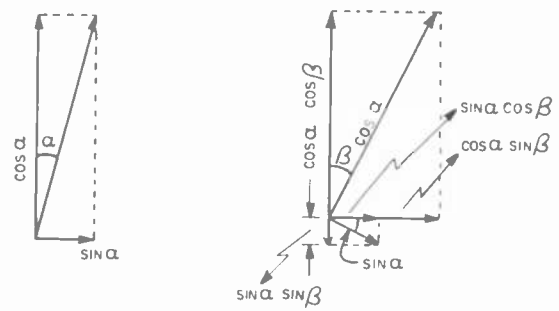

Fig. 19—Geometry of co-polar and cross-polar electric field as the wave passes each cross-polarizing stage.

Table 7—Daytime Minimum and Nighttime Maximum Values of the Cross-Polarization Isolation, XPI (in dB) at 4 GHz if Feed is Set Up for Free Space Condition

	XPI (dB) for $R = 0$				XPI (dB) for $R = 100$			
	Daytime Min.		Nighttime Max.		Daytime Min.		Nighttime Max.	
Station	Mean	20% above Mean	Mean	20% above Mean	Mean	20% above Mean	Mean	20% above Mean
				Spring				
Houston	37.8	36.2	51.6	50.1	29.0	27.4	46.2	44.5
Average over 48 states	39.5	37.9	52.2	50.1	29.9	28.3	46.5	45.1
Juneau	47.6	45.9	61.2	59.6	32.8	31.2	51.6	50.1
Hawaii	36.4	37.8	58.3	57.1	30.5	28.9	53.6	52.2
				Summer				
Houston	39.7	38.1	50.6	49.1	33.4	31.8	44.5	42.9
Average over 48 states	41.2	39.6	50.1	48.3	34.7	33.2	45.3	43.8
Juneau	41.7	40.2	48.3	46.9	36.4	34.8	44.8	43.1
Hawaii	39.3	37.8	56.1	54.3	33.3	31.7	49.1	47.6
				Winter				
Chicago	38.8	37.2	58.3	57.1	28.5	26.9	47.9	46.2
Average over 48 states	39.6	38.0	58.3	57.1	29.7	28.1	51.1	49.6
Juneau	41.4	39.7	69.1	69.1	30.2	28.6	58.3	57.1
Hawaii	39.9	38.3	59.6	58.3	33.2	31.6	56.1	54.3

Table 8—Daytime Minimum and Nighttime Maximum Values of the Cross-Polarization Isolation, XPI (in dB) at 6 GHz if Feed is Set Up for Free Space Condition

Station	XPI (dB) for R = 0				XPI (dB) for R = 100			
	Daytime Min.		Nighttime Max.		Daytime Min.		Nighttime Max.	
	Mean	20% above Mean	Mean	20% above Mean	Mean	20% above Mean	Mean	20% above Mean
				Spring				
Houston	44.8	43.1	58.3	57.1	36.0	34.4	52.9	51.1
Average over 48 states	46.5	45.1	59.6	58.3	37.0	35.4	53.6	52.2
Juneau	49.6	47.9	69.1	69.1	39.9	38.3	58.3	57.1
Hawaii	43.6	41.9	65.6	63.1	37.5	36.0	59.6	58.3
				Summer				
Houston	46.9	45.3	57.1	55.2	40.4	38.8	51.6	50.1
Average over 48 states	48.3	46.9	57.1	55.2	41.7	40.2	52.2	50.6
Juneau	48.7	47.2	55.2	53.6	43.3	41.7	51.6	50.1
Hawaii	46.2	44.5	63.1	61.2	40.4	38.8	56.1	54.3
				Winter				
Chicago	45.6	44.0	65.6	63.1	35.6	34.0	59.6	58.3
Average over 48 states	46.5	45.1	63.1	61.2	36.8	35.2	58.3	57.1
Juneau	48.3	46.9	75.2	75.2	37.2	35.6	65.6	63.1
Hawaii	46.9	45.3	65.6	63.1	40.2	38.6	63.1	61.2

(i.e., where only rain-induced differential attenuation is considered) and further rotates by $\beta°$ at the second cross-polarizing stage, such as the Ionosphere. Then the cross-polarization isolations at the first and the second stages are expressed as follows:

$$(\mathrm{XPI})_1 = 20 \log \frac{\cos\alpha}{\sin\alpha} = 29.14 \text{ dB, assuming } \alpha = 2° \qquad [13]$$

$$(\mathrm{XPI})_2 = 20 \log \frac{\cos\beta}{\sin\beta} = 25.61 \text{ dB, assuming } \beta = 3° \qquad [14]$$

The overall cross-polarization isolation is calculated to be (see Fig. 19)

$$(\mathrm{XPI})_{\text{total}} = 20 \log \left(\frac{\text{Resultant } E \text{ vector component polarized in the desired direction}}{\text{Resultant } E \text{ vector component polarized perpendicular to the desired direction}} \right)$$

$$= 20 \log \left(\frac{\cos\alpha \cos\beta - \sin\alpha \sin\beta}{\cos\alpha \sin\beta + \sin\alpha \cos\beta} \right) \qquad [15]$$

$$= 20 \log \frac{0.9962}{0.0872} = 21.16 \text{ dB}$$

Eq. [15] is exactly equal to $20 \log[\cos(\alpha + \beta)/\sin(\alpha + \beta)]$, that is, $20 \log(\cos 5°/\sin 5°)$ if the original vector rotates by 5° from its original attitude.

Since $\sin\alpha \sin\beta$ is much less than unity, Eq. [15] can be approximated as

$$(\mathrm{XPI})_{\text{total}} \approx 20 \log \left(\frac{\cos\alpha \cos\beta}{\cos\alpha \sin\beta + \sin\alpha \cos\beta} \right)$$

$$= 20 \log \left(\frac{\sin\alpha}{\cos\alpha} + \frac{\sin\beta}{\cos\beta} \right)^{-1}$$

$$= 20 \log (10^{-(\mathrm{XPI})_1/20} + 10^{-(\mathrm{XPI})_2/20})^{-1} \qquad [16]$$

which is the expression for the voltage summation of $(\mathrm{XPI})_1$ and $(\mathrm{XPI})_2$. Thus, for N cross-polarization stages, each characterized by an isolation $(\mathrm{XPI})_i$ of the wanted polarization, the total cross-polarization is given by the voltage summation of $(\mathrm{XPI})_i$:

$$(\mathrm{XPI})_{\text{total}} = 20 \log (10^{-(\mathrm{XPI})_1/20} + 10^{-(\mathrm{XPI})_2/20} + \ldots 10^{-(\mathrm{XPI})_N/20})^{-1} \qquad [17]$$

Since the characteristic of each cross-polarizing stage is different from others in practice, the way E vectors are added together as the signal travels through various cross-polarizing stages is a complicated problem. However, the worst situation described above can be evaluated using Eq. [17] to determine the total cross-polarization isolation.

As examples of such calculations of cross-polarization on an up or down link, two cases are presented below. One case is for a pointing error 0.1°, and the other for 0.2° for the determination of the cross-polarization isolation of an earth station 10-m antenna. As discussed in Section 3, 0.1°

Table 9—Uplink and Downlink Cross-polarization Isolations As a Function of % Time Availability and the Earth Station Location (Pointing Error of 0.1° was Assumed)

		99%		99.9%		99.99%	
		Up-link	Down-link	Up-link	Down-link	Up-link	Down-link
Zone 1	Tampa & Memphis	22.53	21.44	21.12	20.61	17.17	18.05
	Willmington	22.38	21.33	20.66	20.29	16.47	17.47
Zone 2	Boston	21.95	21.07	20.36	20.12	16.30	17.17
	New York	22.12	21.17	20.63	20.31	16.77	17.59
	Houston	22.68	21.54	21.75	21.01	18.91	19.30
	Chicago	22.41	21.31	21.19	20.67	17.83	18.44
	Denver	22.59	21.48	21.57	20.90	18.57	19.01
Zone 3	San Francisco	22.67	21.53	21.88	21.09	19.80	19.86
	Seattle	22.48	21.39	21.51	20.85	19.07	19.35
Zone 4	Los Angeles & San Diego	22.73	21.58	22.00	21.17	20.36	20.22
Zone 5	Phoenix	22.76	21.58	22.61	21.52	21.86	21.09
	Salt Lake City	22.61	21.49	22.45	21.42	21.57	20.91
	Moscow	22.49	21.42	22.32	21.33	21.33	20.77

is the maximum pointing error that can be experienced during the normal operation of the spacecraft when the earth station maintains a pointing accuracy of 0.01° with respect to its initial setting. 0.2° is the maximum pointing error when the earth station maintains an initial pointing accuracy of 0.04° during spacecraft station keeping.

The case for the clear weather condition is considered first, and then results are modified to include the rain depolarization effect as a function of availability and the earth-station locations as shown in Tables 9 and 10. The worst-case Faraday rotation (winter or fall daytime maximum value of the Faraday rotation angle in the year of maximum solar activity) and a polarization isolation of 33 dB for the satellite antenna were used throughout the calculation. When the duirnal and seasonal variations of the Faraday rotation angle are considered, the availabilities given

in the tables are low, because they represent availability associated with rain statistics and worst-case Faraday Rotation. The overall system cross-polarization isolation can be obtained by combining uplink and downlink polarization isolations via power addition for the satellite link of interest.

Table 10—Uplink and Downlink Cross-polarization Isolations As a Function of % Time Availability and the Earth Station Location (Pointing Error of 0.2° was Assumed)

		99%		99.9%		99.99%	
		Up-link	Down-link	Up-link	Down-link	Up-link	Down-link
Zone 1	Tampa & Memphis	19.82	20.20	18.76	19.48	15.60	17.19
	Willmington	19.70	20.11	18.41	19.19	15.01	16.66
Zone 2	Boston	19.39	19.88	18.18	19.04	14.87	16.39
	New York	19.51	19.96	18.39	19.21	15.27	16.77
	Houston	19.92	20.28	19.24	19.82	17.03	18.31
	Chicago	19.73	20.09	18.82	19.53	16.14	17.54
	Denver	19.86	20.24	19.11	19.73	16.75	18.06
Zone 3	San Francisco	19.92	20.29	19.34	19.89	17.73	18.82
	Seattle	19.78	20.15	19.06	19.69	17.16	18.36
Zone 4	Los Angeles & San Diego	19.96	20.32	19.43	19.96	18.18	19.13
Zone 5	Phoenix	19.99	20.32	19.88	20.26	19.32	19.89
	Salt Lake City	19.88	20.24	19.76	20.18	19.10	19.74
	Moscow	19.79	20.18	19.66	20.10	18.92	19.62

6.2 Effect of Cross-polarization Isolation on Signal Performance

In the system under consideration, there are 24 transponder channels. If every channel carries traffic, then for any one channel, the adjacent cross- and co-polarized channels can generate interference to the desired channel, since only these four channels occupy adjacent or overlapping portions of the spectrum (see Fig. 20). The interference from the adjacent, i.e., the co-polarized, channels is negligible in most cases, and the cross-polarized channels provide most of the interference to the desired channel. Since interference from the cross-polarized channels is a function of the cross-polarization isolation, the cross-polarization isolation can be translated into a carrier-to-interference ratio for a given traffic model.

A traffic model is assumed as shown in Fig. 20 and interference from cross-polarized channels to the desired channel (TV in this case) is evaluated using the cross-polarization isolations shown in Table 9 (for a pointing error of 0.1°). Noise-like treatment of interference was as-

sumed in the calculation. After the carrier-to-interference ratio is evaluated, the total carrier-to-noise ratio and, thus, the signal-to-noise ratio are computed for the satellite link. Interferences from other satellite systems are also taken into account for the calculation of the total carrier-to-noise (C/N) ratio based on a basic-5 satellite interference model.[20] Finally the statistical performance of the satellite link is added to the common elements (the end link and the radio link) to determine the overall performance. This statistical performance provides the system

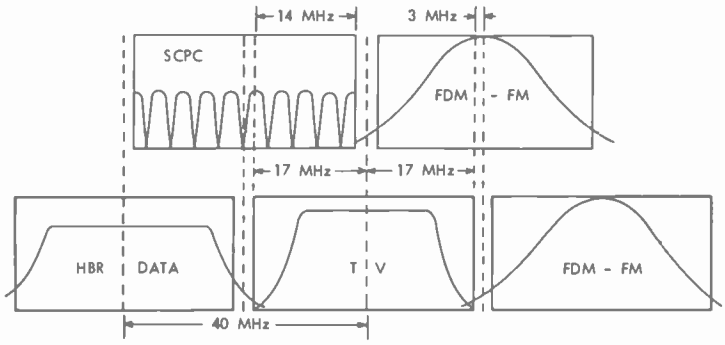

Fig. 20—Interference model to a TV channel.

availability, i.e., the fraction of time that the system is actually capable of providing a desired level of video and audio signal to noise ratio (SNR) for this case. One example of computed results is shown in Fig. 21.[20]

7. Conclusion

Cross-polarization isolation is a very important parameter in the RCA Satcom system and will play an increasingly important role in future satellite communications systems. Sources of depolarization encountered in the spectrum reuse system are identified and described. The method and the procedure described in this paper allows the cross-polarization isolation to be predicted in a consistent manner as a function of time and earth-station location. In the generation of Tables 9 and 10, which can be adopted for system design, several worst-case assumptions are made and accordingly, the prediction is conservative. The effect of loss of polarization isolation on signal performance is also described briefly for a TV signal. Some of the system parameters used in the analysis will presumably require frequent updating when more experimental data on propagation becomes available.

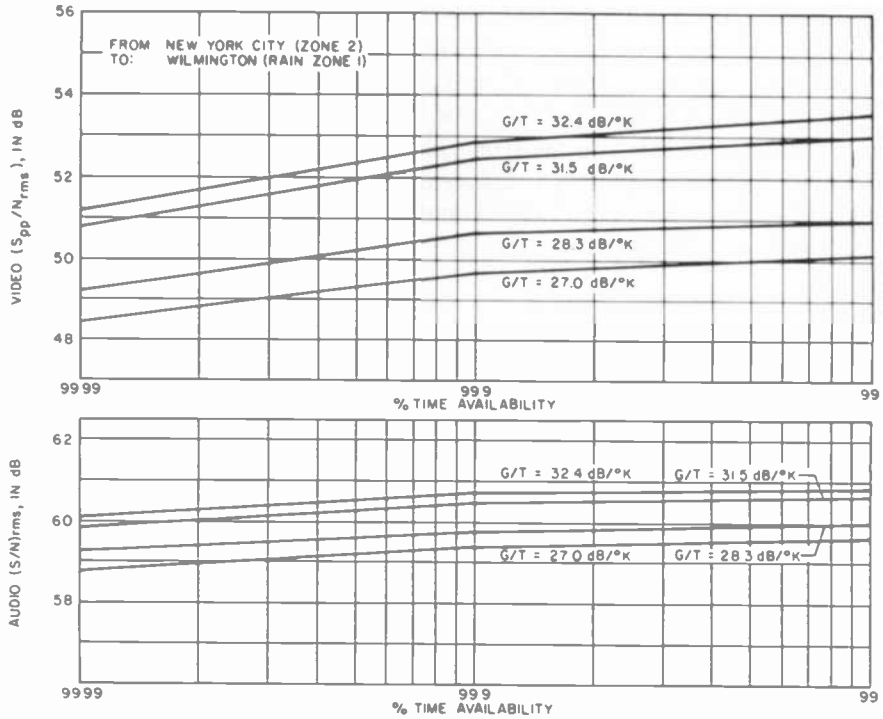

Fig. 21—Statistical performance of video and audio signals as a function of E.S. *G/T*.

Acknowledgment

The author wishes to thank Mr. L. A. Ottenberg for his review of the manuscript. His original initiation of the study and encouragement given to the author throughout the course of work are greatly appreciated.

Appendix 1—Rain-Induced Depolarization

Depolarization due to Differential Attenuation

R_A and R_C, which are the components resolved in the $\vec{OC}$ and $\vec{OA}$ directions (see Fig. 8), will experience attenuation and phase shift through the rain of path length, L. After passing through rain, these two waves can be expressed as

$$R_A' = R_1 \sin\theta e^{-\alpha_A L} \cos(\omega t - \beta_A L) \qquad [18]$$
$$R_C' = R_1 \cos\theta e^{-\alpha_C L} \cos(\omega t - \beta_C L).$$

If differential phase shift, $\beta_A L - \beta_C L$, is zero, then Eq. [18] gives,

$$\tan\Psi = \frac{R_A'}{R_C'} = \tan\Theta e^{-(\alpha_A-\alpha_C)L}$$

$$\Psi = \tan^{-1}[\tan\Theta e^{-(\alpha_A-\alpha_C)L}], \qquad [19]$$

where α_A and α_C are attenuation coefficients in km^{-1} of the waves polarized along $\vec{OA}$ and $\vec{OC}$ direction. Since,

$$20\log e^{-\alpha_A L} = -\alpha_A' L \text{ (dB)}$$

$$20\log e^{-\alpha_C L} = -\alpha_C' L \text{ (dB)}, \qquad [20]$$

then,

$$20\log e^{-(\alpha_A-\alpha_C)L} = -(\alpha_A' L - \alpha_C' L)$$

$$= -(\alpha_A' - \alpha_C')L \text{ (dB)}$$

$$e^{-(\alpha_A-\alpha_C)L} = \log^{-1}\left[\frac{-(\alpha_A' - \alpha_C')L}{20}\right], \qquad [21]$$

where α_A' and α_C' are attenuation coefficients in [dB/km] and $(\alpha_A' - \alpha_C')$ is differential attenuation in [dB/km].

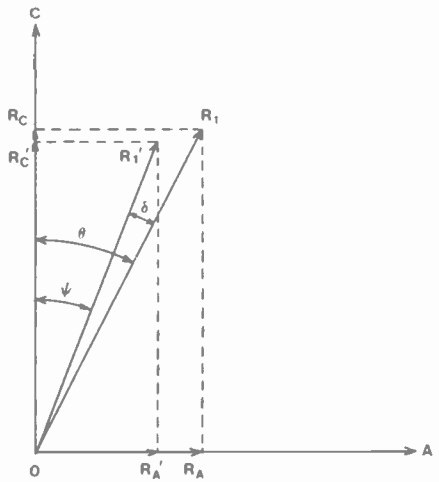

Fig. 22—Rotation of the linearly polarized field vector due to differential attenuation.

Substituting Eq. [21] into Eq. [19], Ψ becomes

$$\Psi = \tan^{-1}\left\{\tan\Theta \cdot \log^{-1}\left[\frac{-(\alpha_A' - \alpha_C')L}{20}\right]\right\}.$$

Original linearly polarized vector R_1 rotates by $\delta°$ as shown in Fig. 22,

$$\delta = \theta - \psi$$

$$= \theta - \tan^{-1}\left\{\tan\theta \cdot \log^{-1}\left[\frac{-(\alpha_A' - \alpha_C')L}{20}\right]\right\}.$$

Cross-polarization isolation due to the rotation of a linearly polarized vector is

$$\text{XPI} = 20 \log \frac{R_1' \sin\delta}{R_1' \cos\delta} \simeq 20 \log(\sin\delta), \qquad [22]$$

for small δ.

It can be seen that the original linearly polarized vector R_1 was rotated by δ with reduced amplitude, after passing through rain, the path length of which is L. The polarization of the wave remains the same as before. The other linearly polarized wave, R_2, rotates in the opposite direction, and its magnitude of rotation is

$$\delta = \theta - \tan^{-1}\left\{\frac{\tan\theta}{\log^{-1}\left[\frac{-(\alpha_A' - \alpha_C')L}{20}\right]}\right\}$$

Depolarization due to Differential Phase Shift

The relative phase in Eq. [18], can be rewritten as

$$R_A' = R_1 \sin\theta e^{-\alpha_A L} \cos\omega t$$

$$= E_A \cos\omega t$$

$$R_C' = R_1 \cos\theta e^{-\alpha_C L} \cos(\omega t + \phi)$$

$$= E_C \cos(\omega t + \phi) \qquad [23]$$

where

$$\phi = \beta_A L - \beta_C L.$$

$(\beta_A - \beta_C)$ is the differential phase shift in degree/km. Since

$$R_C' = E_C \cos\omega t \cos\phi - E_C \sin\omega t \sin\phi \qquad [24]$$

$$\cos\omega t = \frac{R_A'}{E_A} \text{ and } \sin\omega t = \pm\sqrt{1 - \left(\frac{R_A'}{E_A}\right)^2}, \qquad [25]$$

substitution of Eq. [25] into [24] yields

$$\left(\frac{R_C'}{E_C}\right)^2 + \left(\frac{R_A'}{E_A}\right)^2 - \frac{2R_A'R_C'}{E_A E_C}\cos\phi = \sin^2\phi. \qquad [26]$$

This is the equation of an ellipse with its centers at the origin and its

minor axis inclined with respect to the coordinate axes. Elliptical polarization also has a rotational sense associated with it, depending upon the sign of ϕ in Eq. [26]. This is summarized as follows[21]:

$0° < \phi < 180°$ Right Hand Sense

$-180° < \phi < 0$ Left Hand Sense

Either the major axis or minor axis of the ellipse, defined by Eq. [26], is inclined by an angle Ω from the OÂ axis where[21,22]

$$\Omega = 1/2 \tan^{-1}\left[\frac{2E_A E_C \cos\phi}{E_A{}^2 - E_C{}^2}\right]; \qquad [27]$$

and the axial ratio,

$$\text{AR} = \frac{\text{Major Axis}}{\text{Minor Axis}}$$

$$= \tan[1/2 \sin^{-1}(\pm \sin 2\rho \sin\phi)], \qquad [28]$$

where $\tan\rho = E_C/E_A$. If ϕ is zero (differential phase shift is zero), Eq. [26] yields the relationship shown in Eq. [19].

Substitution of $E_A (= R_1 \sin\Theta e^{-\alpha_A L})$ and $E_C (= R_1 \cos\Theta e^{-\alpha_C L})$ into Eqs. [27] and [28] yields

$$\Omega = 1/2 \tan^{-1}\left[\frac{2 \cot\Theta e^{(\alpha_A - \alpha_C)L} \cos\phi}{1 - \cot^2\Theta e^{2(\alpha_A - \alpha_C)L}}\right] \qquad [29]$$

$$\text{AR} = \tan[1/2 \sin^{-1}(\pm \sin 2\rho \sin\phi)],$$

where

$$\tan\rho = \cot\Theta e^{(\alpha_A - \alpha_C)L}. \qquad [30]$$

If the differential attenuation, $(\alpha_A - \alpha_C)L$ is zero, Eqs. [29] and [30] become

$$\Omega = 1/2 \tan^{-1}\left[\frac{2 \cot\theta \cos\phi}{1 - \cot^2\Theta}\right] \qquad [31]$$

$$AR = \tan[1/2 \sin^{-1}(\pm \sin 2\theta \sin\phi)] \qquad [32]$$

where,

$\tan\rho = \cot\theta$, i.e., $\rho = 90° - \theta$

$\phi = (\beta_A - \beta_C)L$, $(\beta_A - \beta_C)$ being differential phase shift in [degree/km]

θ = canting angle and $90° \leq \sin^{-1}(\sin 2\theta \sin\phi) \leq 180$, for AR > 1.

It can be concluded from the above that the differential phase shift introduces an axial ratio deterioration. At the same time, the major axis of the polarization ellipse rotates by an angle, δ, relative to the original attitude of the linear polarized field vector as shown in Fig. 8. This angle, δ, is shown below:

$$\delta = \theta - (90° - \Omega)$$
$$= \theta + \Omega - 90°. \qquad [33]$$

It is interesting to note that if $\phi = 0$ (no differential phase shift), the axial ratio AR becomes infinitive. This is the case for linear polarization.

Appendix 2—Determination of the Geomagnetic Field Parameter

At a point in space p which is dependent upon its altitude h, azimuth of the earth station α, and elevation of the earth station β, there is assumed to exist a geomagnetic field vector $\vec{B}$. The magnitude and orientation of this vector are defined by the magnetic flux density B, inclination (or dip angle) I, and declination D at p. These parameters can

Fig. 23—Orientation of magnetic inclination and declination.

be determined from the magnetic field model described in Refs. [17] and [18] if the longitude, latitude, and altitude of point p are known. Therefore, the longitude, latitude, and altitude of p have to be determined.

Let the surface projection of p be p' and $\Delta\lambda$ and $\Delta\phi$ be the latitudinal and longitudinal separation from the earth station site S as shown in Figs. 23 and 24. These separations are computed with the aid of spherical geometry as shown in Figure 24.[23]

$$\Delta\lambda = c - \pi/2 + \lambda \qquad [34]$$

$$\Delta\phi = \sin^{-1}\left(\frac{\sin\alpha \sin\zeta}{\sin c}\right) \qquad [35]$$

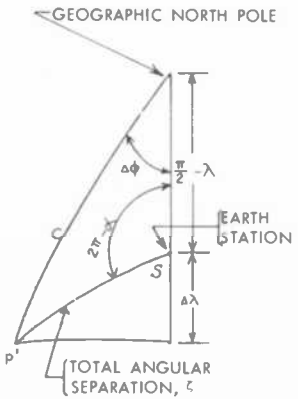

Fig. 24—Spherical geometry considerations.

where $c = \cos^{-1}[\cos\zeta \cos(\pi/2 - \lambda) + \sin\zeta \sin(\pi/2 - \lambda) \cos\alpha]$ and λ is the latitude of the earth station site.

The total angular separation ζ is required in the determination of the projected point in accordance with Eqs. [34] and [35] and is also involved in the correction of nonzenith propagation. The total angular separation is given by

$$\zeta = \cos^{-1}\left(\frac{R}{R + h_m}\cos\beta\right) - \beta. \qquad [36]$$

The geometrical justification for this equation is given in Fig. 25, which illustrates the equivalence of $R\cos\beta$ to $(R + h_m)\cos(\zeta + \beta)$. As discussed in section 5.1, the ionospheric mean height, h_m was chosen to be about 400 km.

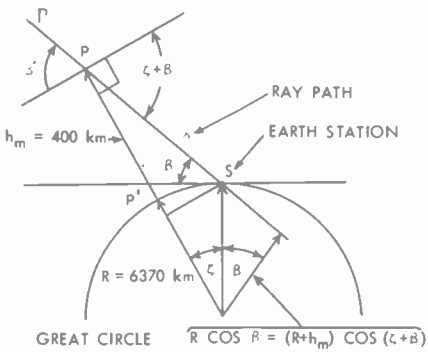

Fig. 25—Geometry illustrating the equivalence of $R\cos\beta$ and $(R + h_m)\cos(\zeta + \beta)$.

In order to solve Eqs. [34], [35], and [36], the azumith α and the elevation β of the earth station, shown in Figs. 24 and 25, have to be determined. A computer program was developed to give α and β for any earth station site if the longitude ϕ and the latitude λ of the earth station site and the satellite location are provided as the input data. Once the values for α and β are substituted into Eqs. [35] and [36], Eqs. [34] and [35] can be solved for $\Delta\lambda$ and $\Delta\phi$. It can also be noted that the longitude and the latitude of p are identical to those of p', since p' is the surface projection of p on the earth.

Since the latitude, longitude, and the altitude of the point p can be specified as $\lambda + \Delta\lambda$, $\phi + \Delta\phi$, and 400 km, respectively, the magnetic parameters at the point p such as B, I, and D can be obtained using the magnetic field model. The magnetic field parameters (h_m, Γ) are then expressed:

$$\Psi(h_m, \Gamma) = B\cos\theta \csc(\zeta + \beta), \text{ evaluated at the point } p(h_m = 400 \text{ km})$$

where B is the magnetic flux density in Wb/m^2, θ is the angle between the ray path Γ and the geomagnetic field vector B, ζ is the total angular separation between the earth station site and the appropriate space point p, and β is the elevation angle of the earth station. The factor $B\cos\theta$ is the component of the geomagnetic field vector $\vec{B}$ along Γ at the space point p. The compensation for nonzenith propagation is incorporated in the $\csc(\zeta + \beta)$ term.

To calculate the angle between the ray path Γ and the geomagnetic field vector $\vec{B}$ at the space point p, it is convenient to use a coordinate system that has its origin at p. Since the coordinate system used to define magnetic field parameters is identical to that used to define the earth-station elevation and azimuth angles, it is necessary to determine the elevation and the azimuth angles at the point p as if the radius of the earth were (6370 + 400) km long. This can be done by using the same computer program that was used to determine the earth station azimuth α and the elevation β. In this case, the computer program was modified such that the radius of the earth is (6370 + 400) km. 400 km is the altitude of the point p above the earth (radius 6370 km). The longitude and the latitude of the point p, which have to be provided as input data, were previously determined. The elevation and azimuth thus determined at the point p are designated as β' and α', respectively. Elevation angle β' obtained in this way is identical to the value of $(\zeta + \beta)$, which was expected from Figs. 14 and 25.

After finding the dip angle I and the declination D of the geomagnetic field vector at the point p, and the elevation β' and the azimuth α' of the point p, the angle, θ between the ray path Γ and the geomagnetic field

vector $\vec{B}$ can be determined from Fig. 26 as follows:

$$\Theta = \cos^{-1}(\lambda_1\lambda_2 + \mu_1\mu_2 + \nu_1\nu_2) \qquad [37]$$

where

$$\lambda_1 = \sin(90 - \beta_1)\cos\alpha_1$$
$$\mu_1 = \sin(90 - \beta_1)\sin\alpha_1$$
$$\nu_1 = \cos(90 - \beta_1),$$

α_1 and β_1 being α' and β', respectively. Also

$$\lambda_2 = \sin(90 - \beta_2)\cos\alpha_2$$
$$\mu_2 = \sin(90 - \beta_2)\sin\alpha_2$$
$$\nu_2 = \cos(90 - \beta_2)$$

α_2 and β_2 being D and $-I$, respectively.

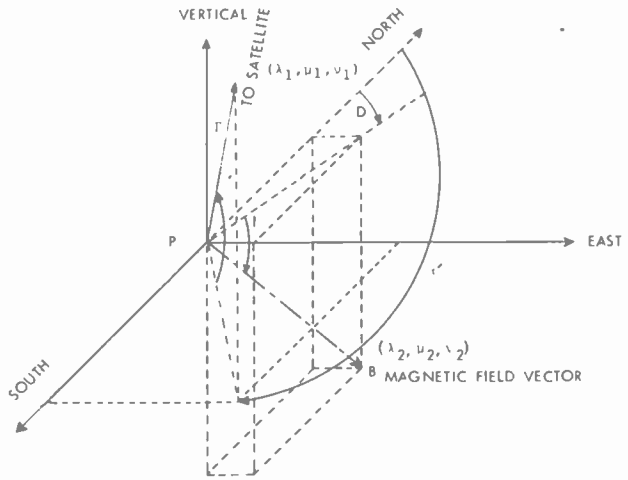

Fig. 26—Coordinate system used to calculate the angle between the ray path Γ and the geomagnetic field vector.

$(\lambda_1, \mu_1, \nu_1)$ and $(\lambda_2, \mu_2, \nu_2)$ are the direction cosines of the ray path Γ and the geomagnetic field vector $\vec{B}$ in the coordinate system defined as shown in Fig. 26. The angle, Θ and the function $\Psi(400, \Gamma)$ are tabulated in Table 5 for various earth-station sites. The angle between ray path Γ and the geomagnetic field vector $\vec{B}$ is about 175° for the transmitted wave from San Diego to the satellite, which is located at 119° W in the equatorial orbit.

References:

[1] E. Laborde, E. Vilar, and A. Vazquez, "Choice of Polarization in Orthogonal Polarization Frequency Reuse for Satellite Links," *Electrical Communication*, **49**, No. 3, p. 289, 1974.

[2] P. A. Watson and S. I. Ghobrial, "Off-Axis Polarization Characteristics of Cassegrainian and Front-Fed Paraboloidal Antennas," *IEEE Trans. Antenna and Propagation*, **AP-20**, No. 6, p. 691, Nov. 1972.

[3] A. R. Raab, "Cross-polarization Performance of the RCA Satcom Frequency Reuse Antenna," Aerospace & Government Systems, RCA Limited, Montreal, Presented at the AP-S/URSI meeting in Amherst, Mass., Oct. 1976.

[4] Private Communication with D. Greenspan, RCA American Communications, Inc. (Oct. 1976).

[5] J. Christopher, D. Greenspan, and P. Plush, personal communication.

[6] T. Oguchi, "Attenuation and Phase Rotation of Radio Waves due to Rain; Calculations at 19.3 and 24.8 GHz," *Radio Science*, **8**, No. 1, p. 31, Jan. 1973.

[7] J. A. Morrison, J. M. Cross, and T. S. Chu, "Rain-Induced Differential Attenuation and Differential Phase Shift at Microwave Frequencies," *Bell System Tech. J.*, **52**, No. 4, p. 599, April 1973.

[8] P. A. Watson and J. Arbabi, "Rainfall Cross-Polarization of Linearly and Circularly Polarized Waves at Microwave Frequencies," *Electronics Lett.*, **8**, No. 11, p. 283, June 1, 1972.

[9] R. R. Taur, "Rain Depolarization Measurement on a Satellite Earth Propagation Path at 4 GHz," Comsat Laboratories, To Be Published in *IEEE Trans. on Antenna And Propagation*.

[10] T. S. Chu, "Rain-Induced Cross Polarization at Centimeter and Millimeter Wavelengths," IEEE 1974 International Communications Conf., p. 12 F-1.

[11] M. J. Saunders, "Cross Polarization at 18 and 30 GHz due to Rain, *IEEE Trans. Antenna and Propagation*, **AP-19**, No. 2, p. 273, March 1971.

[12] R. L. Herbstritt, "Rain Climate Consideration for Domestic Satellites—Continental U. S.," Report No. R-7301, Federal Communications Commission, Office of Chief Engineer, Research Division, Wash., D. C 20554, Nov. 1973.

[13] K. Davies, *Ionospheric Radio Waves*, Blaisdell Publishing Company (1969).

[14] T. Murakami and G. S. Wickizer, "Ionospheric Phase Distortion and Faraday Rotation of Radio Waves," *RCA Review*, **30**, No. 1, p. 475, Sept. 1969.

[15] J. S. Nisbet, "On the Construction and Use of a Simple Ionospheric Model," *Radio Science*, **6**, p. 437, April 1971.

[16] M. K. Lee, "Propagation Predictions and Studies Using a Ray Tracing Program Combined with a Theoretical Ionospheric Model," *IEEE Trans. Antennas and Propagation*, **AP-23**, No. 1, p. 132, Jan. 1975.

[17] D. C. Jensen and J. C. Cain, "Interim Geomagnetic Field (abstr.)," *J. Geophysical Research*, **72**, No. 23, p. 6099, Dec. 1, 1967.

[18] S. Chapman and J. Bartels, *Geomagnetism*, Vol. 2, Oxford at the Clarendon Press (1962).

[19] Ionospheric Predictions (published monthly, 3 months in advance), Institute for telecommunication Sciences and Aeronomy, U. S. Government Printing Office.

[20] A. W. Brook, M. K. Lee, and L. A. Ottenberg, "RCA Satcom TV Distribution System," 25th Annual NCTA (National Cable Television Association) Convention and Exposition, Dallas Convention Center, Dallas, Tx., April 4–7, 1976.

[21] J. D. Kraus, *Antenna*, McGraw Hill Book Co. (1950).

[22] J. M. Kelso, *Radio Ray Propagation in the Ionosphere*, McGraw-Hill Book Co., 1964.

[23] J. M. Goodman, "Prediction of Faraday Rotation Angles at VHF and UHF," NRL Report 6234, U. S. Naval Res. Lab., April 28, 1965.

Properties of Amorphous Silicon and a-Si Solar Cells *

D. E. Carlson, C. R. Wronski, J. I. Pankove, P. J. Zanzucchi, and D. L. Staebler

RCA Laboratories, Princeton, N.J. 08540

Abstract—Discharge-produced amorphous silicon and thin-film a-Si solar cells are characterized by a series of property measurements. Film properties measured include optical absorption, resistivity, photoconductivity, and photoluminescence. The solar cells are characterized by *I-V* and *C-V* measurements (dark and illuminated) and also by measurements of the photocurrents as a function of wavelength and bias.

Introduction

A new type of solar cell has been developed at RCA Laboratories using amorphous silicon (a-Si) deposited from a glow discharge in silane (SiH_4).[1,2] These solar cells utilize ~1 μm of a-Si and have been fabricated in heterojunction, p-i-n, and Schottky-barrier structures on low-cost substrates such as glass and steel.

Discharge-produced a-Si has optical and electronic properties that are ideally suited for a solar cell material. The optical absorption coefficient is significantly larger than that of crystalline Si over the visible light range[1] and therefore most of the solar radiation with $\lambda < 0.7$ μm is absorbed in a film ~1 μm thick.

The electronic properties are exceptional for an amorphous semiconductor and can be attributed to the low density of defect states within the energy gap. This low density of gap states appears to be due partially

* Research funded by the Division of Solar Energy of the U. S. Energy Research and Development Administration, under Contract No. EY-76-E-03-1286 and RCA Laboratories, Princeton, New Jersey 08540.

to the discharge kinetics and partially to compensation of dangling bonds by hydrogen. Consequently, the carrier lifetimes in discharge-produced a-Si are expected to be significantly longer than in other amorphous semiconductors with comparable energy gaps, and, in fact, the electron recombination lifetime has been estimated to be ~10 μs.[3] The hole diffusion length appears to be sufficient to allow efficient collection of photogenerated carriers within a film thickness of ~1 μm.[1]

The low density of gap states also allows the Fermi level to be moved easily with respect to the band edges by means of an external field, substitutional doping, or a Schottky barrier. Thus, built-in potentials on the order of 1.1 V have been measured in p-i-n devices,[4] and barrier heights of ~1.1 eV have been obtained with Pt Schottky barriers on a-Si.[5,6] These later devices have exhibited open-circuit voltages in excess of 800 mV.

Process Technology

The a-Si was deposited from a glow discharge in silane (SiH_4). The discharge could be produced (1) with a dc system with the substrate at or near the cathode, (2) in an electrodeless system using an external rf coil, or (3) in an rf capacitive system where the substrate is located on one of the capacitor plates.

The depositions were performed at pressures of 0.5 to 2.0 Torr of SiH_4. In the dc discharge, the current density at the cathode was in the range 0.2 to 3.0 mA/cm^2 with voltages in the range of 600 to 1500 V.

Both doped and undoped a-Si films with thicknesses in the range of 0.1 to 3.0 μm have been deposited. The films were deposited at substrate temperatures varying from 200° to 420°C. Dopants such as B_2H_6, PH_3, AsH_3, $Sb(CH_3)_3$, and $Bi(CH_3)_3$ have been investigated using discharge atmospheres containing 0.1% and 1.0% by volume of the dopant gas in SiH_4.

A number of conductive materials have been evaluated to determine the best substrates for a-Si cells in terms of low contact resistance and stability of the a-Si/substrate combinations at 450°C. The best substrates are stainless steel, Nb, Ta, V, Ti, Cr, and Mo.

The maximum substrate temperature is $\lesssim$500°C for all investigated substrates; even films deposited at lower temperatures show poor photovoltaic characteristics when annealed at ~500°C. The upper limit of 500°C for depositions may be due to a change in the short-range structure of the a-Si. An analysis of an a-Si film on a Nb foil using differential scanning calorimetry (DSC) indicated a small broad exothermic transition starting at ~540°C and peaking at ~590°C for a heating rate of 10°C/min. However, a large exothermic peak was observed at ~665°C,

which is the crystallization temperature for a-Si on SiO_2 for comparable heating rates. A-Si films deposited at 500°C and other a-Si films deposited at 350°C and annealed at 620°C for 5 min. were examined by electron diffraction and were found to be amorphous.

Properties of a-Silicon

(a) Optical Properties

The reflection and transmission data for various a-Si films were obtained with a spectrophotometer*, and the absorption coefficients and refractive indices were calculated from a computer program based on Ref. [7]. The a-Si films were typically 900 Å thick (on SiO_2 substrates) which ensured good accuracy for wavelengths in the visible range but not in the infrared (where $\alpha < 10^4\ cm^{-1}$).

Both the absorption coefficient and the refractive index have been measured for a-Si films deposited at substrate temperatures varying from 200° to 420°C using both dc (with a cathodic screen) and electrodeless rf discharge systems. Fig. 1 shows that the absorption coefficient for rf-produced films increases with increasing substrate temperature. A film deposited at ~200°C exhibited values very close to the data for the film deposited at ~325°C. The data of Loveland et al[3] is for a film deposited at room temperature. When films deposited at ~320°C were annealed for 15 min at 400°C in a He-H_2 atmosphere, the absorption coefficients increased toward the values observed for films deposited at ~420°C.

Boron doped films (from 1% B_2H_6 in SiH_4) exhibit an absorption coefficient that is twice as large as that of undoped films at $\lambda = 0.43\ \mu m$ and ten times as large at $\lambda = 0.7\ \mu m$ (for substrate temperatures of ~330°C). Phosphorous doped films (from 1% PH_3 in SiH_4) exhibit absorption coefficients midway between those of undoped and boron-doped films.

The refractive index of rf-produced, undoped a-Si films is the same as single-crystal Si for $T_s \simeq 200$°C over the wavelength range of 0.4 to 0.8 μm. However, as T_s increases, the refractive index increases and is roughly 10% larger at $T_s = 420$°C.

(b) Resistivity and Photoconductivity

The samples for resistivity measurements were fabricated by depositing a-Si on a four-parallel-strip Cr pattern on SiO_2. The resistivity was

* Carey Model 14R.

measured in a dry nitrogen atmosphere from 26° to 200°C using electrometers to monitor the voltage and current.

The phosphorus-doped films were the most conductive with $\rho = 53$ ohm-cm for a film deposited in a SiH_4 atmosphere containing 1% PH_3. This film also exhibited the lowest thermal activation energy for an n+ film ($E_a \simeq 0.17$ eV in $\rho = \rho_0 e^{-E_a/kT}$). The most conductive boron-doped films were produced by a discharge in SiH_4 containing 1% B_2H_6. The characteristic resistivity and activation energy were respectively $\rho \simeq 2.5 \times 10^2$ ohm-cm and $E_a \simeq 0.14$ eV.

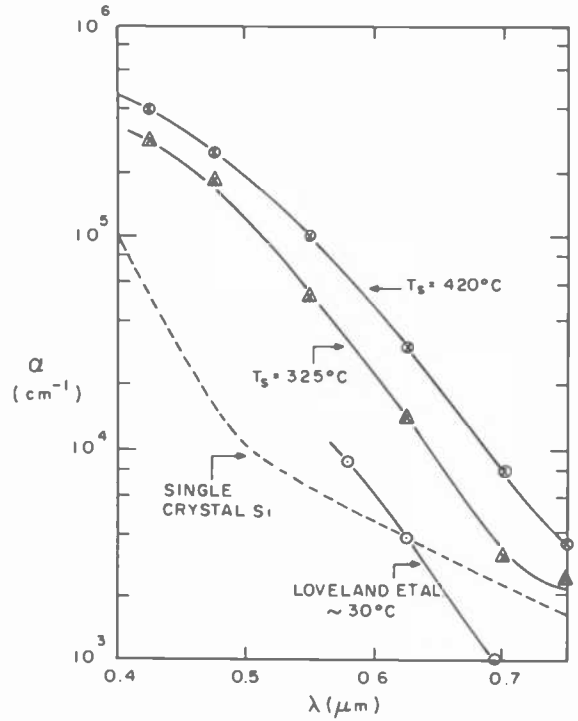

Fig. 1—Optical absorption coefficient of a-Si as a function of wavelength for different deposition temperatures.

While the dark resistivity shows a strong dependence on T_s, the dependence of the photoconductivity (σ_L) on T_s is much weaker. The activation energies for undoped films are large in the dark and decrease as T_s increases. (E_a decreases from ~0.8 eV to ~0.5 eV as T_s increases from 200 to 400°C). When the film is illuminated, E_a is ~0.05 eV. The photoconductivity varies with light intensity as $\sigma_L \propto (\text{intensity})^{\gamma}$. At AM1, σ_L ranges from 1.3 to 5.6×10^{-4} (ohm-cm)$^{-1}$, and γ ranges from 1.0 at low light levels to 0.5 near AM1 intensities.

Fig. 2 shows how σ_L varies with intensity for a dc-produced film deposited at $T_s = 350°C$; the film thickness was ~1 μm. With white light the short wavelength photons will be strongly absorbed at the surface. A red filter ($\lambda > 0.625$ μm) is used to assure relatively uniform absorption throughout the film thickness, so that volume generated photoconductivity can be measured.

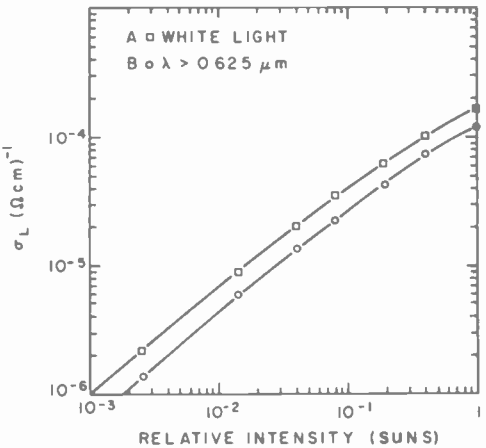

Fig. 2—Photoconductivity versus light intensity.

Since the contacts are ohmic (electron injecting), the photoconductivity measured at a given flux ($\lambda = 0.61$ μm) can be used to estimate the electron recombination lifetime (τ_n). Assuming a drift mobility[8] of ~5 cm^2/V-s, τ_n is in the range of 1 to 10 μs for several undoped a-Si films at ~0.01 AM1 illumination.

(c) Photoluminescence

The photoluminescence was excited by an Argon laser (80-mW out at $\lambda = 0.488$ μm). The measurements used a quartz-prism spectrometer, a cooled photomultiplier, and lock-in detection. The a-Si films were mounted on a cold finger which could be cooled to 78 K. A typical emission spectrum of an undoped layer is shown in Fig. 3. The photoluminescence peaks at 1.28 ± 0.08 eV, and exhibits an external quantum efficiency of 10^{-3} (corresponding to an estimated internal quantum efficiency of ~10%).

Increasing dopant concentrations cause the photoluminescence intensity to decrease, and films deposited from atmospheres containing ~1% of B_2H_6 or PH_3 in SiH_4 do not exhibit a signal. The substitution

of D_2 for H_2 in a discharge atmosphere, also containing 10% SiH_4, causes the photoluminescence peak to shift up in energy by ~0.1 eV (Fig. 3). The emission spectrum shifts to lower energies with increasing temperature at a rate $dE/dT = -2.5 \times 10^{-4}$ eV/°K. The temperature dependence of the emission intensity gives an activation energy of 0.116 eV for nonradiative recombination consistent with the data of Engemann and Fischer.[9]

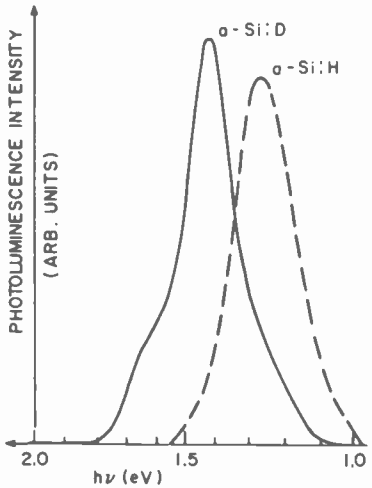

Fig. 3—Photoluminescence spectrum of undoped and D-doped a-Si.

Annealing a film deposited at 350°C first at 200°C for 5 min. and then at successively higher temperatures causes the photoluminescence intensity to increase for annealing temperatures up to 450°C; no signal was observed after 5 min at 500°C.

(d) Electroluminescence

Forward biased p-i-n diodes and Schottky barrier diodes emit radiation having a spectrum identical to that obtained by photoluminescence. The emission intensity increases sublinearly with the current through the diode (Fig. 4). The emission spectrum, however, does not change while the current is varied, (Fig. 5).

(e) Diffusion Coefficients

Compositional profiles of a-Si solar cells have been obtained using Auger electron spectroscopy and secondary ion mass spectroscopy (SIMS).

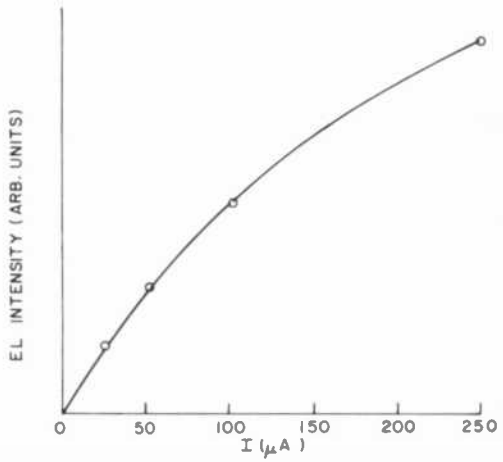

Fig. 4—Variation of emission intensity with current through the diode.

These profiles have been analyzed to obtain the diffusion coefficients for dopants and impurities in a-Si at the deposition or annealing temperatures, and these data are shown in Table 1.

Device Properties

(a) Efficiency

A conversion efficiency of 5.5% was obtained for a Pt Schottky-barrier cell in sunlight of 65 mW/cm^2. The cell was constructed by first depos-

Table 1—Diffusion Coefficients* in a-Si

Diffusing Species	T(°C)	D (cm^2/s)
Pd	180	2.6×10^{-15}
O	250	$\lesssim 3.0 \times 10^{-16}$
P	350	$\sim 4 \times 10^{-14}$
Sb	400	2.3×10^{-15}
B	400	10^{-12}

*These coefficients are all much larger than the values found in single-crystal Si; e.g., D_{Sb} (1030°C) $\simeq 10^{-15}$ cm^2/s in single-crystal Si while we find a comparable diffusion coefficient in a-Si at a much lower temperature (~400°C). The larger values are probably due to the more open structure of the a-Si.

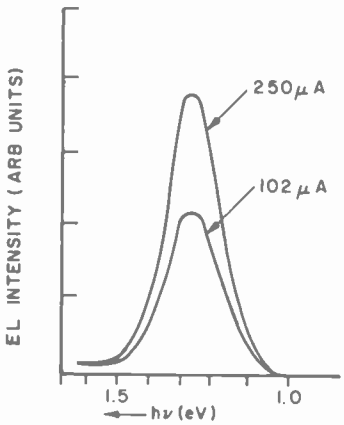

Fig. 5—EL spectrum at two currents through the diode.

iting a phosphorus-doped layer (~0.1 μm thick) and then an undoped layer (~1.0 μ thick); the Schottky barrier was formed by the electron beam evaporation of a 45-Å Pt film. A Pd contact pad (~800-Å thick, area ≃ 0.5 mm^2) was evaporated onto one side of the Pt dot leaving an active area of 1.5 mm^2, and finally ~450 Å of ZrO_2 was deposited as an antireflection coating. The illuminated I-V characteristics are shown in Fig. 6; four dots within an area of ~1 cm^2 exhibited similar characteristics to within 10%.

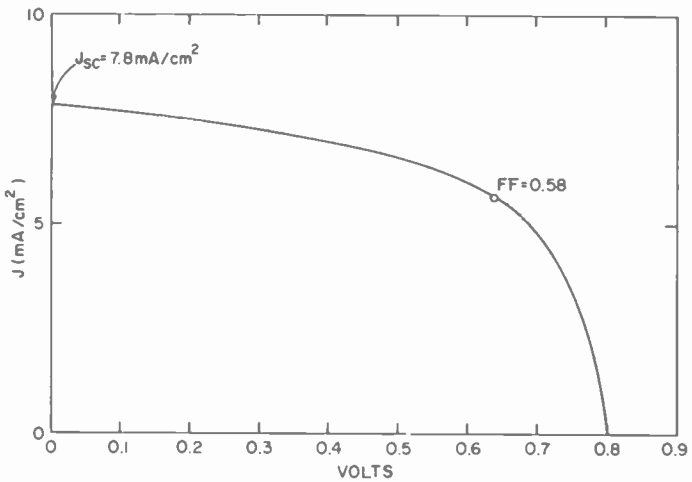

Fig. 6—Illuminated I-V characteristics of a Pt Schottky-barrier cell in sunlight of 65 mW/cm^2.

The largest value of V_{oc} to date is 865 mV for an Ir Schottky barrier on an rf-produced film deposited at ~300°C. The fill factors are usually in the range of 0.5–0.6 in sunlight, but values as high as 0.70 have been measured in blue light (filtered sunlight).

Fig. 7 shows the dependence of V_{oc} on metal work function for a series of Schottky barriers on a-Si films. (The metal work functions were taken from Ref. [10]). A plot of the barrier height versus the metal work functions shows a similar dependence, and the slope indicates a density of surface states comparable to that of single-crystal Si.

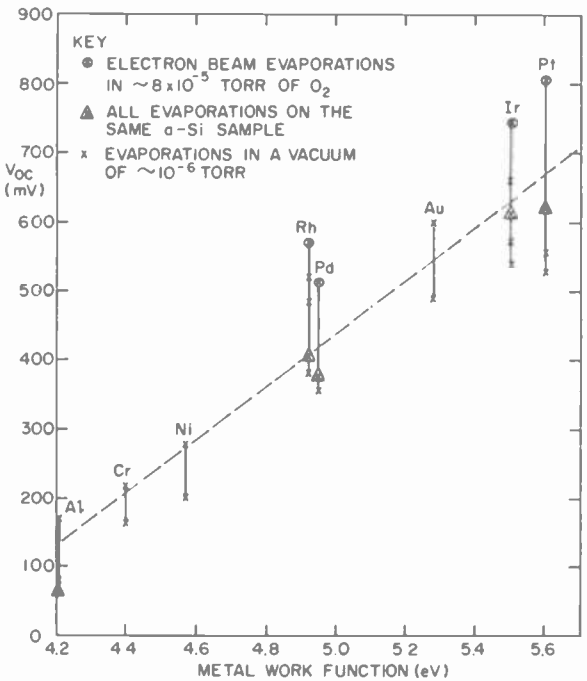

Fig. 7—Open-circuit photovoltage versus metal work function.

(b) Dark I-V Data

According to the diffusion theory of metal–semiconductor rectification, the saturation current density is given by: $J_o = B \exp(-q\phi/kT)$ where ϕ is the barrier height. The dark I-V data in Fig. 8 yields barrier heights between 1.05 eV for Pt and 0.8 eV for Cr.[5] The devices are series-resistance limited in far forward bias and the inset of Fig. 8 shows that the

built-in potential (V_0) is ~0.50 V for Pt and ~0.25 V for Cr and a series resistance $R_s \approx 1\text{–}2 \times 10^3$ ohm cm^2. Similar values for V_0 are obtained from plots of $1/C^2$ versus V.[6] The dependence of R_s on temperature indicates a position of the Fermi level with respect to the conduction band of $\epsilon_c - \epsilon_F \simeq 0.53$ eV. Hence, $\phi_{Pt,Cr} = V_o + \epsilon_C - \epsilon_F + (kT/q) = 1.05, 0.8$ is in excellent agreement with the values determined from J_o.

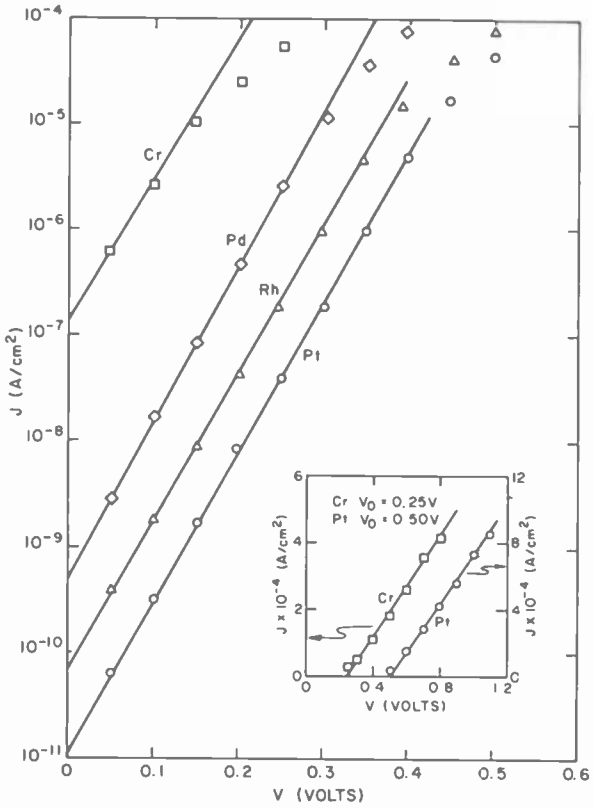

Fig. 8—Dark I-V characteristics of several Schottky-barrier cells.

The barrier height on a-Si is generally ~0.3 eV higher than on single-crystal Si for the same metal evaporation. This is due primarily to the larger bandgap of a-Si (~1.6 eV versus 1.12 eV for crystalline Si).

The diode characteristics shown in Fig. 8 are close to those of an ideal diode with diode quality factors of 1.0 to 1.2. Thus, negligible recombination is occurring in the metal/a-Si junction. In J_{sc} versus V_{oc} mea-

surements, the diode quality factor is also close to unity, and the exponential behavior extends to current densities of $\gtrsim 10^{-2}$ A/cm^2. The extension of the exponential region is due to the photoconductive effect; the data of Fig. 8 shows that the dark current density becomes series-resistance limited at $\sim 10^{-4}$ to 10^{-5} A/cm^2 due to a bulk resistivity of $\sim 10^7$ ohm/cm in the quasi-neutral region. However, in AM1 illumination this resistivity decreases to $\lesssim 10^4$ ohm-cm (see Fig. 2).

(c) Photocurrents

Because the hole lifetimes in a-Si are much shorter than in crystalline Si, the barrier field plays a much more important role than in single crystal Si cells.[11] Efficient collection of photogenerated holes in a solar cell occurs only within the extent of the barrier region, W_B, plus approximately a hole diffusion length, L_p. In a cell having thickness, L, essentially all the carriers generated in the quasi-neutral region (L-W_B) are lost if $L_p \ll (L - W_B)$. Since W_B depends on the bias, V, the photocurrent $J_L(V)$ is a function of bias when L_p is $\ll [L - W_B(V)]$ and $L_p \ll 1/\alpha$. The results of a cell structure where $L_p \ll [L - W_B(V)]$ and $L_p < W_B(V)$ are shown in Fig. 9, where the photogenerated carriers are only collected from the region $W_B(V)$. Fig. 9(a) shows how the ratio J_L/J_{sc} increases with reverse bias for illumination at different wavelengths, and Fig. 9(b) shows the corresponding depletion width (measured in the dark). Thus, the collection efficiency (and J_L) for short wavelength photons saturates, since all photons are absorbed within W_B, while the collection efficiency of long wavelength photons varies with W_B. The corresponding AM1 I-V characteristics show poor saturation and low values of the fill factor (J_L decreases significantly under forward bias due to the decrease in W_B).

In other cells, the dependence of J_L/J_{sc} on reverse bias is not very strong even for red light, and in these cells L_p is an appreciable fraction of the cell thickness. These cells also exhibit relatively good values of the fill factor ($\sim$0.55 to 0.61).

(d) Capacitance-Voltage Data

Fig. 10 shows plots of $1/C^2$ versus V for a cell in the dark and under 0.02 AM1 illumination. The depletion width at zero bias decreases from $\sim$0.4 μm in the dark to $\sim$0.15 μm in the light due to a net positive charge from photogenerated holes in the barrier region. However, J_L was relatively insensitive to bias and exhibited a linear dependence on light intensity up to AM1 illuminations, indicating that L_p is a few tenths of a micron.

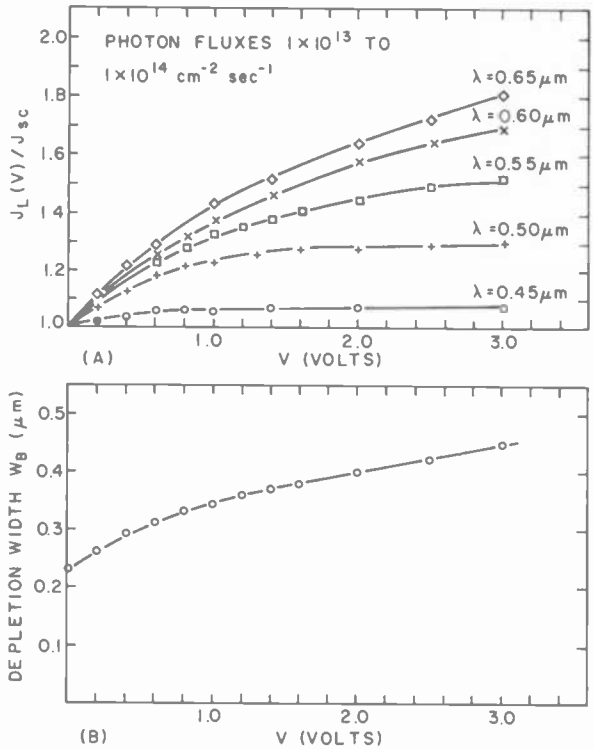

Fig. 9—(a) Relative photocurrent as a function of reverse bias for different wavelength illumination and (b) dark depletion width versus reverse bias.

A similar estimate for L_p was obtained by using the optical absorption data to fit the measured collction efficiency as a function of wavelength;

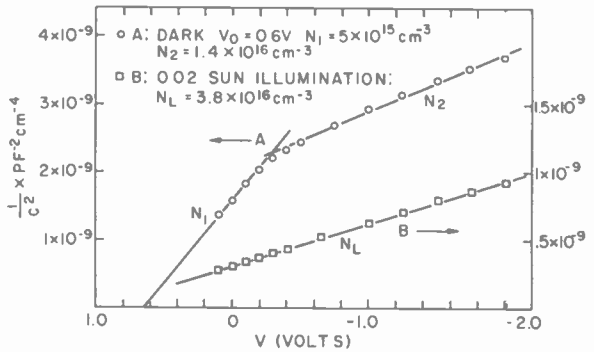

Fig. 10—Plots of $1/C^2$ versus V for a diode in the dark and in 0.02 AM1 illumination.

i.e., only carriers generated in the first 0.3 μm are collected, and thus $J_{sc} \approx 12$ mA/cm^2.

(e) Life Tests

A Pd Schottky-barrier cell has shown no degradation after 4400 hours of continuous illumination of ~75 mW/cm^2; p-i-n cells have remained stable after more than 18 months on the shelf.

Pt Schottky-barrier cells where the a-Si was etched in buffered HF prior to the Pt evaporation have shown no degradation after heating in air at 200°C for 15 min. J_{sc} remained constant after heating to temperatures as high as 400°C for 15 min, but V_{oc} started to decrease after heating to temperatures $\gtrsim$250°C.

Discussion

Since the optical absorption coefficient increases with increasing substrate temperature, larger values of J_{sc} should result for deposition at higher temperatures. However, substrate temperatures must be kept below ~500°C since films deposited or annealed at this temperature show poor photovoltaic characteristics. Another difficulty is that impurities can diffuse into the undoped layer at high substrate temperatures and degrade the photovoltaic properties.

The optical absorption data for a film deposited at 420°C can be used in conjunction with the solar spectral distribution to estimate a theoretical limit for J_{sc} of ~24 mA/cm^2 (assuming 100% collection efficiency for photons absorbed in a light path of 2 μm).

The resistivity measurements suggest that phosphorus-doped films should act as the best n+ contacting layers, since they have the lowest resistivity and the lowest activation energy. Even the most conductive phosphorus-doped films exhibited activation energies of ~0.17 V indicating that not all the phosphorus goes into shallow donor sites. This hypothesis is confirmed by the drastic decrease observed in the photoluminescence signal as the PH_3 content of the discharge atmosphere increases. This observation can be interpreted by assuming that the density of recombination centers increases as the phosphorus content increases. These centers may be due to fully compensated phosphorus atoms (i.e., bonded to five Si atoms), clusters of phosphorus atoms, or phosphorus–hydrogen complexes in the a-Si. Further support for the above hypothesis comes from collection efficiency measurements in p-i-n devices (where lifetime degradation appears to occur in the doped layers) and from the increased optical absorption observed in the infrared for doped films.

The isotope effect observed in photoluminescence indicates that a state associated with bonded hydrogen is involved in the radiative transition. Since the Si-Si and Si-H bond energies are almost the same (within 2% for the diatomic molecules), the compensation of dangling bonds by hydrogen may shift the defect states to energies close to the conduction and valence bands. The photoluminescence signal may then arise from a radiative transition between these localized states. These states rather than the hypothesized tail states may be limiting the built-in potential and hence V_{oc}. The hypothesis that tail states are not involved in luminescence is supported by the absence of a spectral shift when the excitation intensity is varied.

The photoconductivity data indicates monomolecular recombination through centers near ϵ_F at low light levels, and at light intensities approaching AM1 the photoconductivity becomes sublinear due to decreasing electron lifetimes. The series resistance of a quasi-neutral region in the bulk a-Si should not be a limiting factor for properly constructed cells due to the photoconductive effect. Since $\sigma_L \gtrsim 10^{-4}$ (ohm-cm)$^{-1}$ for AM1 illumination (see Fig. 2), the series resistance of a quasi-neutral region $\sim$1 μm thick is $\lesssim$1 ohm for a 1 cm^2 area. Thus, the resistance of a quasi-neutral region should not significantly limit the conversion efficiency of an optimized a-Si cell.

The dependence of V_{oc} on metal work function (see Fig. 8) indicates that the best conversion efficiencies will be achieved with cells using Pt or Ir. The larger values of V_{oc} obtained in some samples may be due to a lower density of defect states near the conduction and valence bands or a smaller density of surface states, thus allowing a greater built-in potential.

Since a value of 865 mV has been obtained for V_{oc}, a practical limit might be closer to 900 mV rather than 800 mV as originally assumed.[1] Since the theoretical fill factor (FF) for an ideal diode is $\sim$0.87, the limit for the efficiency of an a-Si solar cell is given by $\eta_{AM1} \simeq (FF) J_{sc} V_{oc} \approx (0.87)(24)(0.9) = 18.8\%$ assuming 100% collection efficiency in a 1-μm-thick cell with a reflecting back contact. For an average transmission of $\sim$90% into the cell, the limiting efficiency becomes $\sim$17%.

The major factor limiting the conversion efficiency to 5.5% is the small hole diffusion length, L_p. As discussed earlier, the photocurrent is determined by the depletion width (W_B) if L_p is small; i.e., only electron–hole pairs generated within W_B will be sufficiently collected so both J_{sc} and the fill factor will be less than predicted for the ideal diode. The fill factor is reduced since J_L decreases as W_B decreases in forward bias. This effect is relatively insensitive to light intensity unlike the effect of a high series resistance.

Our best cells exhibit relatively good reverse saturation and good fill

factors (~0.55 to 0.61), and in these devices $L_p \approx W_B(0) \approx 0.3\ \mu$m. The optical absorption data predicts that J_{sc} should be ~15 mA/cm^2 for 100% collection efficiency in ~0.3 μm of a-Si. Assuming the average transmission is actually ~80%, the predicted value of J_{sc} is ~12 mA/cm^2 which is the observed value at AM1 intensities. Thus, an improvement in L_p by a factor of ~3 should increase J_{sc} by ~60% for a 1-μm cell (in this case an appreciable amount of red light that is reflected at the back contact can also be absorbed). A significant improvement should also be observed in the fill factor.

References:

[1] D. E. Carlson and C. R. Wronski, "Amorphous Silicon Solar Cell," *Appl. Phys. Lett.*, **28**, p. 671 (1976).

[2] D. E. Carlson, C. R. Wronski, A. R. Triano, and R. E. Daniel, "Solar Cells Using Schottky Barriers on Amorphous Silicon," 12th Photovoltaic Specialists Conf., Baton Rouge, LA, Nov. 15–18, 1976.

[3] R. J. Loveland, W. E. Spear, and O. Al-Sharbary, "Photoconductivity and Absorption in Amorphous Silicon," *J. Non-Cryst. Solids*, **13**, p. 55 (1973/74).

[4] D. E. Carlson and C. R. Wronski, "Solar Cells Using Discharge-Produced Amorphous Silicon," *J. Electronic Materials*, **6**, p. 95 (1977).

[5] C. R. Wronski, D. E. Carlson, and R. E. Daniel, "Schottky Barrier Characteristics of Metal-Amorphous Silicon Diodes," *Appl. Phys. Letters* **29**, p. 602 (1976).

[6] C. R. Wronski, D. E. Carlson, R. E. Daniel, and A. R. Triano, "Electrical Properties of a-Si Solar Cells," International Electron Devices Meeting, Wash., D.C., Dec. 6–8, 1976.

[7] S. G. Tomlin, "Optical Reflection and Transmission Formular for Thin Films," *British J. Appl. Phys. (J. Phys. D)*, **1**, p 1667 (1968).

[8] P. G. LeComber and W. E. Spear, "Electron Transport in Amorphous Silicon Films," *Phys. Rev. Lett.* **25**, p. 509 (1970).

[9] D. Engemann and R. Fischer; *Proc. Fifth International Conf. on Amorphous and Liquid Semiconductors*, Garmish-Partenkirchen, p. 947, (1973).

[10] A. H. Sommer, *Photoemissive Materials, p. 21*, John Wiley & Sons, New York, (1968).

[11] C. R. Wronski, "Electronic Properties of Amorphous Silicon in Solar Cell Operation," (In Press); "Photovoltaic Devices," Special Issue IEEE Trans. Electron Devices, H. W. Brandhorst, Jr. (Ed.).

Electron Trapping Noise in SOS MOS Field-Effect Transistors Operated in the Linear Region*

S. T. Hsu

RCA Laboratories, Princeton, N.J. 08540

Abstract—The theory of generation–recombination (g-r) noise in field-effect transistors is extended to explain low-frequency trapping noise due to trap state at the space-charge region of thin-film MOS FET's. The trap state most susceptible to fluctuation is found to be one-third occupied. Only nearly one-third-occupied trap states contribute significant noise to the device. It is shown that the trap-state energy, the trap-state density, and the capture cross section of the trap state can be determined from noise measurements.

The characteristic of electron trapping noise on p-channel thin film MOSFET's is found to be very complex. This electron trapping noise is strongly related to the electrical properties at and near the silicon–sapphire interface.

1. Introduction

It is well understood that in a field-effect transistor made on a bulk semiconductor, the carrier trapping effect in the depletion region of the device is negligible compared to the effect of the generation of electron–hole pairs in that region. Consequently, bulk trapping noise has not been a problem in bulk MOSFET's. Generation–recombination (g-r) noise in FET's has been studied very extensively during the past decade. The g-r noise in conduction channel was first studied by van der Ziel.[1] Sah[2] published the first theoretical work on g-r noise due to g-r centers

* This work was supported by Air Force Avionics Laboratory, Air Force System Command, Wright-Patterson Air Force Base, Ohio, under Contract No. F33615-73-C-1117.

located in the depletion region of field-effect transistors. Lauritzen[3] performed extensive experimental work on g-r noise in FET's. To the author's knowledge, trapping noise in FET's has not been studied in any detail.

In a previous paper,[4] we reported that the low-frequency excess noise in an SOS (silicon-on-sapphire) MOS FET is dominated by electron trapping noise if the frequency is larger than a few tens of hertz. We also found that the electron trap state is located at 0.65 eV below the edge of the conduction band and that in an SOS film the density of trap states is much larger than the density of g-r centers. In this paper, we present a simplified model for trapping noise in SOS/MOSFET's operated in the linear region. The results provide an understanding of trapping noise in the device when it is operated in the saturation region. It is also shown that the noise measurement at the linear region is an excellent method for measuring the density, the capture cross section, and the energy of the trap state in SOS films.

2. Theory

Only the effect of deep electron trap states on SOS MOSFET noise will be considered. The same theory can be applied to the deep hole trap states effect. The mechanism for electron trapping noise in n-channel SOS MOSFET's is different from that of p-channel devices. We shall discuss electron trapping noise in n-channel devices first.

We assume that in the linear region of operation the silicon film is completely depleted, and the sapphire substrate is at least an order of magnitude thicker than the silicon film. The quasi-Fermi level of electron trap states in the depletion region is assumed to be equal to the Fermi level in the neutral region. The electron distribution function in the trap state, f_t, is given by

$$f_t = \frac{n_t}{N_t} = [1 + \exp(E_t - E_{FP} - qV)/kT]^{-1}, \qquad [1]$$

where N_t is the trap state density, n_t is the trapped electron density, V is the static potential at the given point with respect to the neutral region, and E_t and E_{FP} are the trap energy and the Fermi-level of holes, respectively. All energies are referred to the edge of the conduction band.

It is appropriate to assume that free electrons in the conduction band are under quasi-thermal equilibrium condition. The electron density is, therefore, able to recover its equilibrium value in a very short time after it is perturbed by the fluctuation of charge density at the trap states.

From the g-r noise theory,[5] the time constant for the charge density fluctuation in the trap states at the depletion region is

$$\tau = \frac{f_{tp}}{Cn_1}, \qquad [2]$$

where C is a constant equal to the product of capture cross section and the thermal velocity of electrons, n_1 is the free electron density when the electron Fermi-level is located at the trap energy, and $f_{tp} = 1 - f_t$. The variance of the fluctuation of the trapped electron density is

$$\text{Var } n_t = N_t f_t f_{tp}. \qquad [3]$$

The spectral intensity of the fluctuation of the trapped electron density is, therefore, given by

$$S_{n_t}(\omega) = \frac{4\tau \text{ Var } n_t}{1 + \omega^2\tau^2}. \qquad [4]$$

This noise spectrum has a frequency-independent low-frequency plateau followed by an f^{-2} frequency dependent region as is in the case of g-r noise. Consequently, from a single noise spectrum measurement one cannot discriminate between trapping noise and g-r noise. The low-frequency plateau of the trapping-noise spectrum has a maximum value of

$$S_{n_t}(0)\,|_{\text{Max}} = \frac{16\,N_t}{27\,Cn_1} \qquad [5]$$

at $f_t = 1/3$. The trap state most susceptible to fluctuation is one-third occupied. This is one of the main differences between trapping noise and g-r noise. In the case of g-r noise, the state most susceptible to fluctuation is half occupied.[6,7]

The fluctuation of charge density at the depletion region causes a fluctuation of surface potential. According to Sah,[2] this relationship is given by

$$\overline{\Delta V_s^2} = \frac{1}{A}\left(\frac{q}{\epsilon}\right)^2 S_{n_t}(\omega) X_1^2 \Delta X, \qquad [6]$$

where X_1 is the distance between the location of the noise source and the conduction channel, ΔX is the incremental distance toward the channel, and A is the gate area. The relationship between the carrier density at the surface inversion layer and the surface potential is[8]

$$Q_n = -(V_G - V_{FB} - V_s)C_0 - Q_B. \qquad [7]$$

Therefore,

$$\Delta Q_n = C_0 \Delta V_s, \qquad [8]$$

where V_G is the gate voltage. If V_D is the drain bias voltage and Z and L are the width and the length of the gate, respectively, the spectral intensity of the fluctuation of the output current is

$$\Delta S_i(\omega) = \left(\frac{Zq\mu V_D C_0}{L\epsilon}\right)^2 \frac{4N_t f_t f_{tp} X_1^2 \Delta X}{Cn_1 A\left(1 + \omega^2 \dfrac{f_{tp}^2}{C^2 n_1^2}\right)}. \qquad [9]$$

To obtain the total output noise we must integrate Eq. [9] through the depletion region. Since the trap state most susceptible to fluctuation is one-third occupied, the Fermi–Dirac distribution function must be used for f_t and f_{tp}. The relationship between X_1 and the local voltage, V, is also a very complex function. The charge density in the depletion region is equal to the sum of the densities of ionized donor states and the trapped electrons. The charge density is, therefore, not uniformly distributed through the space-charge region. The integration of Eq. [9] can only be made by computer. An approximate solution is desirable.

It can be shown that the mean square output noise current is one-half of its maximum value at $f_t = \frac{2}{3}$ and $f_t \approx 0.09$. An exact solution for the noise half-power points is also difficult to obtain. For the sake of simplicity we assume that the trap density is uniformly distributed in the depletion region. After some manipulations the distance between these half-power points, ΔX, is found to be

$$\Delta X \approx \frac{kT}{2q}\left[\frac{\epsilon}{(E_t - E_{FP})N}\right]^{1/2}. \qquad [10]$$

Thus, for a space-charge density of 10^{16} cm^{-3} the distance ΔX is nearly equal to 0.03 μm. In this region f_{tp} changes from 0.33 to 0.91. Outside of this region ΔS_i decreases very rapidly. Therefore, we may assume that only those trap states whose occupancy probability is between 0.67 and 0.09 contribute low-frequency excess noise to the device. We also may assume that X_1 is equal to the distance between the channel and the one-third-occupied trap state:

$$X_1 \approx \left[\left(\frac{E_{FP}}{q}\right)^{1/2} - \left(\frac{E_t - E_{FP}}{q} - \frac{kT}{q}\log 2\right)^{1/2}\right]\left[\frac{2\epsilon}{qN}\right]^{1/2}. \qquad [11]$$

From Eq. [9] the corner frequency, ω_c, defined as the frequency where the noise power is ½ of that at low frequencies, is

$$\omega_c = \frac{Cn_1}{f_{tp}}. \qquad [12]$$

Since f_{tp} changes from 0.33 to 0.91, the time constant dispersion of trapping noise in MOSFET's is very small. Consequently, the spectrum of the trapping noise can be approximated as having a single time constant. This property is very similar to that of g-r noise in forward-biased metal–semiconductor Schottky-barrier diodes.[7]

Substituting X_1 and ΔX into Eq. [9] yields

$$S_i(\omega) \approx \frac{16N_t kT}{27NC_{n1}\epsilon A}\left[\frac{\epsilon}{N(E_t - E_{FP})}\right]^{1/2}\left[\frac{Z\mu V_D C_0}{L}\right]^2 \times \frac{\left[\left(\frac{E_{FP}}{q}\right)^{1/2} - \left(\frac{E_t - E_{FP}}{q} - \frac{kT}{q}\log 2\right)^{1/2}\right]^2}{1 + \left(\frac{2\omega}{3C_{n1}}\right)^2}. \qquad [13]$$

The drain output noise is independent of the gate biases but increases with the square of the drain bias voltage. The corner frequency given by Eq. [13] is independent of the bias voltages. Since the temperature dependence of C is expected to be small, the temperature activating energy of ω_c is the same as that of n_1. Therefore, by measuring ω_c as a function of temperature, the energy of the trap state can be determined. From Eq. (13) the density of the trap state can be obtained:

$$N_t \approx \frac{9N\omega_c \epsilon A S_i(0)}{8kT} \times \frac{\left[\frac{N(E_t - E_{FP})}{\epsilon}\right]^{1/2}\left[\frac{L}{ZMV_D C_0}\right]^2}{\left[\left(\frac{E_{FP}}{q}\right)^{1/2} - \left(\frac{E_t - E_{FP}}{q} - \frac{kT}{q}\log 2\right)^{1/2}\right]^2}, \qquad [14]$$

where $S_i(0)$ is the low frequency plateau of $S_i(\omega)$.

In a p-channel MOSFET, the physical process of electron trapping noise is different from what has been described. After perturbation by the fluctuation of the charge density at the trap states, the free electrons in the conduction band tend to recover to the equilibrium value through the region close to the silicon–sapphire interface. It is well understood that the conductivity in this region is very poor.[9,10] The field intensity parallel to the channel in this region is nearly equal to zero when the device is operated in the linear region. The electrons are, therefore, dependent on a diffusion mechanism to recover to the equilibrium density. Since the hole density at the silicon–sapphire interface is very small, the

surface recombination at that region is also small. The perturbed electrons are either trapped at the silicon–sapphire interface or diffuse to the source or drain. The time constant of this process is different from that given by Eq. [2]. Since the diffusion time of the perturbed electrons increases with distance, the universal 3/2 power law of diffusion noise[11,12] may not be observed, even if the excess noise is purely dominated by diffusion process.

3. Experiments

The devices used in this experiment were made on thin silicon film deposited on sapphire substrates. The typical thickness of the silicon films was 0.6 μm. The doping concentrations of the film were varied from 10^{15} to 10^{17} cm^{-3}. Devices with both circular and linear geometries were used.

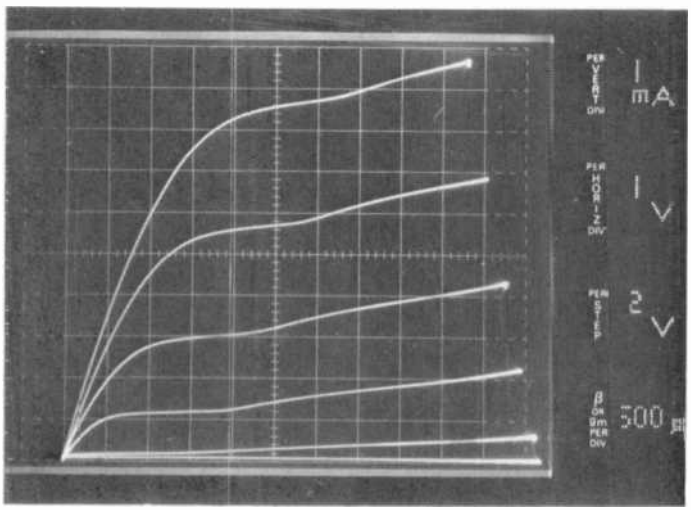

Fig. 1—Typical drain characteristics of an n-channel SOS MOSFET.

The periphery of the gate of a circular device is completely surrounded by a diffused region, while part of the periphery of a linear geometrical device is at the edge of the silicon mesa. The noise data obtained from these two types of devices are very similar. This result indicates that the trapping noise is not due to the periphery or edge effect.

Typical drain current–voltage characteristics of an n-channel SOS MOSFET are shown in Fig. 1. A current kink in the 4 to 6 volt drain bias region is observed. The onset voltage of the current kink increases with

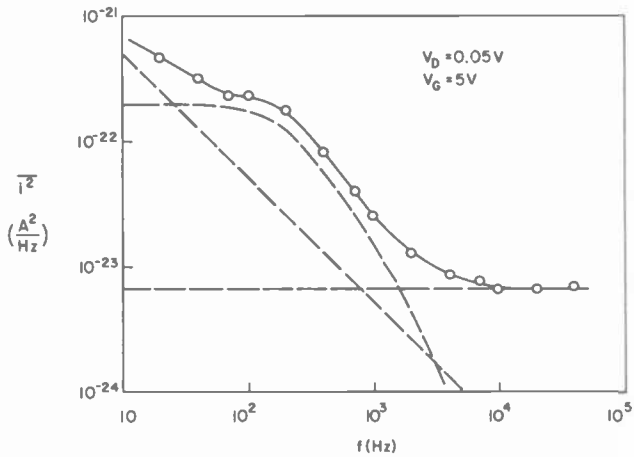

Fig. 2—Noise spectrum of a typical n-channel SOS MOS transistor operated in the linear region.

gate bias voltage. The characteristics and the physical model for this current kink are discussed in a separate paper.[13]

The typical noise spectrum of an n-channel SOS MOSFET operated in the linear region is shown in Fig. 2. It is clearly shown in the figure that at very low frequencies the device noise has $1/f$ frequency dependence.

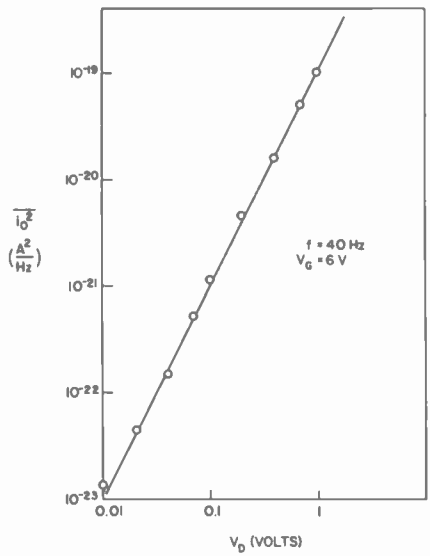

Fig. 3—Low-frequency plateau of trapping noise spectra versus drain bias voltage.

At high frequencies, the noise of the device is independent of the frequency. This noise spectrum can be considered as the superposition of three components, as shown by the broken lines—the frequency-independent component, the 1/*f* noise, and the generation–recombination type noise. Subtracting the 1/*f* noise and the frequency-independent noise from the measured data, we obtained a g-r type noise spectrum. The g-r type noise is caused by electron trap states. This noise spectrum has a single time constant in good agreement with the approximation made in the previous section. The corner frequency in this case is found to be 250 Hz. The low-frequency plateau is 2×10^{-22} A^2/Hz. From Eq. [14] the trap density is found to be 2×10^{15} cm^{-3}.

The low-frequency plateau of the trapping-noise spectrum is plotted as a function of drain bias voltage in Fig. 3. As expected from Eq. [15], the low-frequency plateau of the trapping noise in SOS MOSFET's is

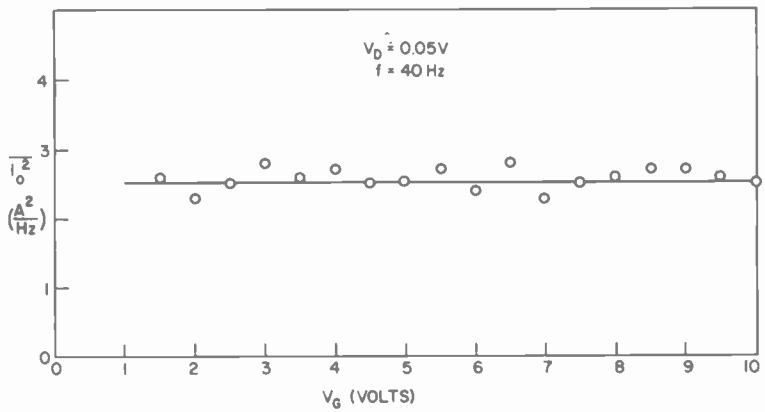

Fig. 4—Low-frequency plateau of trapping noise spectra versus gate bias voltage.

proportional to the square of the drain bias voltage. The gate bias voltage dependence of the low-frequency plateau and the corner frequency of the trapping-noise spectra are plotted in Figs. 4 and 5, respectively. As predicted in the previous section, the low-frequency plateau and the corner frequency of the trapping noise are found to be gate-voltage independent. The experimental results also show that the corner frequencies of the trapping-noise spectrum is independent of drain bias voltage.

The temperature dependence of the low-frequency plateau and the corner frequency of the trapping noise spectra are shown in Fig. 6, where it is clear that the corner frequency decreases exponentially and the

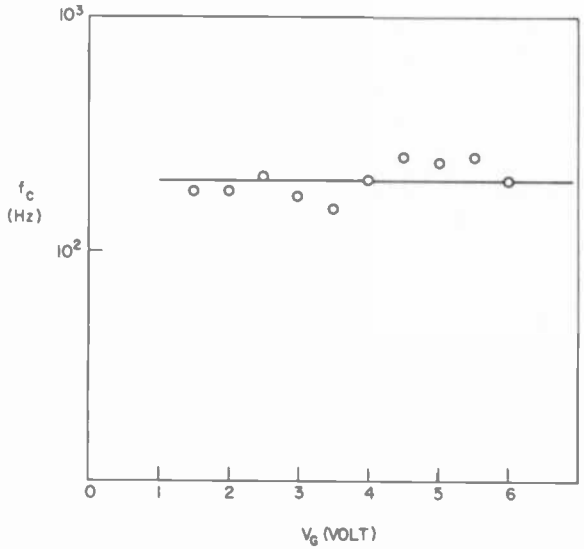

Fig. 5—Corner frequency of trapping noise spectra versus gate bias voltage.

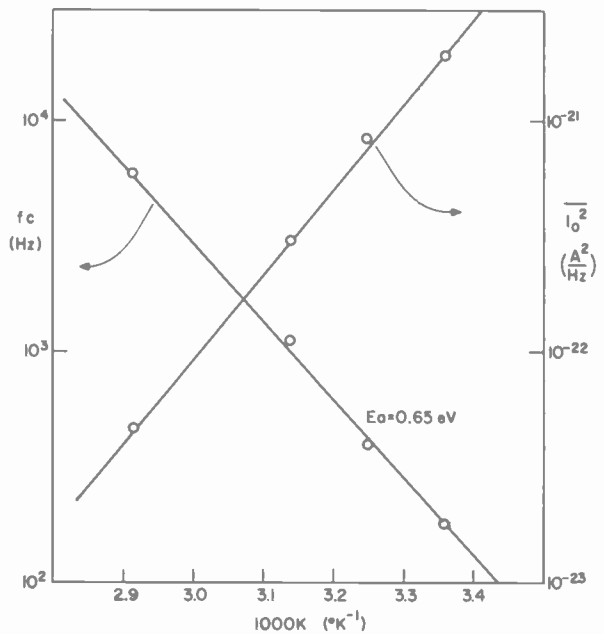

Fig. 6—Temperature dependence of the corner frequency and the low-frequency plateau of trapping noise spectra.

low-frequency plateau increases exponentially with the increase of the reciprocal of the absolute temperature. From the slope of the ω_c versus $1/T$ curve, the activation energy of the corner frequency is found to be equal to 0.65 eV. Consequently, the electron trap state is located at 0.65 eV below the edge of the conduction band. This is consistent with what we found from the noise measurement of a SOS MOSFET operated in the saturation region.[4] When we substitute $f_c = 200$ Hz and $E_t = 0.65$ eV into Eq. [14], the capture cross section of the electron trap states is found to be 5×10^{-15} cm^2. However, from a large number of devices we found that there is approximately one order of magnitude deviation in capture cross section. The low-frequency plateau of trapping noise also has an activation energy nearly equal to 0.65 eV, as expected from Eq. [14].

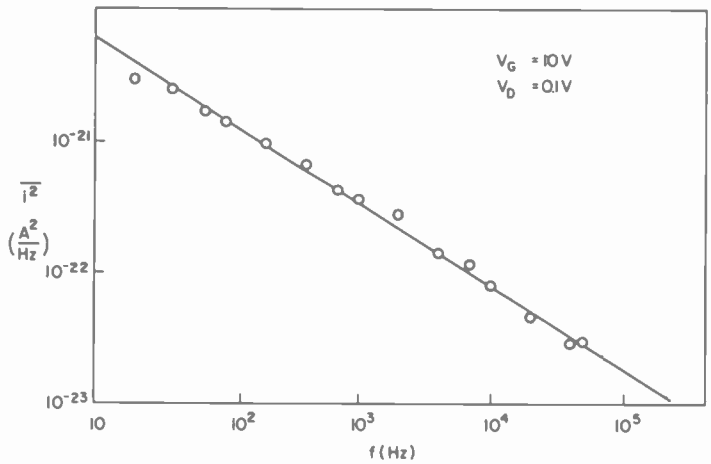

Fig. 7—Noise spectrum of a typical p-channel SOS MOSFET operated in the linear region.

The typical drain-current–voltage characteristic of p-channel SOS MOSFET's exhibits no current kink. The noise spectrum of a typical p-channel SOS MOSFET operated in the linear region is shown in Fig. 7. The output noise power has $f^{-\alpha}$ frequency dependence. In this particular device α is nearly equal to unity. Since the noise time constant has a large dispersion, the trap energy and the density of the trap state cannot be obtained from this measurement. Experimental results also show that the low-frequency noise power is proportional to the square of the drain bias voltage and is independent of the gate bias. These results suggest that the low-frequency noise of the device is due to the

fluctuation of surface potential. However, it is not possible to distinguish the effect of the silicon–sapphire interface states based on the above experiment.

4. Conclusion

Theoretical and experimental studies on trapping noise in SOS MOSFET's due to trap states in the depletion region have been made. It is shown that the fluctuation of charge density in electron trap states produces a long-time-constant noise due to charge-density fluctuation in trap states, which in turn produces low-frequency excess noise in the drain current. The trap state most susceptible to fluctuation is one-third occupied. Only those nearly one-third-occupied trap states contribute significant noise to the device. Consequently, the electron trapping noise in n-channel thin MOSFET's exhibits a nearly single-time-constant noise spectrum. The trap energy, the trap state density, and the capture cross section of the trap state can be obtained from noise measurements. In our SOS film, the electron trap state is located at 0.65 eV below the edge of the conduction band, the density and the capture cross section of the electron trap states are of the order of 10^{15} cm^{-3} and 10^{-15} cm^2, respectively.

The characteristics of electron trapping noise in p-channel thin-film MOST's is very complex. A detailed knowledge of the characteristics of silicon–sapphire interface state, the properties of silicon near the silicon–sapphire interface, and the carrier transport mechanism in that region must be known in order to predict the characteristics of electron trapping noise of the devices.

Acknowledgment

The author wishes to express his indebtedness to L. C. Lucas for the noise measurements.

References

[1] A. van der Ziel, "Carrier Density Fluctuation Noise in Field Effect Transistors," *Proc. IRE*, 51, p. 1670 (1963).

[2] C. T. Sah, "Theory of Low Frequency Generation Noise in Junction Gate Field Effect Transistors," *Proc. IEEE*, 52, p. 795 (1964).

[3] P. O. Lauritzen, "Low Frequency Generation Noise in Junction Field Effect Transistors," *Solid State Elect.*, 8, p. 41 (1965).

[4] S. T. Hsu, 1972 Noise Symposium, University of Florida, Gainesville, Fla.

[5] A. van der Ziel, *Noise, Source, Characterization, Measurement*, Chapter 5, Prentice-Hall, Englewood Cliffs, N.J. (1970); also, K. M. van Vliet and J. R. Fassett, *Fluctuation Phenomena in Solids*, Chapter VII, Edited by R. E. Burges, Academic Press, N.Y. (1965).

[6] A. van der Ziel, *Fluctuation Phenomena in Semiconductors*, p. 25, Butterworth, London, England (1959).

[7] S. T. Hsu, "Low-Frequency Excess Noise in Metal-Silicon Schottky Barrier Diodes," *IEEE Trans. Electron Devices*, **ED-17**, No. 7, p. 496 (1970).

[8] A. S. Grove, *Physics and Technology of Semiconductor Devices*, Chapter 9, John Wiley and Sons, Inc., New York (1967).

[9] S. T. Hsu and J. H. Scott, "Mobility of Current Carriers in Silicon-on-Sapphire (SOS) Films," *RCA Review*, **36**, No. 2, p. 240 (1975).

[10] A. C. Ipri, "Variations in Electrical Properties of Silicon Films on Sapphire Using the MOS Hall Technique," *Appl. Phys. Lett.*, **20**, No. 1, p. 1 (1972).

[11] K. M. van Vliet and A. van der Ziel, "On the Noise Generated by Diffusion Mechansims," *Physics*, **24**, p. 415 (1958).

[12] K. S. Champlin, "On the Influence of Diffusion and Surface Recombination Upon the G-R Noise Spectrum of Semiconductors," *Physics*, **26**, p. 751 (1960).

[13] S. T. Hsu, 'Drain Characteristics of Thin-Film MOSFET's," *RCA Review*, **38**, No. 1, p. 139 (1977).

A Novel FET Frequency Discriminator*

A. Rosen, D. Mawhinney, and L. S. Napoli

RCA Laboratories, Princeton, N. J. 08540

Abstract–We have developed wideband GaAs FET microwave frequency discriminators that are smaller and perform better than the conventional interferometer type. The new discriminators consist of a 1.0 × 1.3-cm thin-film ceramic circuit on which are mounted a GaAs FET chip and an Si beam-lead Schottky diode. A typical discriminator instantaneously covers the frequency range from 7 to 11 GHz, producing a dc output voltage ranging from approximately −200 MV at 7 GHz to +300 MV at 11 GHz for an input of 0.2 mV. Compared to the interferometer-type discriminators, the FET discriminators provide approximately 10 times larger output voltages for the same rf input.

Introduction

One important application for wideband microwave discriminators is in frequency memory systems, where the device is used to provide an accurate analog voltage related to frequency for open-loop VCO set-on or closed-loop VCO frequency control. For either function, a linear relation between input frequency and output voltage is desirable but not essential. The use of post-detection voltage processing or linearization can compensate for overall nonlinearity to a considerable degree. In this paper we describe a novel FET discriminator consisting of an integrated microwave GaAs FET chip and an Si beam-lead Schottky diode. The high frequency gain roll-off of the FET augmented by an

* The research reported in this paper was sponsored in part by the Naval Electronic System Command, Washington, D.C., under Contract No. N00039-76-C-0280 and RCA Laboratories, Princeton, N.J.

input shaping network and biasing networks, provided the desired wideband discriminator characteristic.

Techniques for the rapid and accurate determination of unknown signal frequencies are of considerable interest in modern military electronic systems. A microwave interferometer employing 3-dB hybrid couplers to split and later recombine the incoming signal after transmission through unequal path lengths is frequently used for this application.

The FET discriminator discussed in this paper provides a greater output voltage swing for a given limiter output power, less fine-grain structure, smaller volume, and potentially lower cost. The new discriminator consists of a 1.0 × 1.3 cm thin-film ceramic circuit on which are mounted a GaAs FET chip and an Si beam-lead Schottky diode. The Schottky diode detector is dc isolated from the FET drain circuit by a ceramic chip blocking capacitor, and is forward biased to a current of between 0.1 and 1.0 mA through a dropping resistor and an rf choke.

Basic Considerations

The discriminator circuit most widely used today is the passive interferometer type, shown schematically in Fig. 1. A preleveled rf signal is divided into two channels of unequal electrical length. The resulting

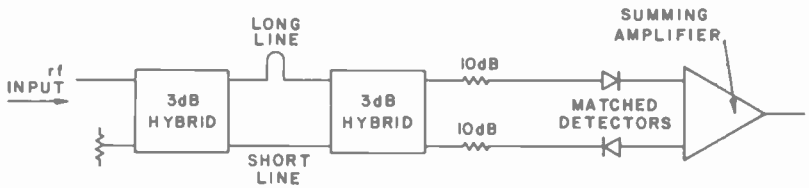

Fig. 1—Long-line/short-line pulse interferometer used for frequency discriminator.

signals, displaced in phase, are recombined and detected, resulting in a voltage output that is a function of the frequency of the input signal.[1-3] Problems with this type of device have been related to the need to very accurately match the various elements of the two paths–the hybrid couplers crystal detectors, diodes, connectors, etc. To ensure a frequency resolution of ±1 MHz in a 4-GHz band, mismatches of less than 1.05:1 in VSWR would be required, a figure that is not achievable in practice. In addition, input rf power variations across the band of interest must be restricted to a fraction of a dB, which places major constraints on the design of the limiter at the input of the discriminator circuit.

Even when the discriminator circuits are fabricated in MIC (micro-

wave integrated circuit) form, thereby greatly reducing the line length and eliminating many interconnection problems, a phase interferometer of this general design still produces a nonlinear frequency error equivalent to ±50 MHz in the 7 to 11-GHz band.[4] A different concept of a discriminator circuit is clearly required.

FET Discriminator Design Approach

A completely different approach to the problem of converting a pulsed microwave signal to a voltage that is an accurate measure of the microwave frequency is based on the utilization of the transfer function of a broadband microwave amplifier using GaAs Schottky-barrier field-effect devices.

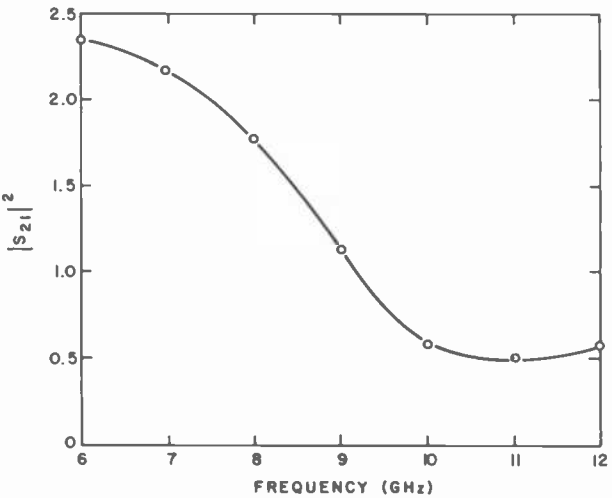

Fig. 2—Typical transfer function of untuned FET amplifier.

Fig. 2 shows a typical transfer function of an untuned GaAs FET amplifier. As can be seen, the output is a monotonic, although not linear, function of frequency. It is this intrinsic property of the FET amplifier that is utilized in the frequency-discrimination embodiment. Input and output shaping networks are designed (using computer optimization routines) to provide maximum linearity over the band of interest.

A discriminator based on this approach was designed and described by Z. Turski, D. Mawhinney, and I. Drukier.[5–8] Its performance is compared to that of an interferometer-type unit driven from the same limiter in Fig. 3. The figure also shows the output when the FET dis-

criminator is removed. The output curves of Fig. 3 depict some of the following basic characteristics of an FET discriminator:

(1) For a given frequency band and a given power input, the FET discriminator provides a greater voltage swing than does the interferometer type;
(2) Linearity of output can be achieved with proper matching networks at the input and output of the FET;
(3) The output of the discriminator reflects the irregularities of the limiter driving it.

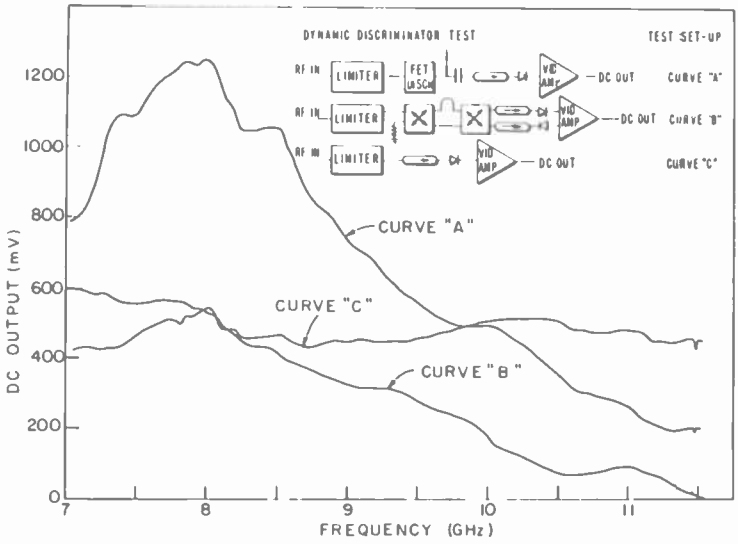

Fig. 3—Dynamic performance curves of early 8- to 11-GHz FET discriminator. Curve A is for active FET discriminator, B is for passive interferometer type discriminator, and C is the power feed through reference.

FET Discriminator Design Considerations

The basic discriminator circuit consists of a GaAs FET chip and an Si beam-lead Schottky detector diode mounted on a thin-film circuit on a ceramic substrate. The detector diode is dc-isolated from the FET drain circuit by a ceramic-chip blocking capacitor, and is forward biased to a current between 0.1 to 1.0 mA. Input and output response shaping for optimization of linearity and slope are utilized, but dissimilar approaches are employed in the FET input and output circuits, as explained below. A functional block diagram of the FET discriminator is shown in Fig. 4.

Table I—Input and output scattering parameters of a typical FET chip for two values of drain voltage.

Frequency	S_{11}		S_{22}	
V_G = 0, V_D = 3V, I_D = 50 MA				
7000.0	.785	−148	.684	−87
7200.0	.760	−153	.671	−89
7400.0	.748	−161	.648	−91
7600.0	.751	−166	.642	−93
7800.0	.739	−170	.625	−96
8000.0	.736	−178	.604	−100
8200.0	.750	174	.583	−105
8400.0	.776	170	.564	−110
8600.0	.777	166	.550	−116
8800.0	.787	161	.549	−122
9000.0	.822	157	.556	−128
9200.0	.845	152	.562	−136
9400.0	.845	150	.568	−143
9600.0	.856	146	.585	−149
9800.0	.855	142	.602	−154
10000.0	.858	140	.620	−160
10200.0	.869	138	.642	−163
10400.0	.849	135	.664	−167
10600.0	.835	133	.685	−171
10800.0	.835	131	.703	−174
11000.0	.816	129	.719	−177
V_G = 0, V_D = 8V, I_D = 50 MA				
7000.0	.770	−152	.839	−82
7200.0	.743	−157	.831	−84
7400.0	.734	−165	.813	−86
7600.0	.740	−170	.813	−88
7800.0	.735	−174	.798	−91
8000.0	.731	177	.784	−95
8200.0	.744	170	.768	−99
8400.0	.771	166	.756	−104
8600.0	.775	162	.745	−109
8800.0	.786	157	.742	−115
9000.0	.812	153	.745	−121
9200.0	.837	149	.747	−128
9400.0	.839	147	.752	−134
9600.0	.851	143	.766	−140
9800.0	.850	139	.777	−145
10000.0	.856	137	.795	−151
10200.0	.865	135	.809	−156
10400.0	.843	132	.829	−160
10600.0	.829	130	.846	−165
10800.0	.827	128	.855	−167
11000.0	.807	126	.867	−171

FET Chip Characteristics

The basic concept of the FET discriminator requires the maximum gain of the active device only at the lowest frequency, while frequency roll-off characteristics are optimized to provide the desired output versus frequency performance. It was noted that varying the drain voltage of the FET results in considerable variations in the device output impedance, while maintaining a constant FET input impedance. An example of this effect is shown in Table 1, where S_{11} and S_{22} scattering parameters of a typical FET chip are shown for two values of device drain voltage (V_D = 3 and 8 V) over the 7- to 11-GHz frequency range. This property can be used to optimize the discriminator output circuit.

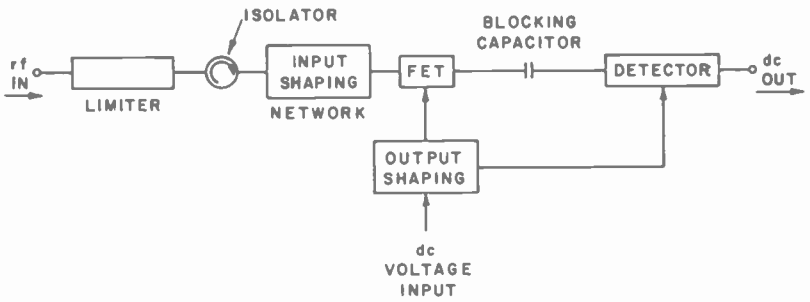

Fig. 4—Functional block diagram of FET discriminator.

Linearization And Slope Optimization

While a true linear relationship between input frequency and output voltage is usually not essential in most receiver subsystems (since post-detection voltage processing and linearization can be used), linear transfer characteristics are nevertheless highly desirable and frequently simplify circuit design.

Linearization of the discriminator characteristic is accomplished by shaping arrangements at the input and output of the FET chip. The input network uses the conventional approach of selecting a microwave matching circuit geometry and adjusting it for linear output with the aid of computer-aided optimization routines. For the output circuit, however, it was thought prudent to adjust the output of the FET by purely electronic means, as opposed to circuit-geometry approaches. The large FET output impedance variability as a function of drain voltage changes, discussed in the preceding section, provides such an adjustment

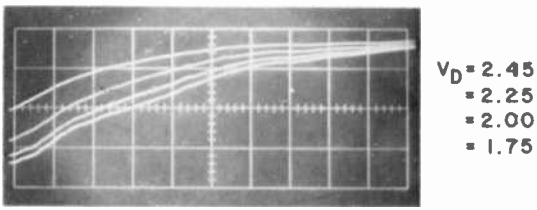

Fig. 5—Effect of drain voltage variation on FET discriminator output characteristics.

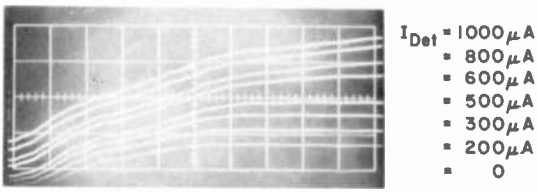

Fig. 6—Effect of detector bias on FET discriminator output characteristic.

mechanism. The elimination of an output-matching microwave transmission line helps to eliminate a source of multiple reflections and discontinuities that tend to introduce irregularities in the discriminator output characteristic. An example of the effect of drain-voltage variations on the discriminator output response is shown in Fig. 5. As can be seen, the most pronounced effect on the shape of the output curve is at the

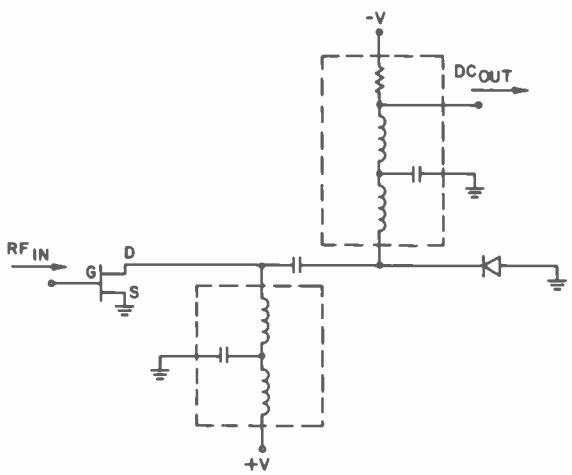

Fig. 7—Output shaping arrangements for FET discriminator.

low-frequency end of the band. In addition to changes in the linearity of the output curve, the slope can also be varied, so that the output voltage swing can be changed as a function of drain voltage.

Another means of affecting the shape of the discriminator output (as a function of input frequency) is afforded by adjustments in the forward-bias current of the detector diode, as shown in Fig. 6. Here, the greatest effect appears to take place at the high-frequency end of the operating band. Again, the adjustment affects both the slope and the linearity of the video output.

The effectiveness of these electronic adjustments and the apparent complementary nature of the two approaches (drain voltage affecting the lower frequencies, detector bias affecting the high-frequency end) led us to adopt the electronic "shaping" approach at the discriminator output, while using the more conventional microwave matching network at the FET input. The basic scheme is shown in Fig. 7.

Effect Of Limiter Characteristics

The accuracy of power-leveling at the input to the discriminator can be expected to have a profound effect on the accuracy of frequency-to-voltage conversion, and the experimental data confirm the need for precise limiting of the input signal over the band of operation. The expanded x-y recorder plots of the limiter output and the discriminator response, shown in Figs. 8 (A) and 8 (B), clearly indicate the correspondence of the irregularities in the discriminator output to the imperfections in the limiting at its input. Indeed, it is the lack of smooth power leveling that actually limits the overall frequency band over which the FET discriminator can be used in a practical system. For instance, the final limiter–discriminator unit actually performs over the 7.5 to 11-GHz band (rather than the desired 7- to 11-GHz range) due to irregularities in the limiter performance in the 7- to 7.5-GHz region. While these considerations apply equally to interferometer- and FET-type discriminators, the crucial dependence of the broadband discriminator response on the excellence of limiting was less evident with the older designs, because it was masked by the multiple reflections in the short-line/long-line discriminator arrangements.

Experimental Results

A. Discriminator Circuit

A breadboard discriminator based on the approach outlined above has been tested. Fig. 9 is a photograph of the discriminator including integral

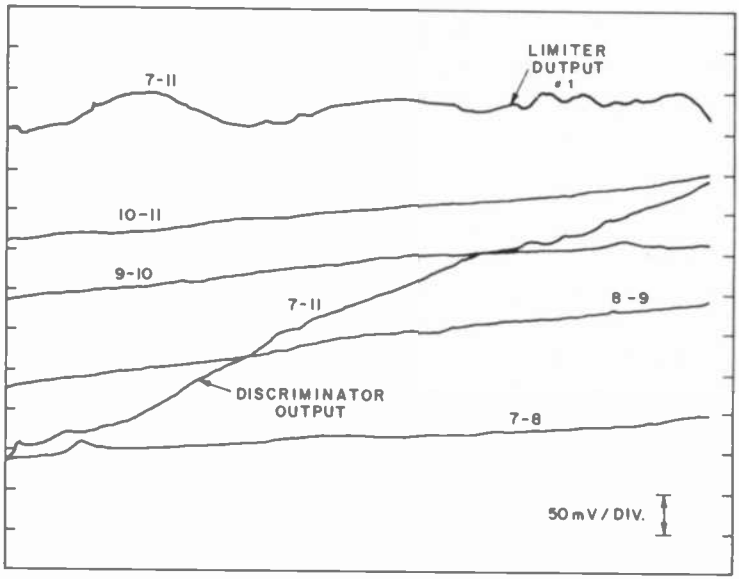

(a)

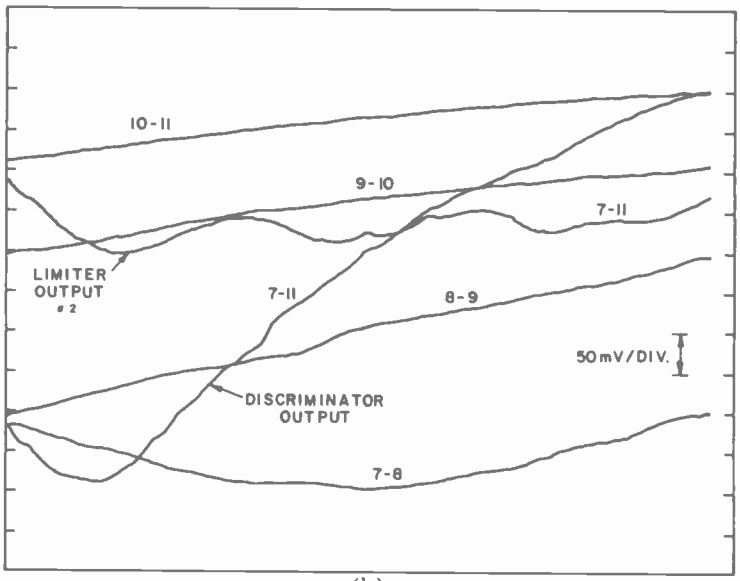

(b)

Fig. 8—Expanded x-y recorder plots showing effect on discriminator output of irregularities in limiter input: (a) for limiter #1 and (b) for limiter #2.

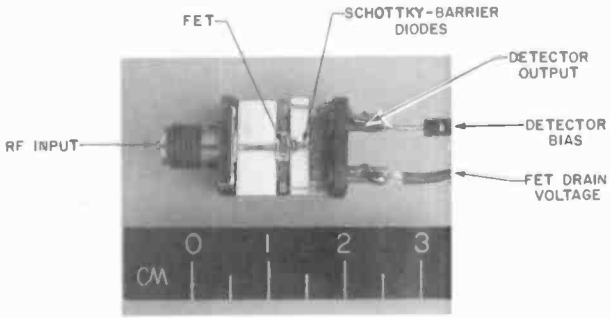

Fig. 9—FET descriminator.

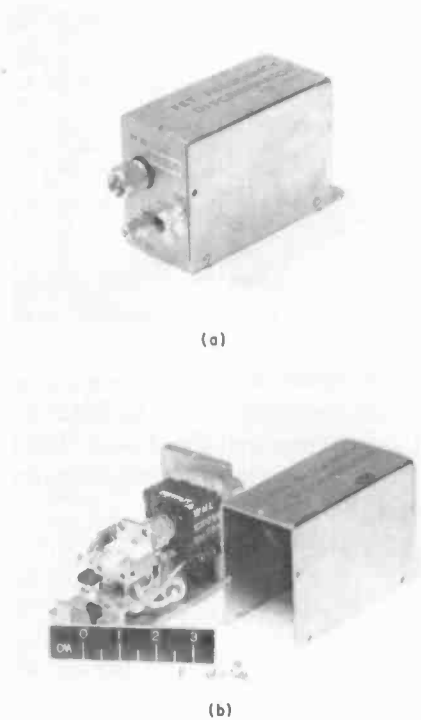

Fig. 10—FET discriminator (a) packaged and (b) with cover removed showing circuit components.

detector; Fig. 10 shows both the packaged discriminator and a view of circuit contents with the cover removed. The overall assembly consists of an input isolator, the FET amplifier stage, detector, and MIC assembly, and a voltage regulator to stabilize the drain voltage.

The discriminator assembly unit, operating in conjunction with a TDA limiter,* operates over the frequency range 7.5 to 11 GHz (Fig. 11).

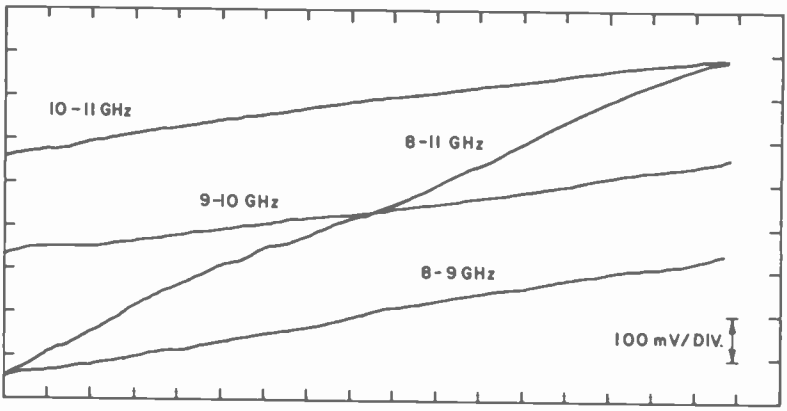

Fig. 11—FET discriminator operation (7.5 to 11 GHz).

B. Discriminator Noise Output

Measurements have been made to determine the video noise output of an FET discriminator. Fig. 12(a) shows the overall voltage output versus frequency. The intensified spot, expanded by a factor of 100 to 1 mV is shown in Fig. 12(b). The resulting noise level is measured by the width of the trace in Fig. 12(b), which is comparable to the width of the trace on the scope when the input is disconnected (Fig. 12(c)). The total frequency-noise equivalency of the measured noise voltage would therefore cause an estimated error of less than 1 MHz.

C. High-Frequency Unit

A unit designed around a GaAs FET device that has a maximum available gain in excess of 6 dB at 15 GHz was fabricated and tested over the 14.5- to 16.7-GHz frequency band. A special GaAs Schottky-barrier

* Aercom Model AL-78005 S/N 192.

detector developed by RCA[10] was employed in this discriminator. Performance is shown in Fig. 13 for three different matching adjustments. While these are preliminary results, they are very encouraging in terms of the monotonic output voltage versus input frequency at these short wavelengths.

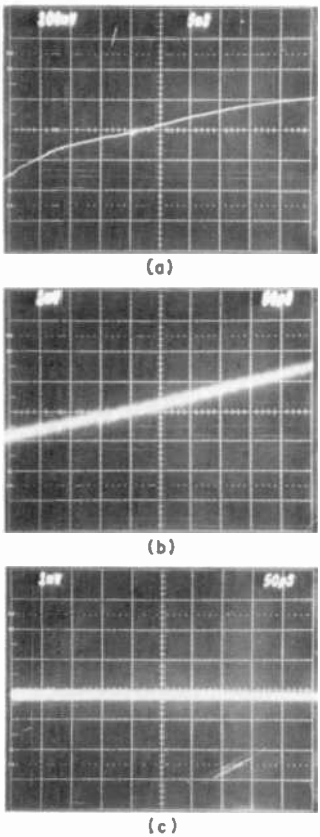

Fig. 12—FET discriminator output showing noise characteristics.

D. Discriminator Used in VCO Memory System

An early model of an FETdiscriminator was used in a locked-open-loop VCO frequency memory system. An interferometer-type discriminator which had been experimented with in that equipment, exhibited considerable fine-grain structure, which caused significant frequency error.

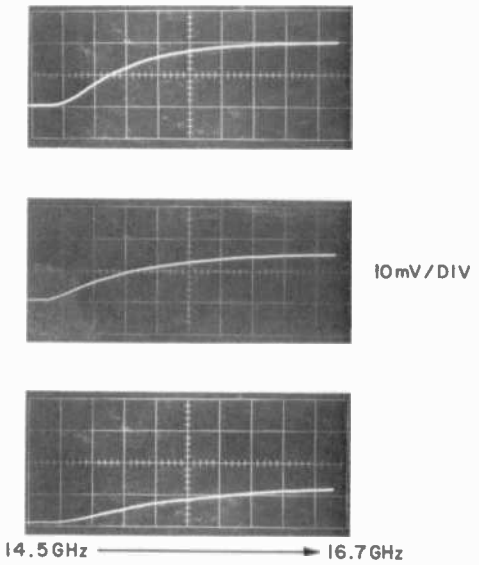

Fig. 13—Ku-band discriminator performance.

The FET discriminator that was used greatly reduced this error and provided, in addition, a larger output voltage swing.[9]

A comparison of the interferometer-type discriminator and an experimental version of an FET discriminator (without the integrated detector and isolator used in the final model of the system) is shown in Fig. 14. The dramatic reduction in size and weight is evident.

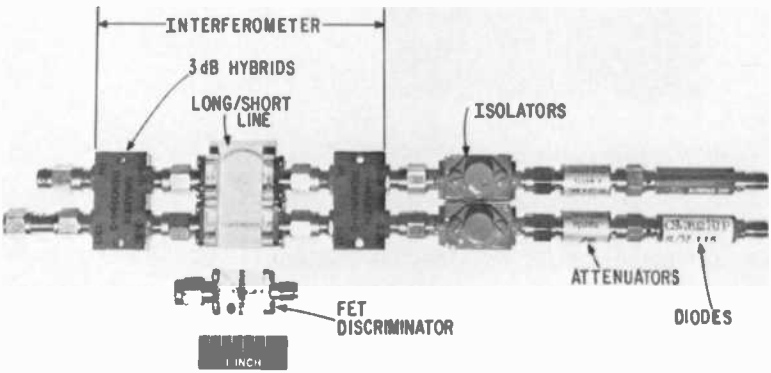

Fig. 14—Comparison of interferometer-type discriminator and FET discriminator circuit.

Although more recently fabricated FET discriminators have been improved in this respect, the output of the one installed in the frequency memory system departs considerably from a linear slope, but the change is smooth and gradual. Except for the bumps from the limiter in the region of 9.0 GHz, the FET discriminator is free from noticeable fine-grain structure, as shown by the oscilloscope photograph of Fig. 15(a). This shows the discriminator output for a swept frequency input from 8 to

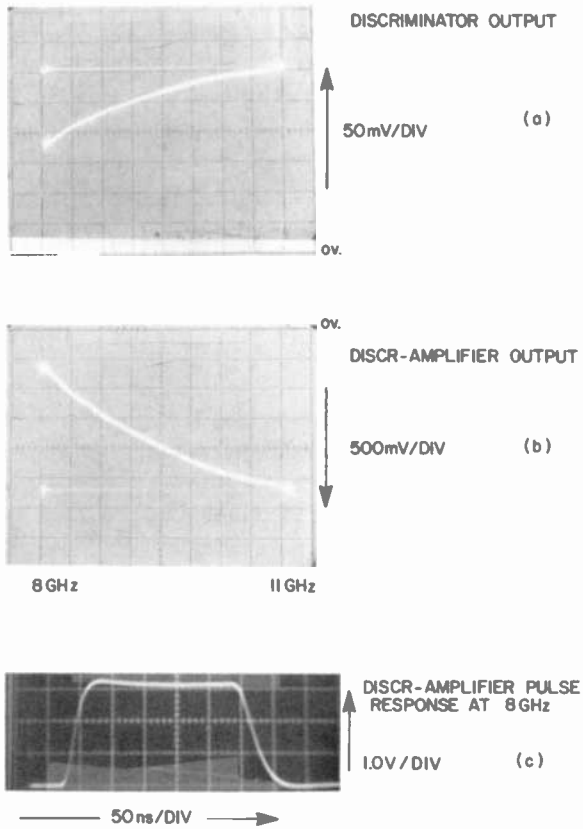

Fig. 15—Discriminator performance (VCO memory system unit).

11 GHz. The final adjustment of the drain voltage resulted in a voltage output swing of 160 mV for this same frequency range.

The FET discriminator is followed in the circuit by a video amplifier stage consisting of a high-speed hybrid operational amplifier set to a gain of approximately 17 to provide about a 2.5-V swing for driving the li-

nearizer through the follow-and-hold module. The swept output of the amplifier stage is shown in Fig. 15(b). and the pulse response is shown in Fig. 15(c) with the limiter/discriminator/amplifier combination driven by an 8-GHz, 250-ns input pulse. The extremely fast response capabilities of the FET discriminator are clearly demonstrated by these photographs.

Conclusions

A novel frequency discriminator suitable for use in EW receivers has been designed.

Compared to a dual-line MIC interferometer design, the FET discriminator provides higher output voltages, faster response time, better linearity, a smoother output response, and an inherently wider bandwidth. Moreover, its weight is less than one-third and its volume about one-quarter that of the interferometer-type unit.

A typical discriminator instantaneously covers the frequency range from 7 to 11 GHz producing a dc output-voltage swing of 500 mV.

Acknowledgments

The cooperation of the late J. Napoleon in providing the FET, and of E. Denlinger in providing the GaAs Schottky-barrier diodes is acknowledged with gratitude. In addition, the authors wish to express their appreciation to H. Wolkstein and W. W. Siekanowicz for critical review of this manuscript, and to E. Mykietyn for diligent circuit assembly and device testing.

References:

[1] R.J. Mohr, "Broadband Microwave Discriminator," IEEE Trans. Microwave Theory and Tech., 11, p. 263, July 1963.

[2] S.J. Robinson, "Comment on Broadband Microwave Discriminator," IEEE Trans. Microwave Theory and Tech., 12, p. 255, March 1964.

[3] L. I. Reber, "Improve Performance in Phase Discriminators," Microwaves, p. 48, May 1971.

[4] U.H. Gysel and J.P. Watjen, "MIC 7 to 11-GHz Frequency Discriminator," Final Report, Contract N00039-75-C-040 (Stanford Research Institute), Sept. 1976.

[5] Z. Turski, private communication.

[6] Patent pending No. 70,204, "Microwave Frequency Discriminator Comprising an FET Amplifier," Z. Turski and D. Mawhinney.

[7] Patent pending No. 70,221, "Microwave Frequency Discriminator Comprising a One Port Active Device," A. Rosen and Z. Turski.

[8] Patent pending No. 70,994, "Improved Microwave Frequency Discriminator Comprising an FET Amplifier," A. Rosen and L. Napoli.

[9] D.D. Mawhinney, "Locked-Open-Loop, VCO Frequency Memory System," Naval Electronic Systems Command, Final Report, Contract No. N00039-74-C-0227, Nov. 1976.

[10] E. Denlinger, S.G. Liu, H. Veloric, F. Duigon, and V. Lawson, "High Performance Mixer-Diode," Digest International Electron Devices Meeting, Washington, D.C., Dec. 1976.

A Dual-Gate GaAs FET RF Power Limiter*

A. Rosen, H. J. Wolkstein, J. Goel, and R. J. Matarese

RCA Laboratories, Princeton, N.J. 08540

Abstract–This report describes a preliminary investigation of a novel rf power limiter-amplifier that makes use of a recently developed dual-gate GaAs FET stage with a small-signal gain of 7 dB and a compressive gain slope (when overdriven) of 14.8 dB at the unity gain point. When operated in the power-limiting mode, several cascaded stages of this amplifier can be used to drive a companion FET discriminator to provide unambiguous frequency-to-voltage conversion.

FET Dual-Gate RF Power Limiter

A conventional means of achieving constant output power independent of drive variation or frequency is to utilize a multistage high-gain amplifier chain. The output stages of this amplifier operate in saturation regions where the output-power variations are greatly compressed, even for large variations in the input-power range. This mode of operation is depicted for several stages in Fig. 1.

For use with a frequency discriminator, for example, to obtain a frequency accuracy of 1 MHz in a 4-GHz bandwidth, the rf-limiter output must be flat to within 0.025%. This is equivalent to an incremental power output fluctuation of 1 part in 4000, 36 dB down from saturation over the total variation in input drive range. Assuming an input drive range of 31 dB, the combined value of input power swing and output limiting

* RCA Acknowledges the support of the Naval Electronic Systems Command, under Contract No. N00039-76-C-0-0280, in the initial work associated with the FET limiter.

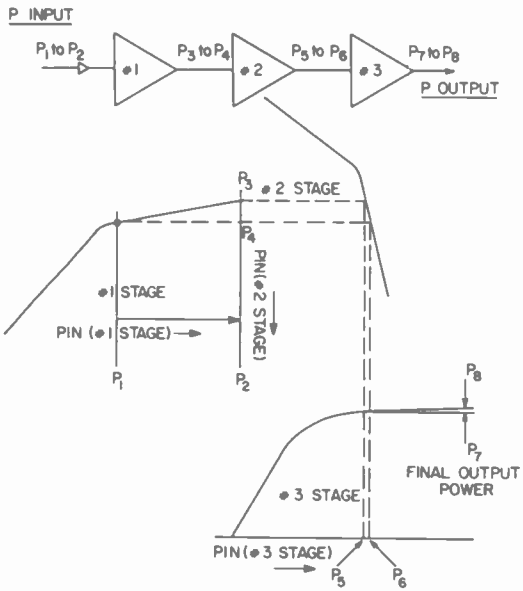

Fig. 1—A cross plot of power-input compression for a three-stage overdriven amplifier.

is equivalent to an overall compression ration of 67 dB ($1250/2.50 \times 10^{-4} = 5 \times 10^6$).

A dual-gate GaAs FET amplifier stage[1] has recently been tested in C-band with adjustments made in the operating voltage parameters to emphasize its capability to achieve rf power limiting. The resulting curve is shown in Fig. 2.[2] Using the test setup shown in Fig. 3, the rf power output of the stage, which has a small signal gain of ~ 7 dB, was driven

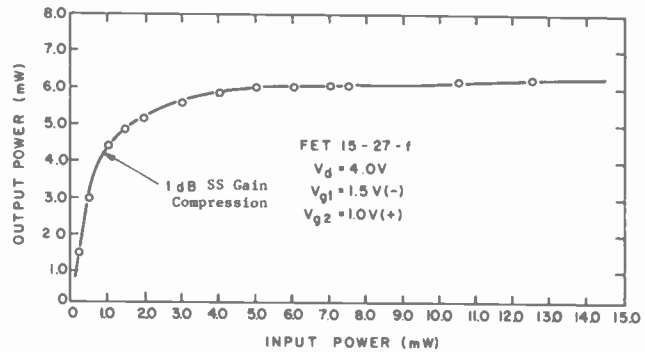

Fig. 2.—Limiting characteristics of dual-gate GaAs FET (operated at 5 GHz).

over the 0 to +15-mW input power drive range. Under these operating conditions, the stage goes to unity gain at an input drive level of 6 mW. At this approximate drive level and beyond, the compressive slope of the limiter (given by $\Delta P_{in}/\Delta P_{out}$) is 9 mW/0.3 mW or 14.8 dB. This level of power compression or limiting per stage provides an excellent capability on which to base an FET limiter–amplifier design.

The use of a dual-gate amplifier provides important functional advantages over the single-gate FET because of its flexibility.[3–5] One of the gates (G2) is adjusted to ensure proper gain level and saturation

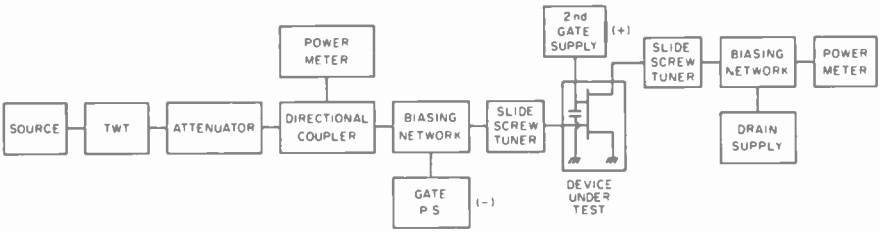

Fig. 3—Measurement setup for dual-gate FET.

operation, while the input rf signal is connected to the additional gate (G1). The dual-gate device greatly reduces the capacitance between the signal input gate and the drain electrode. This reduced capacitance provides for increased small-signal gain per stage when compared to equivalent single-gate devices with the same gate length. The dual gate also substantially reduces direct rf feedthrough from input to output; which is important in an overdrive amplifier.

Measurements were also performed to evaluate the limiting properties of the single-gate high-power FET devices of the type discussed previously by I. Drukier et al.[6] We found that the saturation characteristic of those devices was inferior to that obtained using a dual-gate FET device, and therefore a greater number of stages was required to obtain the same compression ratio.

In conclusion, we have demonstrated the use of a dual-gate FET as a limiter. Used at 5 GHz, the device has a small signal gain of 7 dB and has demonstrated a compression ratio ($\Delta P_{in}/\Delta P_{out}$) of 14.8 dB. This level of limiting per stage provides an excellent basis for the design of an FET limiter–amplifier chain. The number of stages, operating parameters, and power levels may be adjusted to fit particular operational requirements. Such a limiter, operated, for example, with an FET discriminator such as the one described in Ref. [7], represents an attractive approach for an EW receiver.

Acknowledgments

The authors wish to thank D. Mawhinney and L. Napoli for many helpful discussions and suggestions and E. Mykietyn for diligent circuit assembly and device testing.

References:

[1] R. H. Dean and R. J. Matarese, "Submicrometer Self-Aligned Dual-Gate GaAs FET," *IEEE Trans. on Electron Devices*, p. 358, June 1975.

[2] A. Rosen and D. D. Mawhinney, "FET Frequency Discriminator," Final Report, NESC Contract No. N00039-76-C-0280, Feb. 1977.

[3] Charles A. Liechti, "Performance of Dual-Gate GaAs MESFETs as Gain-Controlled Low-Noise Amplifiers and High-Speed Modulators," 1975 IEEE International Solid-State Circuits Conf., Phila., Pa.

[4] S. Asai, F. Mural, and H. Kodera, "The GaAs Dual-Gate FET with Low Noise and Wide Dynamic Range at Microwave Frequencies," Int. Electron Devices Conf. Digest of Technical Papers, p. 64 (1973).

[5] M. Maeda and Y. Minai, "Application of Dual-Gate GaAs FET to Microwave Variable-Gain Amplifier," Int. Microwave Symposium Digest of Technical Papers, p. 351 (1974).

[6] I. Drukier et al, "Medium Power GaAs Field-Effect Transistors," *Electronics Lett.*, **11**, No. 5, p. 104, March 1975.

[7] A. Rosen, D. Mawhinney, and L. S. Napoli, "A Novel FET Frequency Discriminator," *RCA Review*, **38**, p. 238, June 1977 (this issue).

Depolarization Due to Precipitation in Satellite Communications

I. P. Shkarofsky*

RCA Limited, Ste. Anne de Bellevue, Canada

Abstract—The theory on cross-polarization induced by rain on an electromagnetic wave is extended to include antenna effects. Of interest are the communication bands 4–6 and 12–14 GHz. In satellite–earth propagation links designed for frequency reuse using two orthogonal polarizations in order to double the channel capacity, the generation of cross-polarization decreases the isolation between the orthogonal channels.

We extend the analysis to include the following effects besides rain depolarization: (1) the finite clear-weather isolations and/or the co- and cross-polarization patterns of the transmitter and receiver antennas, (2) misalignment between the transmitter and receiver polarization vectors and/or Faraday rotation for linear polarization, and (3) polarization angle of a signal received off-axis from the transmitter pattern. We provide parameter plots illustrating all these effects at 4, 6, and 11 GHz, and for certain elevation angles. Results for both linear and circular polarizations are shown. Other causes of cross-polarization considered are due to interfering satellites and multipath. Compensation methods to eliminate the cross-polarization components are discussed and the theory on the rf system is elaborated.

1. Introduction

The use of two orthogonal polarizations at the same frequency is an economical method of increasing the channel capacity in satellite to earth communication links. The RCA Satcom satellite uses this concept.

* Now at MPB Technologies, Ste. Anne de Bellevue, Canada.

Several factors can however induce unwanted cross-polarization leading to cross-talk between orthogonal channels. A serious cause is rain in the lower atmosphere, which produces cross-polarization in incident waves due to the nonspherical geometry of raindrops. Another cause is associated with the clear weather finite antenna (transmitter and/or receiver) isolation between orthogonal polarizations, which varies with the off-axis angle in the antenna pattern. A third cause which can occur for noncircular waves is the possibility of the receiver polarization direction being misaligned with respect to the transmitter electric field direction. Other causes of cross-talk are associated with interference due to signals from adjacent satellites and/or signals received through multipath propagation.

The effect of antenna clear weather isolation on satellite to earth propagation through rain has been considered only in isolated papers, such as those of Bostian[1] and McCormick and Hendry.[2] Bostian uses the Stokes parameter representation for predominantly linearly polarized waves. A neater representation in terms of the linear antenna patterns is given here (see Appendix 1 which outlines both representations). McCormick and Hendry's work applies to predominantly circularly polarized waves. For this situation, we follow their method but do not assume, as they do, that the transmitter and receiver antennas are identically imperfect. A CCIR Report[3] discusses antenna effects in the absence of rain. Our results reduce to those plotted there in this limit.

Most of the final relations have already been given by Shkarofsky and Moody.[4] In the present paper, the basis of the derivations and mathematical manipulations are given, curves are plotted based on the formulas and the implications in the results are discussed.

In Section 2, we formulate the theory on attenuation and cross polarization to include antenna effects in addition to rain effects for both predominantly linear and circular transmitted waves. Particulars are given in Appendices 1 and 2. In Section 3, we give plotted results based on this analysis and discuss implications of the plots. In Section 4, we analyze three additional causes of depolarization, namely Faraday rotation, interfering satellites, and multipath propagation. Finally, Section 5 reviews the theory on compensation and cancellation systems to recover the pure polarizations.

2. Theoretical Formulation

2.1 Angles of Interest

Fig. 1 illustrates the angle of interest. The angles ϕ_T and ϕ_R are the angles that the line of sight propagation path makes with the boresight axis

of the respective antenna patterns. The satellite transmitter antenna has co- and cross-polarization antenna patterns $F_T'(\phi_T)$ and $f_T''(\phi_T)$ in dB, both normalized to $F_T'(0) = 0$. For radiation with orthogonal polarization, the corresponding patterns are $F_T''(\phi_T)$ and $f'(\phi_T)$ normalized to $F_T''(\phi_T) = 0$. The receiver patterns corresponding to the above are $F_R'(\phi_R)$, $f_R'(\phi_R)$, $F_R''(\phi_R)$ and $f_R''(\phi_R)$. To convert dB to watts, we redefine

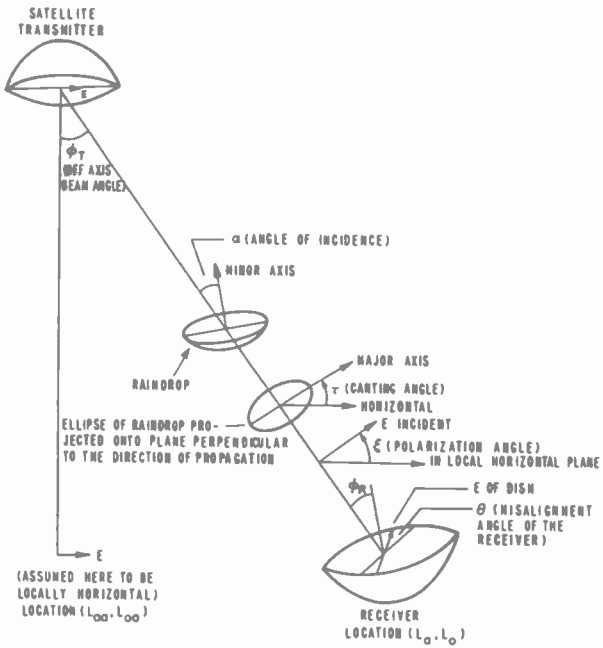

Fig. 1—Angles used in the analysis.

$$
\begin{aligned}
F_{Ta} &= 10^{F_T'/20}, \quad F_{Tb} = 10^{F_T''/20}, \\
f_{Ta} &= 10^{f_T''/20}, \quad f_{Tb} = 10^{f_T'/20}, \\
F_{Ra} &= 10^{F_R'/20}, \quad F_{Rb} = 10^{F_R''/20}, \\
f_{Ra} &= 10^{f_R'/20}, \quad f_{Rb} = 10^{f_R''/20}.
\end{aligned} \tag{1}
$$

Also let the respective on-axis antenna gains be G_T', G_T'', G_R', and G_R'' in dB, with

$$
\begin{aligned}
G_{Ta} &= 10^{G_T'/10}, \quad G_{Tb} = 10^{G_T''/10}, \\
G_{Ra} &= 10^{G_R'/10}, \quad G_{Rb} = 10^{G_R''/10}.
\end{aligned} \tag{2}
$$

The radiation matrix for a predominantly linearly polarized wave is written here as

$$\Lambda_T \equiv \begin{pmatrix} F_{Ta} & -if_{Tb}\exp(-i\delta_{Tb}) \\ f_{Ta}\exp(i\delta_{Ta}) & iF_{Tb} \end{pmatrix}, \qquad [3]$$

where δ denotes a phase factor determining the antenna imperfection, i.e., the degree of ellipticity (see Appendix 1). If the transmitted electric field is predominantly either in the $\mathbf{i}_H$ or $\mathbf{i}_V$ (horizontal or vertical) direction, the radiated components are given respectively by

$$\begin{pmatrix} E_{OH} \\ E_{OV} \end{pmatrix} = \Lambda_T \cdot \begin{pmatrix} 1 \\ 0 \end{pmatrix} \quad \text{or} \quad \begin{pmatrix} E_{OH} \\ E_{OV} \end{pmatrix} = \Lambda_T \cdot \begin{pmatrix} 0 \\ 1 \end{pmatrix}. \qquad [4]$$

In frequency reuse system, both predominant component pairs exist. Similarly for reception in two receiver antenna channels, which are predominantly sensitive to linear polarization, the inverse matrix $\Lambda_R{}^{-1}$ has to be used, namely

$$\Lambda_R{}^{-1} \equiv \begin{pmatrix} F_{Ra} & f_{Ra}\exp(-i\delta_{Ra}) \\ if_{Rb}\exp(i\delta_{Rb}) & -iF_{Rb} \end{pmatrix}. \qquad [5]$$

The clear weather isolations are defined as the ratios

$$D_{Ta,b} \equiv 10^{(D_{T'''}/20)} = F_{Ta,b}/f_{Ta,b} \quad \text{and}$$
$$D_{Ra,b} = 10^{(D_{R'''}/20)} = F_{Ra,b}/f_{Ra,b}, \qquad [6]$$

and these depend on the angles ϕ_T and ϕ_R as mentioned above. The radiation matrices for predominantly circular waves are given later.

Fig. 1 also illustrates the angle of incidence, α, and the canting angle, τ. Also shown (in considering noncircularly polarized waves) are the polarization angle, ξ, and the misalignment angle, Ω. Now α is the angle between the incidence direction and the minor axis of the raindrop. If the canting angle is small, the angle of incidence is nearly equal to the angle, ψ, between the incidence direction and the local vertical at the ground station. The angles ψ and ξ are obtainable from the satellite longitude (L_{os}), the earth location (L_{aa},L_{oa}) for the boresight axis ray from the satellite antenna, and the earth station location (L_a,L_o) for latitude and longitude respectively. Let R_E = 6378 km be the earth radius and H = 42187 km be the distance from the synchronous satellite to earth center. To order $(R_E/H)^2$, we have*

$$\tan\xi = \frac{\sin L_{aa}\cos L_a \sin L_d - \cos L_{aa}\sin L_{da}\sin L_a}{\sin L_{aa}\sin L_a + \cos L_{aa}\sin L_{da}\cos L_a \sin L_d}, \qquad [7]$$

where $L_{da} = L_{oa} - L_{os}$ and $L_d = L_o - L_{os}$. Also

* Note the plus sign in the denomenator of Eq. [7], erroneously given as negative in Shkarofsky and Moody.[4]

$$\cos\psi = (H \cos L_a \cos L_d - R_E)/Q, \quad [8]$$

where

$$Q^2 \equiv H^2 + R_E{}^2 - 2HR_E \cos L_a \cos L_d. \quad [9]$$

The polarization angle can be defined more generally than shown in Fig. 1. Consider the vertical plane containing the satellite, the earth center and location P_o or (L_{aa},L_{oa}). Adopt the convention that longitudes are positive eastward of Greenwich and negative westward, and that latitudes are positive above the equator and negative below. Suppose that at point P_o, the electric vector is displaced by an angle K from the counterclockwise normal to the vertical plane. The angle K is positive above and negative below the horizontal normal. Then it can be shown that the polarization angle at point (L_a,L_o) measured from the same normal line is given by $K + \xi$ where ξ is that in Eq. [7]. Suppose on the other hand that the electric vector at point P_o is displaced by an angle K from the vertical plane. Now K is positive counterclockwise and negative clockwise from the vertical plane. Then the polarization angle at (L_a,L_o) measured from the same vertical plane can be shown to be $K - \xi$ where ξ is that in Eq. [7]. Thus ξ is the negative of the expression in Eq. [7] for vertical polarization ($K = 0$) on boresight at point P_o.

The canting angle, τ, and the actual angle of incidence, α, are related to three other angles, namely ψ given above, and θ and ϕ. Here θ is the actual polar angle of the minor axis of the raindrop with respect to the local vertical and ϕ is the azimuthal angle of the raindrop with respect to the horizontal axis in a plane containing the vertical and the incidence direction (see Fang[5]). The relations are

$$\sin\tau = -\sin\theta \sin\phi/\sin\alpha \quad [10]$$

$$\cos\alpha = \cos\theta \cos\psi + \sin\theta \sin\psi \cos\phi. \quad [11]$$

Variations in τ and α are due to variations in θ and ϕ.

The received field after propagation through rain can be written in terms of matrices to be now introduced. We define the canting angle matrix **V** and its inverse as follows:

$$\mathbf{V} \equiv \begin{pmatrix} \cos\tau & \sin\tau \\ -\sin\tau & \cos\tau \end{pmatrix}; \quad \mathbf{V}^{-1} \equiv \begin{pmatrix} \cos\tau & -\sin\tau \\ \sin\tau & \cos\tau \end{pmatrix}. \quad [12]$$

The transformation matrix, **B**, between the forward scattered electromagnetic fields and the incident fields for two waves, incident respectively along the major and minor axes, is given by

$$\mathbf{B} \equiv \begin{pmatrix} \exp[i(k_1 - k_0)r] & 0 \\ 0 & \exp[i(k_2 - k_0)r] \end{pmatrix}. \quad [13]$$

Here r is the path length through the rainfall (assuming the rain effects to be uniform over r), $k_0 = 2\pi/\lambda$ is the free space wavenumber, λ is the wavelength, and

$$k_{1,2} - k_0 \equiv i\alpha_{1,2} + \beta_{1,2}$$
$$= (iA_{1,2}/8.686 + \pi\Phi_{1,2}/180) \times 10^{-3} \quad [14]$$

where $A_{1,2}$ and $\Phi_{1,2}$ are the attenuation per km and phase shift per km, calculated for example by Oguchi and Hosoya[6] as a function of incidence angle, α, and frequency, f. In particular, the differential values are defined as

$$\Delta\alpha = \alpha_1 - \alpha_2, \quad \Delta A = A_1 - A_2, \quad \Delta\beta = \beta_1 - \beta_2$$
$$\text{and} \quad \Delta\Phi = \Phi_1 - \Phi_2. \quad [15]$$

It is also useful to introduce the parameters p and χ used by McCormick and Hendry,[2]

$$pe^{-i\chi} \equiv -\tanh\left[\frac{i}{2}(k_1 - k_2)r\right] \quad [16a]$$

or

$$p^2 \equiv \frac{\cosh(r\Delta\alpha) - \cos(r\Delta\beta)}{\cosh(r\Delta\alpha) + \cos(r\Delta\beta)} \quad \text{and} \quad \tan\chi \equiv \frac{\sin(r\Delta\beta)}{\sinh(r\Delta\alpha)}. \quad [16b]$$

2.2 Received Fields for Linear Polarization

For linearly polarized waves, we need the polarization angle matrices, Ψ_T and Ψ_R, where in Ψ_R we allow for a misalignment angle, Θ, in polarization.

$$\Psi_T \equiv \begin{pmatrix} \cos\xi & \sin\xi \\ -\sin\xi & \cos\xi \end{pmatrix}; \quad \Psi_R \equiv \begin{pmatrix} \cos(\xi + \Theta) & -\sin(\xi + \Theta) \\ \sin(\xi + \Theta) & \cos(\xi + \Theta) \end{pmatrix} \quad [17]$$

With the above introduced matrices, the received electric field components, both for direct and cross polarization (denoted by subscript x), are given by

$$\begin{pmatrix} E_{Ra}/\kappa_a \\ E_{Rbx}/\kappa_a \end{pmatrix}$$
$$= \Lambda_R^{-1} \cdot \Psi_R \cdot \mathbf{V}^{-1} \cdot \mathbf{B} \cdot \mathbf{V} \cdot \Psi_T \cdot \Lambda_T \cdot \begin{pmatrix} 1 \\ 0 \end{pmatrix} \quad [18]$$

if the transmitted wave is predominantly polarized horizontally. If the wave polarization is predominantly vertical, we change $\left(\begin{smallmatrix} E_{Ra} \\ E_{Rbx} \end{smallmatrix}\right)$ to $\left(\begin{smallmatrix} E_{Rax} \\ E_{Rb} \end{smallmatrix}\right)$

and $\binom{1}{0}$ to $\binom{0}{1}$. Corresponding to these two cases, κ is given in magnitude by

$$|\kappa_{a,b}| = \frac{\lambda}{4\pi d} (G_{Ta} G_{Ra,b})^{1/2} \quad \text{and}$$

$$|\kappa_{a,b}| = \frac{\lambda}{4\pi d} (G_{Tb} G_{Ra,b})^{1/2}, \qquad [19]$$

where d is the transmitter to receiver distance. Eq. [18] assumes that all raindrops are oriented at the same or at an effective canting angle, τ. Such an approach has been proposed by Watson and Arbabi[7] and is adopted in our calculations below. Fang and Jih,[8] on the other hand, introduce the canting angle distribution $p(\theta,\phi)$, normalized to $\int\int p(\theta,\phi) \sin\theta d\theta d\phi = 1$, where θ and ϕ are defined above in Eq. [10]. Then Eq. [18] is modified to read

$$\begin{pmatrix} E_{Ra}/\kappa_a \\ E_{Rbx}/\kappa_b \end{pmatrix} = \int_0^{\pi} \int_0^{2\pi} \Lambda_R^{-1} \cdot \Psi_R \cdot \mathbf{V}^{-1} \cdot \mathbf{B} \cdot \mathbf{V} \cdot \Psi_T \cdot \Lambda_T \cdot \begin{pmatrix} 1 \\ 0 \end{pmatrix} p(\theta, \phi) \sin\theta d\theta d\phi. \qquad [20]$$

Multiplication of the matrices and calculation of the magnitudes of the various matrix elements leads to results given in Shkarofsky and Moody[4] (with τ there being replaced by $\tau + \xi$, and θ there referring to the symbol 0 here). Appendix 2 here gives the matrix elements and summarizes the results. The worst phase results (Eqs. [9] to [17] in Shkarofsky and Moody) follow by letting $\delta_{Ta,b} = -\delta_{Ra,b} = \pi/2$. The random phase results (Eqs. [27], [30], [33], and [36] there) follow by letting the δ phases be random. Details can be found in Appendix 2.

2.3 Received Fields for Circular Polarization

The analysis for predominantly polarized circular waves can similarly be formulated. We use the same symbols F and f, but F here refers to the main (say right-hand) antenna pattern of a *circularly* polarized wave and f refers to the small cross-polarized (i.e. left-hand) component. These should not be confused with the antenna patterns for predominantly *linearly* polarized waves. (All F and f symbols in Appendix 1 here refer to the linear polarization patterns; all F and f in Shkarofsky and Moody[4] when referring to circular waves are meant to be the circular polarization patterns.) The ellipticity e and the angle μ are defined such that e is the ratio of the major to minor axis of the ellipse (see Fig. 22 in Appendix 1) and

$$e \equiv \cot\mu = \frac{F+f}{F-f} \quad \text{or} \quad \frac{F}{f} = \frac{e+1}{e-1} = \tan\left(\mu + \frac{\pi}{4}\right). \tag{21}$$

This relation applies with subscripts Ta, Tb, Ra, and Rb, adopting here the convention that $e > 0$. In dB, we can define F_T', F_T'', f_T'', f_T', F_R', F_R'', f_R', and f_R'' for circular waves using the relations in Eq. [1], and in addition e_T', e_T'', e_R', and e_R'' in dB by

$$\begin{aligned} e_{Ta} &= 10^{e_T'/20}, \quad e_{Tb} = 10^{e_T''/20}, \\ e_{Ra} &= 10^{e_R'/20} \quad \text{and} \quad e_{Rb} = 10^{e_R''/20}. \end{aligned} \tag{22}$$

For perfectly circularly polarized waves, $e' = e'' = 0$, $e = 1$, $(F/f)_{circular} = \infty$ but $(F/f)_{linear} = 1$.

The right-hand and left-hand rotating circularly polarized electric field components can be written with σ phase factors as

$$\begin{aligned} &E_{cr} = Cm, \quad E_{cl} = Cn^*, \quad m = \sin\left(\mu + \frac{\pi}{4}\right) e^{-i\sigma}, \\ &n = \cos\left(\mu + \frac{\pi}{4}\right) e^{-i\sigma}, \end{aligned} \tag{23}$$

with

$$\begin{aligned} &F = |C||m|, \quad f = |C||n|, \quad F/f = \tan\left(\mu + \frac{\pi}{4}\right) \\ &\text{and} \quad |C|^2 = F^2 + f^2. \end{aligned} \tag{24}$$

Instead of the $\mathbf{\Lambda_T}$ and $\mathbf{\Lambda_R}^{-1}$ matrices in Eqs. [3] and [5], it can be shown using the results in Appendix 1 that these are replaced by

$$\mathbf{\Lambda_T} = C_T \mathbf{R} \cdot \mathbf{M_T} \quad \text{and} \quad \mathbf{\Lambda_R}^{-1} = C_R^* \mathbf{M_R}^{-1} \cdot \mathbf{R}^{-1} \tag{25}$$

where $\mathbf{R}$ is the rotation matrix

$$\mathbf{R} \equiv \frac{1}{\sqrt{2}} \begin{pmatrix} 1 & 1 \\ i & -i \end{pmatrix}, \quad \mathbf{R}^{-1} \equiv \frac{1}{\sqrt{2}} \begin{pmatrix} 1 & -i \\ 1 & i \end{pmatrix} \tag{26}$$

and

$$\mathbf{M}_T \equiv \begin{pmatrix} m_{Ta} & n_{Tb} \\ n_{Ta}^* & -m_{Tb}^* \end{pmatrix}, \quad \mathbf{M_R}^{-1} \equiv \begin{pmatrix} m_{Ra}^* & n_{Ra} \\ n_{Rb}^* & -m_{Rb} \end{pmatrix}. \tag{27}$$

We also note that the matrices for misalignment or polarization angle, Ψ_R and Ψ_T, may be omitted for relatively small depolarizations. Consequently, instead of Eq. [18], we now have

$$\begin{pmatrix} E_{Ra}/\kappa_a C_T C_{Ra}^* \\ E_{Rbx}/\kappa_b C_T C_{Rb}^* \end{pmatrix}$$

$$= \mathbf{M_R}^{-1} \cdot \mathbf{R}^{-1} \cdot \mathbf{V}^{-1} \cdot \mathbf{B} \cdot \mathbf{V} \cdot \mathbf{R} \cdot \mathbf{M_T} \cdot \begin{pmatrix} 1 \\ 0 \end{pmatrix} \qquad [28]$$

if a predominantly right-hand circular wave is transmitted. If the wave is predominantly left-hand circular, we change $\binom{E_{Ra}}{E_{Rbx}}$ to $\binom{E_{Rax}}{E_{Rb}}$ and $\binom{1}{0}$ to $\binom{0}{1}$. If we wish to include the canting angle distribution, Eq. [28] can be averaged over this distribution as in Eq. [20] for linear waves.

The procedure is to multiply the matrices in Eq. [28] and calculate the magnitudes of the various matrix elements. These are given in Appendix 2, where the results are also summarized. Relations for the worst relative phases are obtained by letting $\sigma_{Ta,b} = 0$ and $\sigma_{Ra,b} = \pi/2$ so that the axes of the received elliptical field are orthogonal to the axes of the transmitted field. This gives the relations in Eqs. [21] to [24] in Shkarofsky and Moody.[4] Results for random phases between transmitter and receiver signals are obtained by letting the σ phases be random. This leads to the results given in Eqs. [29], [32], [34], and [37] in Shkarofsky and Moody, which turn out to be independent of τ and the same for right-hand and left-hand circular polarizations.

2.4 Parameters of Interest

Results will be illustrated based on the random phase limit both for predominantly linear and circular waves. Three sets of parameters are of interest, namely $(\mathrm{XPD})_{\mathrm{H,V,C}}$, $(\mathrm{XPI})_{\mathrm{H,V,C}}$, and $(\mathrm{ATT})_{\mathrm{H,V,C}}$, all in dB. The quantities XPD refer to the discrimination between the two cross-polarized channels of signals received when a single dominantly polarized wave (either linear horizontal, linear vertical, or circular) is transmitted. These relations are obtained by taking ratios of the 11 to 12 matrix elements or of the 22 to 21 matrix elements and expressing the results in dB. The quantities XPI refer to the isolation against cross-talk in a single receiver channel when two cross-polarized signals are transmitted. These relations result from the ratios of the 11 to 21 or 22 to 12 matrix elements. The quantities ATT are the attenuations of the wave with respect to those in free space for various polarizations. Formulas for XPD are given in Eqs. [36] to [37] and for XPI in Eqs. [33] and [34] in Shkarofsky and Moody.[4] The same analysis gives ATT. Expressions are also given here in Appendix 2 for all three sets of quantities.

3. Calculated Results

Antennas transmitting or receiving a particular polarizations in clear weather are designed to have the cross-polarized antenna pattern as low as possible, viz. $f \ll F$ in our previous notation. For usual satellite antennas, the clear weather isolation, CWI, i.e., the difference between the co-polar and cross-polar patterns in dB, varies from about 35 to 45 on axis to about 20 at the off-axis angle equal to the total beam width. Well

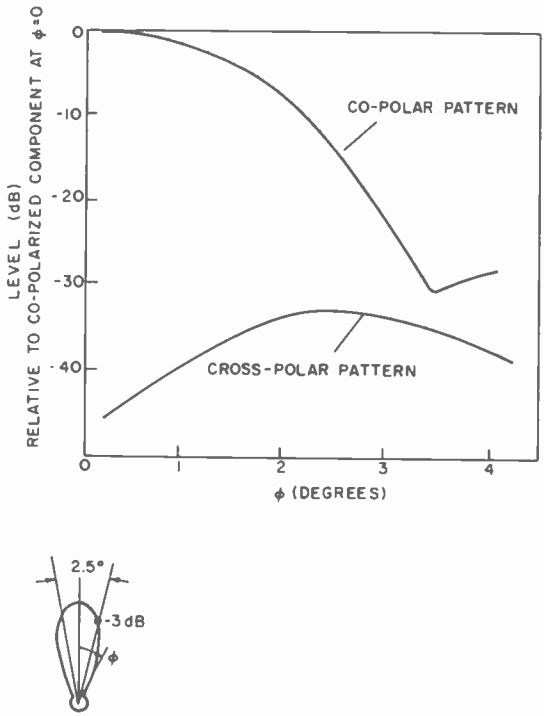

Fig. 2—Cross-polarized component of the OTS spotbeam antenna at 11.58 GHz (linear polarization) (after EBU Report[9]).

designed antennas have a sharp on-axis minimum in the cross-polarization pattern. The cross-polarized pattern reaches a maximum at an angle equal to about the beamwidth. Fig. 2 shows[9] the two patterns of the spot beam antenna to be used on the European Orbital Test Satellite (OTS) operating at 11.58 GHz. The CWI values are thus functions of the off-axis angle ϕ_T. In earth paths, the transmitter and receiver usually face each other, but the satellite transmitter does not usually face the earth receiver and therefore the off-axis patterns are of importance. The

OTS antenna is of modern design but even better ones can be designed with a lower cross-component at all off-axis angles.

Although ground stations for community reception usually have good isolation, small individual receivers are worse. Their CWI values vary from about 25 dB on-axis to about 10 dB at an off-axis angle equal to the beamwidth. The off-axis patterns of ground receivers are of consequence both if there occurs a pointing error towards the desired satellite and also if neighbouring interfering satellites are present and their interference levels have to be minimized. Clearly, accurate pointing and accurate alignment of the polarization vectors for linear waves, especially if both polarizations are used, are necessary for ground receivers. Proper satellite attitude control and station keeping are also required to provide a constant polarization angle as seen by the receiver in clear weather. Otherwise, the receiver may require polarization and position tracking. For dual polarized satellite antennas, tracking is a necessity and the theory on this is elaborated by Johannsen.[10]

Attempts should be made to increase the antenna CWI on-axis values over and above 40 dB. Otherwise, the cross-polar component may vary during precipitation both above or below the clear weather reference, as theoretical calculations below show.

For the calculations, we adopt several approximations, namely an effective canting plus polarization angle to be specified in the graphs, a uniform rainfall rate along the path length, and the results based on random phases between orthogonal electric field components. The effective path length through the rain is determined from the following empirical formulas due to M. K. Lee (private communication):

$$H(\text{km}) = 5.34 - 1.67 \log_{10} R$$
$$V(\text{km}) = 17.18 - 5.13 \log_{10} R \qquad [29a]$$

where H is the horizontal extent and V is the vertical extent of the rainfall, and R in mm/hr is the rainfall rate, assuming $R > 1$. Then the effective path length r is given by whichever one of the following two expressions is less than $\sqrt{H^2 + V^2}$:

$$r(\text{km}) = H/\sin\alpha \quad \text{or} \quad r(\text{km}) = V/\cos\alpha \qquad [29b]$$

where α is the incidence angle. Another empirical formula will also be used for comparison towards the end of this section.

In our calculations, we simulate various transmitter or receiver on-axis CWI values (D_T' and D_R' respectively), or their variable off-axis values, by allowing D_T' and D_R' to range over a series of values. The values used are D_T' = 25, 35, and 45 dB and D_R' = 20, 25, 30, 35, and 45 dB. For circularly polarized waves, the corresponding ellipticity values are e_T' = 0.978, 0.309, and 0.0977 dB and e_R' = 1.74, 0.978, 0.550, 0.309, and

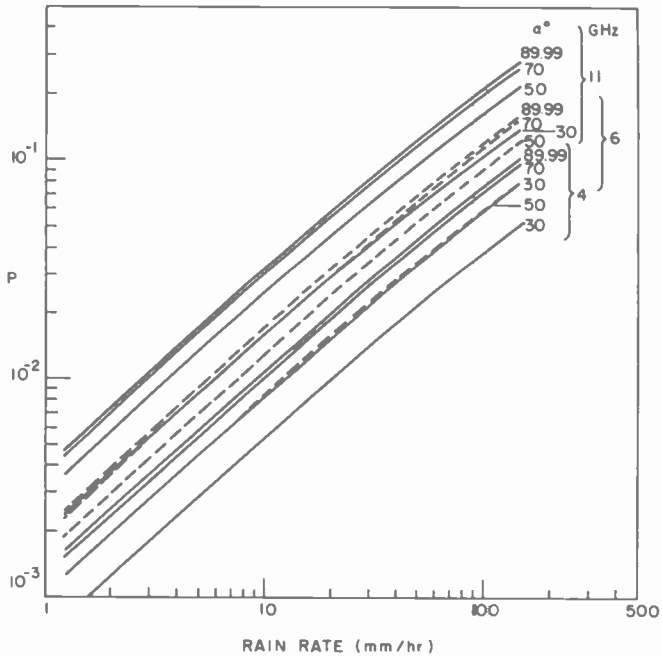

Fig. 3—The parameter p plotted versus rain rate for various frequencies and α in degrees.

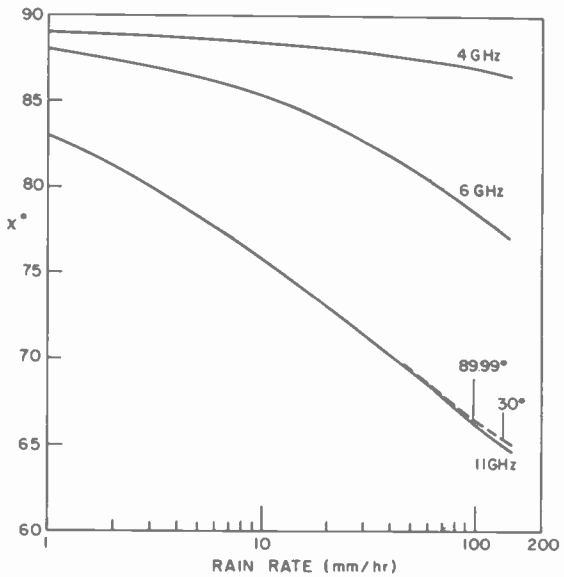

Fig. 4—The parameter χ plotted versus rain rate for various frequencies and α in degrees.

0.0977 dB. A misalignment of the receiver polarization direction for linear waves is allowed for by letting Θ vary over $-8°$ to $8°$. We also note that for linearly polarized waves, the polarization angle, ξ, can change and off-axis signals in the east-west direction are received with a polarization angle differing from that at beam center (see Eq. [7]). This is included in the calculations by letting $\tau + \xi$ vary from 0 to 45° and sample calculations for $\Theta = 0°$ will be shown.

The values of p and χ have been calculated by us based on the results[6] for ΔA and $\Delta\Phi$ from Eqs. [16b] versus R, the rainfall rate, for three frequencies 4, 6, and 11 GHz, and various angles of incidence α or elevation angles $90° - \alpha$, with $\alpha = 89.99°, 70°, 50°$, and $30°$. These results are shown in Figs. 3 and 4. Fig. 4 shows that χ is quite insensitive to the

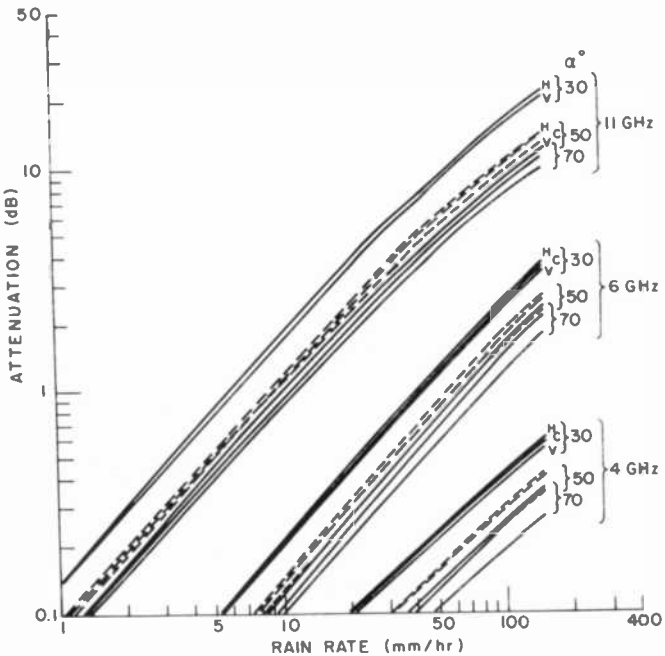

Fig. 5—Attenuation along a satellite-to-earth path versus rain rate for various frequencies and α in degrees.

value of α for our range of parameters. The equations for these results are independent of τ. On the other hand, the relative attenuation, with respect to its clear weather value, depends on τ and on the type of polarization. It has a very slight dependence on the misalignment angle and on the antenna clear weather discrimination or ellipticity values. Assuming perfect antennas ($D = \infty$) and exact alignment ($\Theta = 0$), we plot

in Fig. 5 this relative attenuation versus rainfall rate for horizontal, circular, and vertical polarizations. The results show that the attenuation decreases in that order. Plots are given for three frequencies and various α values, assuming $\tau = 4°$ and $\xi = 0$. The attenuation increases with elevation angle (or decreasing α) due to the larger propagation distance through the rainfall extent as given by Eq. [29]. This more than compensates for the lower values of p. Note that other empirical expressions (see Fang[11] and also Eq. [30] later on) for path length can lead to an opposite theoretical trend, namely attenuation decreasing with elevation angle.

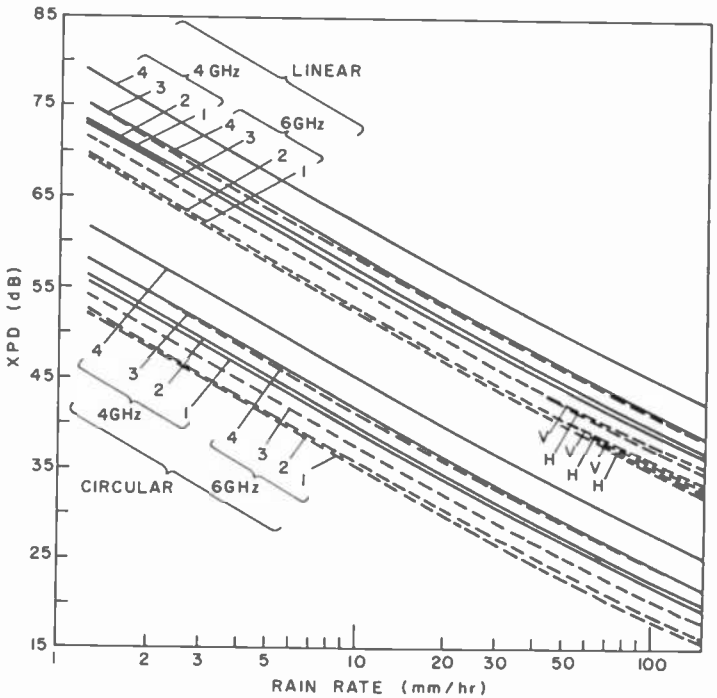

Fig. 6—XPD versus rain rate at 4 and 6 GHz for perfect antennas ($D_R = D_T = \infty$), exact alignment ($\Theta = 0$) and $\tau = 4°$. The top curves are for *H* or *V* polarization unless indicated and the bottom curves are for circular polarization; solid lines for 4 GHz, dashed for 6 GHz; curve 1 is for $\alpha = 89.99°$, 2 for 70°, 3 for 50°, and 4 for 30°.

In Fig. 6 we plot values of XPD versus rainfall rate for 4 and 6 GHz (where the attenuation is small) and in Fig. 7 versus attenuation for 11 GHz, given perfect antennas and exact alignment. Adopting as before $\tau = 4°$, plots are given for three frequencies and various α values for linear horizontal and vertical polarizations. Sets of results for circular polarization are also shown. The differences between horizontal and vertical

polarizations are negligible at 4 GHz, just noticeable at 6 GHz for large rain rates, and distinguishable at 11 GHz. It is interesting to note from Fig. 7 that for a given attenuation of fade, vertical polarization provides a better XPD only for the large fades but not for the smaller fades.

Calculations are now performed including antenna effects using the data on p, χ and attenuation plotted in Figs. 3, 4, and 5. Selected sample results are plotted below, all for $\alpha = 70°$. This is a worst case corresponding to a location such as Mill Village, N.S., in the north for a satellite positioned at 114°W longitude. As seen from Figs. 6 and 7, results

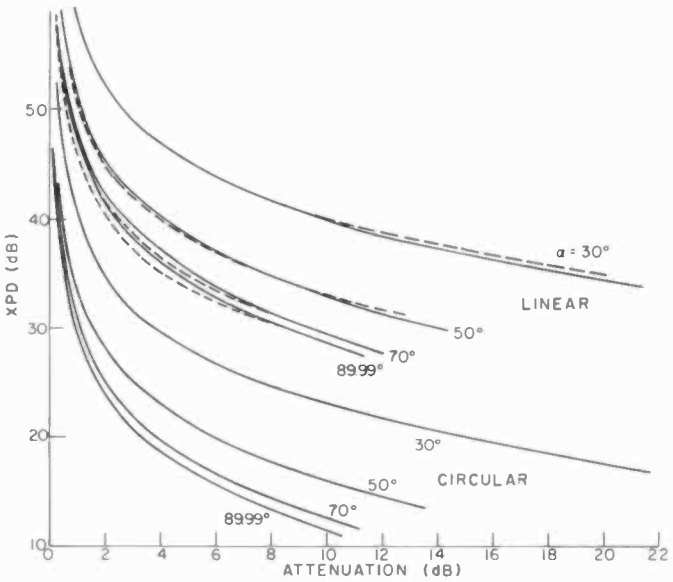

Fig. 7—XPD versus attenuation at 11 GHz for perfect antennas ($D_R = D_T = \infty$), exact alignment ($\Theta = 0$) and $\tau = 4°$. In top curves, solid lines are for *H* polarization, dashed for *V* polarization; bottom curves are for circular polarization.

for $\alpha = 70°$ are close to those for 89.99° and XPD and XPI for both of these are lower than for other α values. In certain examples, we select only a few D_R' and D_T' combinations, or we plot only $XPD_{H,V}$ omitting $XPI_{H,V}$, or we look at only specific rain rates. The object is to show the trends for each situation.

Fig. 8 illustrates the effect of the misalignment angle Θ between the receiver polarization direction and that of the incoming electric field direction for linear polarization. XPD values, all referring to XPD_H except for one curve, are plotted versus the angle Θ varying from $-8°$ to 8°. Curve 1 represents the situation for perfect antennas and the others are for various combinations of D_T' and D_R'. We take $\tau + \xi = 4°$.

The dashed plots are for two frequencies, 4 and 11 GHz, and two rain rates, 50 and 150 mm/hr. The solid curves represent the case of no rain. The arrows indicate the values of XPD for perfect antennas and exact alignment in the presence of rain. The figure illustrates the stringent conditions required to observe XPD effects subject to rain alone. First,

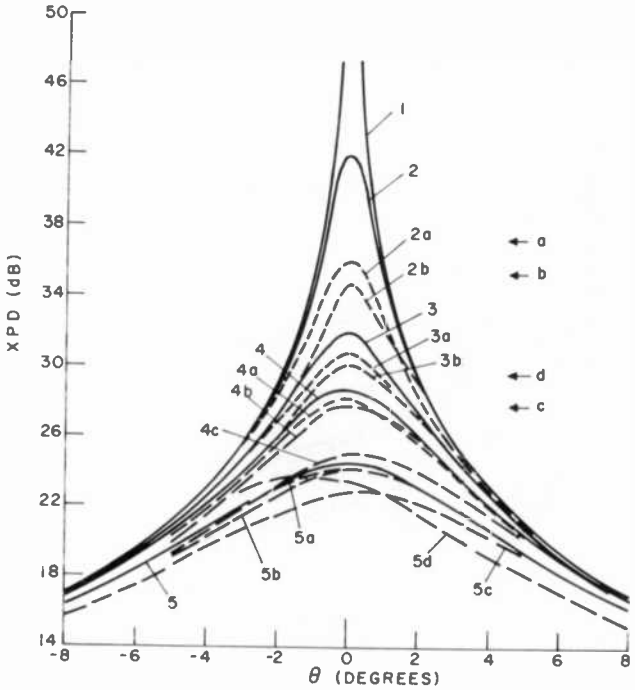

Fig. 8—XPD versus misalignment angle θ for $\alpha = 70°$ and $\tau + \xi = 4°$. Arrows indicate limits for $D_R' = D_T' = \infty$ and $\theta = 0$. Curves are as follows:

(1) $D_R' = D_T' = \infty$
(2) $D_R' = D_T' = 45$ dB
(3) $D_R' = D_T' = 35$ dB
(4) $D_R' = 30$; $D_T' = 35$ dB
(5) $D_R' = 25$; $D_T' = 35$ dB

(a) XPD_H, 4 GHz, 150 mm/hr
(b) XPD_H, 11 GHz, 50 mm/hr
(c) XPD_H, 11 GHz, 150 mm/hr
(d) XPD_V, 11 GHz, 150 mm/hr

the solid curves have to be close to curve 1, with D_R' and D_T' about 45 dB, and secondly, the angle θ has to be close to zero, below 2°. At $\theta = 3°$, even for $D_R' = D_T' = 45$ dB, the XPD value is sufficiently below its maximum at $\theta = 0°$ to disguise rain effects. For the lower D_R' and D_T' combinations, the rain effects have only a moderate influence because the imperfections in the antennas dominate, and then the θ misalignment effects also cause a smaller variation. Thus, rain effects may be

disguised either by misalignment for near perfect antennas or by the poor isolation of imperfect antennas.

Asymmetry with respect to $\pm\Theta$ shows up for the higher frequency of 11 GHz. Curves 5(c) and 5(d) plot XPD_H and XPD_V respectively and we see that these two curves cross at $\Theta = 1°$. Consequently, in this case,

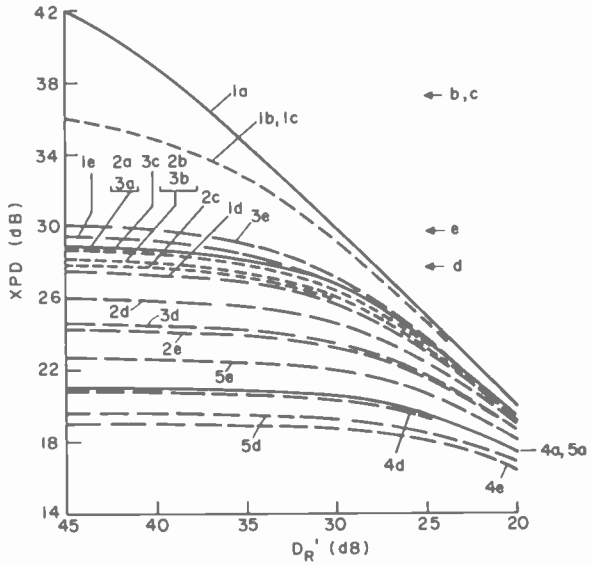

Fig. 9—XPD versus D_R' or pointing error for $\alpha = 70°$, $\tau + \xi = 4°$ and $D_T' = 45$ dB. Arrows indicate limits for $\Theta = 0$ and $D_R' = D_T' = \infty$. Curves are as follows:

(1) $\Theta = 0$	(a) no rain
(2) $\Theta = 2°$	(b) XPD_H, 4 GHz, 150 mm/hr
(3) $\Theta = -2°$	(c) XPD_V, 4 GHz, 150 mm/hr
(4) $\Theta = 5°$	(d) XPD_H, 11 GHz, 150 mm/hr
(5) $\Theta = -5°$	(e) XPD_V, 11 GHz, 150 mm/hr

$XPD_H > XPD_V$ for $\Theta > 1°$ and vice versa for $\Theta < 1°$. Thus with imperfect antennas and misalignment, vertical polarization is not always better than horizontal.

Figs. 9 and 10 represent for both linear and circular polarizations, respectively, the effects of decreasing the isolation of the receiver for a given value of transmitter isolation. This variation of D_R' or e_R' also simulates a variable off-axis angle or pointing error of the receiver, neglecting the changes in the polarization angle ξ that also occur when this is done for linear polarization.

In Fig. 9, a value of $D_T' = 45$ dB is assumed with D_R' varying from 45 to 20 dB, and $\tau + \xi$ is fixed at 4°. The solid curves are for a no-rain sit-

uation and the dashed curves represent XPD_H and XPD_V results for a rain rate of 150 mm/hr and at 4 and 11 GHz. Results are given for misalignment angles $\Theta = 0, \pm 2°$ and $\pm 5°$. The extreme curves are well separated at $D_R' = 45$ dB, but all curves become clustered together at $D_R' = 20$ dB, where this finite receiver isolation dominates over rain and over

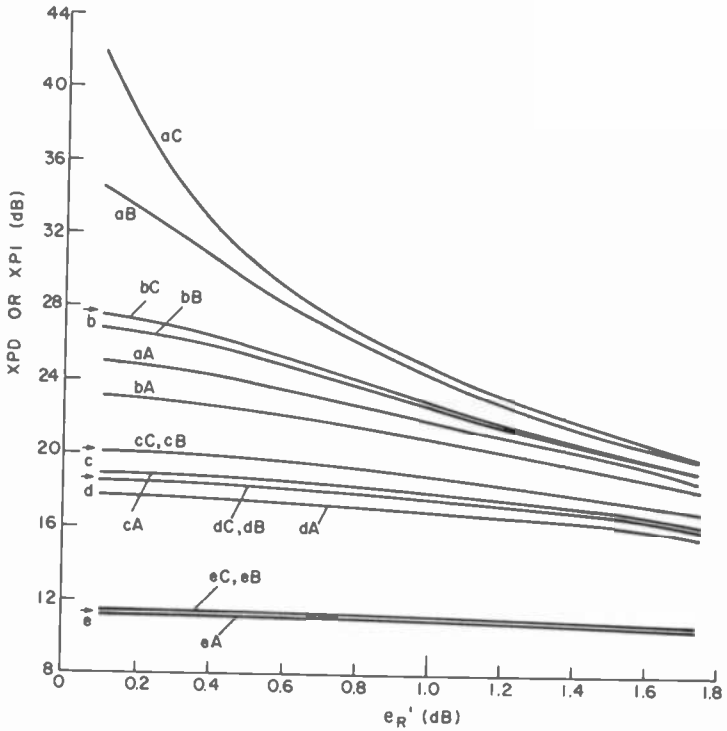

Fig. 10—XPD or XPI versus e_R' or pointing error for circular polarization and $\alpha = 70°$. Arrows indicate limits for $e_T' = e_R' = 0$. Curves are as follows

(A) $e_T' = 0.978$ dB or $D_T' = 25$ dB (a) no rain (d) 11 GHz, 50 mm/hr
(B) $e_T' = 0.309$ dB or $D_T' = 35$ dB (b) 4 GHz, 50 mm/hr (e) 11 GHz, 150 mm/hr
(C) $e_T' = 0.098$ dB or $D_T' = 45$ dB (c) 4 GHz, 150 mm/hr

misalignment effects. At 4 GHz, the $\pm\Theta$ and the $XPD_{H,V}$ curves are close together, but at 11 GHz, these four curves separate as can be seen from curves 2(d), 2(e), 3(d), 3(e) or from 4(d), 4(e), 5(d), 5(e). At $\Theta = 2°$ or 5°, $XPD_H > XPD_V$; whereas at $\Theta = 0, -2°$, or $-5°$, we find that $XPD_V > XPD_H$, in agreement with Fig. 8. It is interesting to note that the curves are more or less flat from $D_R' = 45$ dB to 35 dB for finite Θ showing that either the Θ effect dominates over D_R' in this region, or rain dominates, as for the situation in curves 1(e) and 1(d) (see arrows in Fig. 9).

In Fig. 10, corresponding results are shown for circular polarization. Here, three values of ellipticity, $e_T' = 0.978$, 0.309, and 0.098 dB, corresponding to $D_T' = 25$, 35, and 45 dB are assumed. Also, e_R' is variable over the 0.1 to 1.74 dB range, equivalent to $D_R' = 45$ to 20 dB. In the random phase limit used here, the misalignment angle and the canting

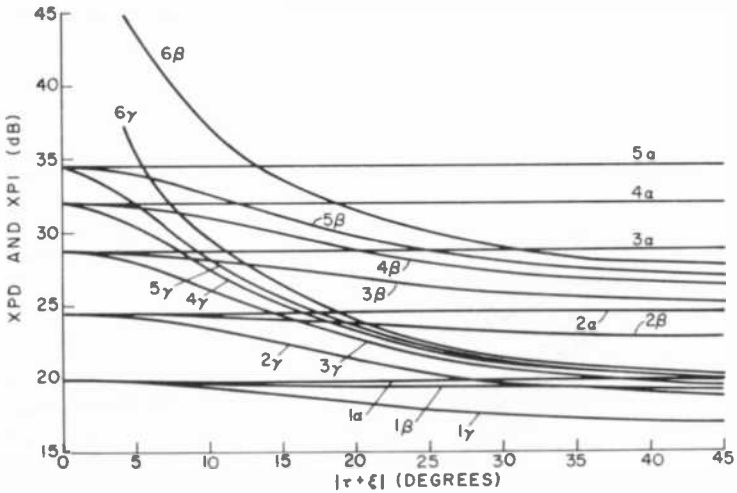

Fig. 11—XPD or XPI versus canting plus polarization angle for $\alpha = 70°$, $\Theta = 0$, and at 4 GHz, (Note: $XPD_H \approx XPD_V \approx XPI_H \approx XPI_V$.) The curves are as follows:

(α) no rain
(β) 50 mm/hr
(γ) 150 mm/hr
(1) $D_R' = 20$; $D_T' = 35$ dB
(2) $D_R' = 25$; $D_T' = 35$ dB
(3) $D_R' = 30$; $D_T' = 35$ dB
(4) $D_R' = 35$; $D_T' = 35$ dB
(5) $D_R' = 45$; $D_T' = 35$ dB
or $D_R' = 35$; $D_T' = 45$ dB
(6) $D_R' = D_T' = \infty$

angle τ are irrelevant and, in addition $XPD_r = XPD_l = XPI_r = XPI_l$. Hence, on the same graph, we can illustrate more cases, namely, three e_T' values and two rain rates of 50 and 150 mm/hr. Whenever the curves cluster together for the three e_T' values and are flat versus e_R', then rain effects dominate. We see that this occurs for the lower XPD cases, namely curves (d) and (e) at 11 GHz and curve (c) at 4 GHz and 150 mm/hr. Thus, rain can dominate over finite antenna isolation for circular polarization because rain is then sufficiently severe to lower the net isolation to below those of the antennas in clear weather. The values of e_R' determine the net XPD magnitudes only for low rain rates.

Figs. 11 and 12, for 4 and 11 GHz, respectively, illustrate the variations in XPD or XPI for linear polarization as the sum of the canting plus polarization angle, $\tau + \xi$, varies from 0° to 45°, assuming $\Theta = 0°$. Since at 4 GHz, the values of $XPD_{H,V}$ and $XPI_{H,V}$ are all nearly equal, we can illustrate more combinations of D_R' and D_T' values in Fig. 11 than we

can in Fig. 12 at 11 GHz. Values at $\tau + \xi = 45°$ are equivalent to those for circular polarization. The flat horizontal lines are the net isolation values of the antennas in clear weather. The curves labelled (6β) and (6γ) are for perfect antennas subject to rainfall rates of 50 and 150 mm/hr, respectively. The other curves include finite antenna isolation effects and are subject to either of the two rainfall rates. We see that in most cases (except for curves 1 in Fig. 11), rain starts to dominate the results

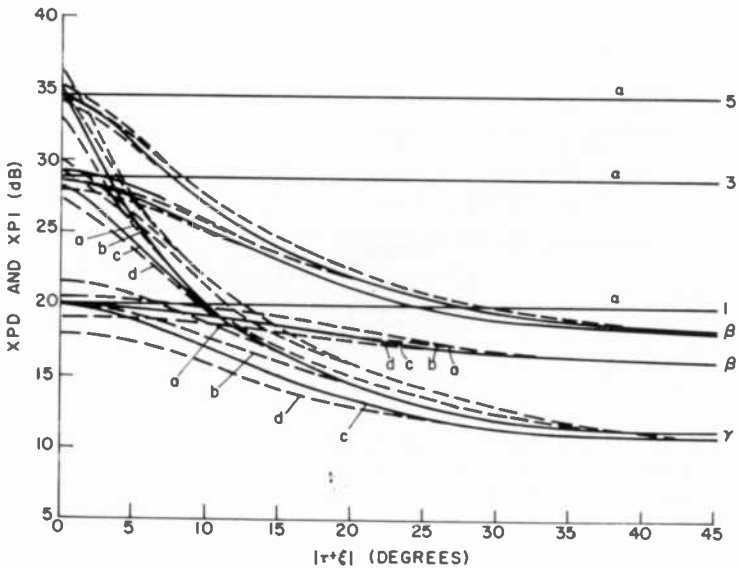

Fig. 12—XPD and XPI versus canting plus polarization angle for $\alpha = 70°$, $\Theta = 0$, and at 11 GHz. The order of the four curves are (a) XPI_V, (b) XPD_V, (c) XPD_H, and (d) XPI_H:

(α) no rain
(β) 50 mm/hr
(γ) 150 mm/hr

(1) $D_R' = 20$; $D_T' = 35$ dB
(3) $D_R' = 30$; $D_T' = 35$ dB
(5) $D_R' = 35$; $D_T' = 45$ dB

close to $\tau + \xi = 45°$, whereas finite antenna isolation effects dominate close to $\tau + \xi = 0°$. Even the XPD values at $\tau + \xi = 20°$ for linear polarization are better, sometimes appreciably, than those at $\tau + \xi = 45°$ or circular polarization. Consequently, linear polarization is preferable to circular even for a 20° polarization angle at an earth receiver in an off-axis direction, provided the misalignment angle θ is close to zero.

In Fig. 12, fewer combination of D_R' and D_T' are used, but each curve separates in certain regions into four curves. We find that $XPI_V > XPD_V > XPD_H > XPI_H$ if $D_T' > D_R'$. The ordinate values always increase in this order for a given rainfall rate at $\Theta = 0$. They all come together to a

single curve near the abscissa value of $\tau + \xi = 45°$. Rain effects are more severe here for 11 GHz than for 4 GHz. Calculations for different combinations of D_R' and D_T' cluster together near $\tau + \xi = 45°$, but they separate and approach their net clear-weather isolation values at $\tau + \xi = 0°$.

Figs. 13 to 18 plot XPD or XPI versus rain rate if the frequency is 4 GHz and versus attenuation if the frequency is 11 GHz. In all graphs,

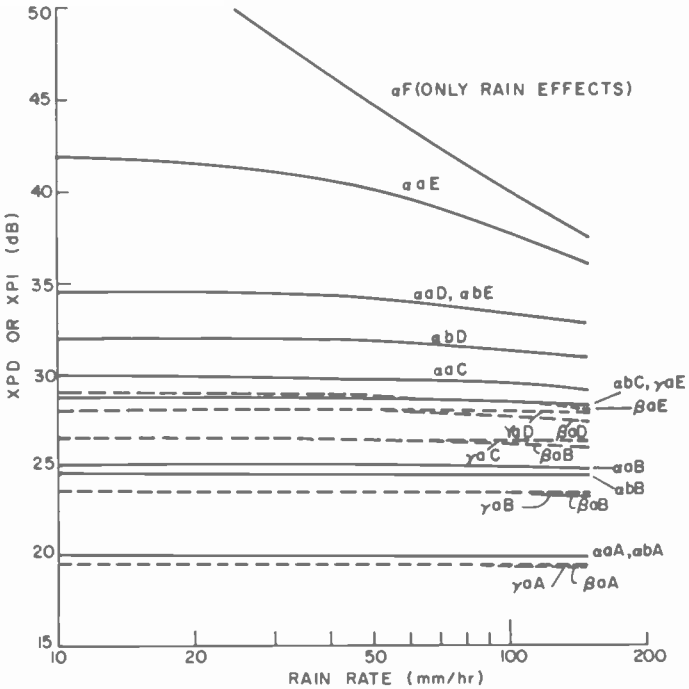

Fig. 13—XPD or XPI versus rain rate for $\alpha = 70°$, $\tau + \xi = 4°$, and at 4 GHz. Here, $XPD_H \approx XPD_V \approx XPI_H \approx XPI_V$, and

(α) $() = 0$
(β) $() = 2°$
(γ) $() = -2°$
(a) $D_T' = 45$ dB
(b) $D_T' = 35$ dB
(A) $D_R' = 20$ dB
(B) $D_R' = 25$ dB
(C) $D_R' = 30$ dB
(D) $D_R' = 35$ dB
(E) $D_R' = 45$ dB
(F) $D_R' = D_T' = \infty$

$\tau + \xi = 4°$ for linear polarization. The main purpose of these graphs is to illustrate the effects of antenna clear weather isolation in limiting the observation of rain-induced effects. As before, a satellite-to-earth link is considered at an elevation angle of 20°.

In Fig. 13, curves are calculated for 4 GHz and linear polarization. The curve marked (αF) is the calculated isolation in the presence of rain for

perfect antennas, and it approaches infinity for a zero rainfall rate. Otherwise, as the rain rate goes to zero, the curves approach their isolation values in clear weather according to the chosen values of D_T' and D_R'. Even for the best chosen values of $D_T' = D_R' = 45$ dB, comparison with theory which includes rain effects alone cannot start until the rain exceeds 100 mm/hr. Most of the other curves are flat and show only a

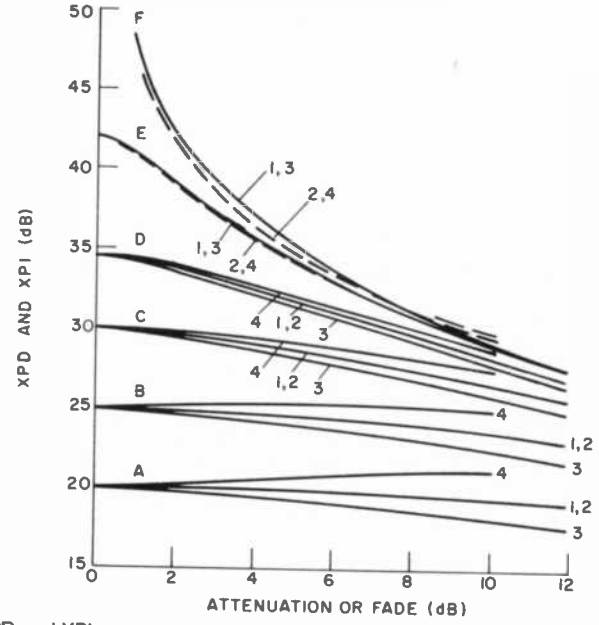

Fig. 14—XPD and XPI versus attenuation for $\alpha = 70°$, $\tau + \xi = 4°$, $\Theta = 0°$, $D_T' = 45$ dB, and at 11 GHz:

(1) XPD_H
(2) XPD_V
(3) XPI_H
(4) XPI_V

(A) $D_R' = 20$ dB
(B) $D_R' = 25$ dB
(C) $D_R' = 30$ dB
(D) $D_R' = 35$ dB
(E) $D_R' = 45$ dB
(F) $D_R' = D_T' = \infty$

slight variation with rain rate. At high rain rates, there is also a minute asymmetry with respect to $\pm\Theta$ misalignment, with the $\Theta = -2°$ providing slightly better XPD or XPI.

Corresponding results are shown in Figs. 14 to 16 for 11 GHz and linear polarization. We give curves for $\Theta = 0°$ and $D_T' = 45$ dB in Fig. 14, for $\Theta = 0°$ and $D_T' = 35$ dB in Fig. 15, and for $\Theta = \mp 2°$ and $D_T' = 45$ dB in Fig. 16a,b. Here the curves separate into those of $XPD_{H,V}$ and $XPI_{H,V}$. The attenuation value on the abscissa corresponds to the individual H or V polarization. In Figs. 14 and 15 we note that only curves D and E ($D_R' \geq 35$ dB, $D_T' \geq 35$ dB) approach at high fades curve F, determined

by rain alone. Comparisons with rain theory which excludes antenna effects can start, say, for curves D at fades above 8 dB or when XPD has decreased to below 30 dB. As already noted in Fig. 7, at low attenuation values for a given fade, Fig. 14 shows that H is better than V polarization and vice versa for the higher attenuation values, provided the values of D_R' and D_T' are sufficiently high (e.g., as in curve E). Fig. 15 for $\Theta = 0$

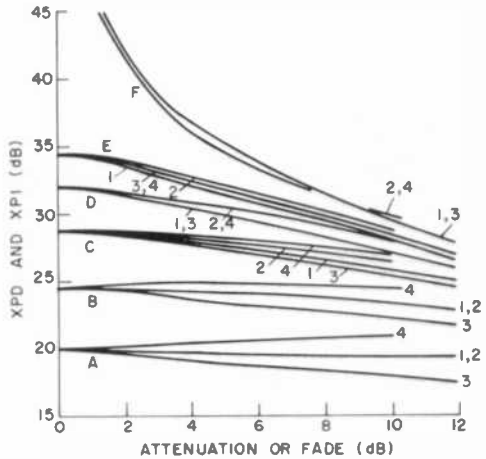

Fig. 15—XPD and XPI versus attenuation for $\alpha = 70°$, $\tau + \xi = 4°$, $\Theta = 0$, $D_T' = 35$ dB, and at 11 GHz:

(1) XPD_H
(2) XPD_V
(3) XPI_H
(4) XPI_V

(A) $D_R' = 20$ dB
(B) $D_R' = 25$ dB
(C) $D_R' = 30$ dB
(D) $D_R' = 35$ dB
(E) $D_R' = 45$ dB
(F) $D_R' = D_T' = \infty$

yields $XPD_V > XPI_V > XPI_H > XPD_H$ when $D_R' > D_T'$ and $XPI_V > XPD_V > XPD_H > XPI_H$ when $D_T' > D_R'$. On the other hand, Figs. 16a,b show for $\Theta = \mp 2°$ that the order can change, with examples of $XPI_V > XPD_H > XPD_V > XPI_H$, $XPD_V > XPI_H > XPI_V > XPD_H$, and $XPD_V > XPI_V > XPI_H > XPD_H$ shown. It is interesting to note that the values in some curves in the presence of rain increase above their clear weather isolation.

Figs. 17 and 18 provides results for circular polarization at 4 and 11 GHz, respectively. Now, even in the 4-GHz case and for D_R' as low as 25 dB, the effect of rain becomes significant and comparisons with rain theory can be made. At 11 GHz, situations with D_R' values as low as 20 dB are affected sufficiently for fades above 5 dB where the XPD and XPI values has decreased to below 17 dB. In all cases, for low rain rates, the curves deviate from curve F and approach their limits based on their D_T' and D_R' values.

Fig. 19 compares results based on the assumed path length, Eq. [29], with another formula, postulated by Ippolito[12], namely

$$r(\text{km}) = 67.57R^{-0.79} \sin 42°/\sin(90 - \alpha) \qquad [30]$$

where $90 - \alpha$ is the elevation angle. XPD and XPI results are plotted versus attenuation for $\alpha = 50°$. Generally the trends are the same for the two r formulas, although some deviations occur for low attenuations and

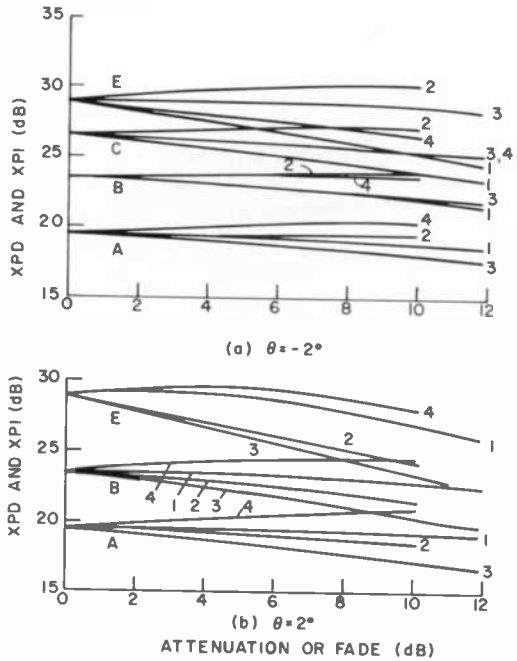

Fig. 16—XPD and XPI versus attenuation for $\alpha = 70°$, $\tau + \xi = 4°$, $D_T' = 45$ dB, and at 11 GHz. For the curves, (a) $\theta = -2°$, (b) $\theta = 2°$, (1) XPD_H, (2) XPD_V, (3) XPI_H, (4) XPI_V, and

(A) $D_R' = 20$ dB
(B) $D_R' = 25$ dB
(C) $D_R' = 30$ dB
(D) $D_R' = 45$ dB

high D_R' values. We can also compare with other formulas, such as Fang's,[11] but this will not be done here.

The general conclusion that we draw is that the finite isolation values in clear weather have to be included in the theory as well as rain effects for any proper comparison between theory and experiment, unless special precautions are taken to raise the clear weather isolation values. Also, one has to distinguish between XPD_H, XPD_V, XPI_H, and XPI_V at 11 GHz but not at 4 GHz. Finally, proper alignment is important for linear polarization.

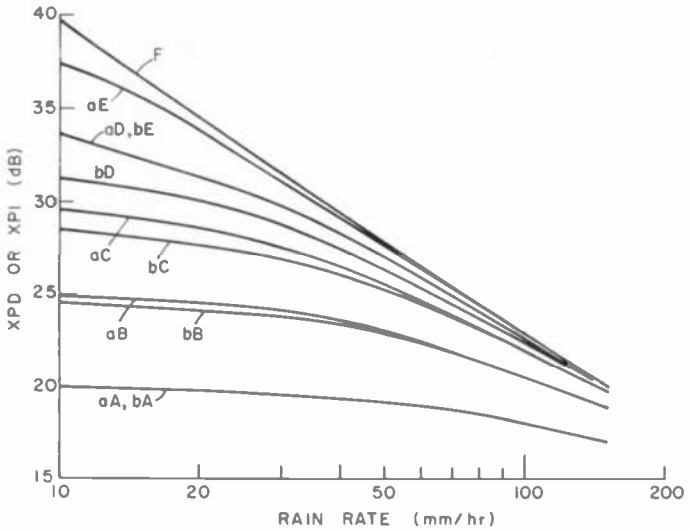

Fig. 17—XPD or XPI versus rain rate for $\alpha = 70°$, 4 GHz, and circular polarization:

(a) $D_T' = 45$ DB (A) $D_R' = 20$ dB (D) $D_R' = 35$ dB
(b) $D_T' = 35$ dB (B) $D_R' = 25$ dB (E) $D_R' = 45$ dB
(F) $D_T' = D_R' = \infty$ (C) $D_R' = 30$ dB

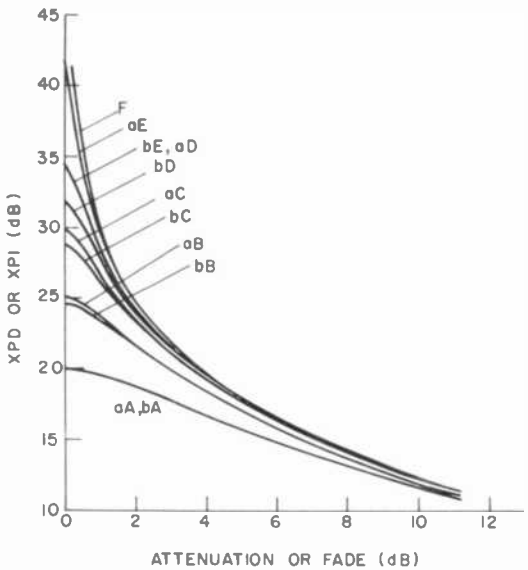

Fig. 18—XPD or XPI versus attenuation for $\alpha = 70°$, 11 GHz, and circular polarization:

(a) $D_T' = 45$ dB (A) $D_R' = 20$ dB (D) $D_R' = 35$ dB
(b) $D_T' = 35$ dB (B) $D_R' = 25$ dB (E) $D_R' = 45$ dB
(c) $D_T' = D_R' = \infty$ (C) $D_R' = 30$ dB

4. Other Causes of Depolarization

4.1 Faraday Rotation

Depolarization due to Faraday rotation within the ionosphere is of importance in satellite to earth links only for frequencies below 8 GHz. In the gigahertz range, the frequency is sufficiently larger than the plasma

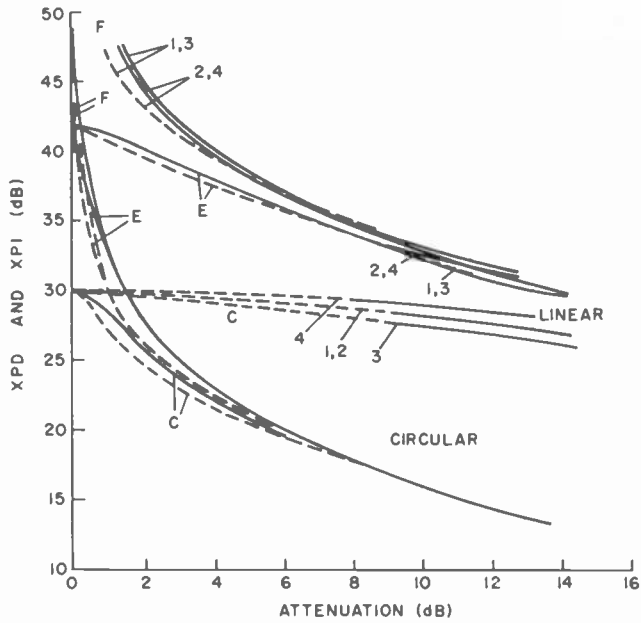

Fig. 19—XPD and XPI versus attenuation for $\alpha = 50°$, $\tau + \xi = 4°$, $\Theta = 0$, $D_T' = 45$ dB, and at 11 GHz. Solid curves use Eq. [29] for path length; dashed curves use Eq. (30):

(1) XPD_H (3) XPI_H (C) $D_R' = 30$ dB
(2) XPD_V (4) XPI_V (E) $D_R' = 45$ dB
(F) $D_R' = D_T' = \infty$

and cyclotron frequencies in the ionosphere so that attenuation is negligible. Then the angular rotation, Ω, of the electric field polarization is given to good accuracy by

$$\Omega = \frac{e^3}{2m_e{}^2\epsilon_0\omega^2 c} \int n_e \mathbf{B}_{0e} \cdot d\mathbf{l} \qquad [31]$$

Here e, m_e, and n_e are respectively the electron charge magnitude, mass and density, $\mathbf{B}_{0e}$ is the earth's magnetic field, ω is the angular frequency, c is the velocity of light and l is the path distance through the ionosphere.

The direction of rotation is opposite for a down link in relation to that of an up link. The clear weather isolation, denoted by CWI, and equivalent to XPD or XPI is given by

$$\text{CWI} = 20 \log_{10} \cot\Omega \qquad [32]$$

The electron density varies on a diurnal, seasonal, and yearly basis and also depends on sunspot and solar storm activity. On a diurnal basis, it is a minimum in the morning and a maximum in the afternoon. In the northern hemisphere, this diurnal change at 4.2 GHz, say in September, is about 1.5°, giving CWI = 32 dB. However, in other months of certain years, it can be as high as 4°, reducing CWI to only 23 dB (P. Foldes, private communication). Whereas these variations are predictable, those dependent on solar activity are not.

Since $\Omega \propto \omega^{-2}$, it is seen that at 8 GHz, the maximum value of Ω is less than 1°. Hence, Faraday rotation is completely negligible at frequencies above 8 GHz.

Faraday rotation only occurs for linear polarization and this phenomenon doesn't affect circular polarization.

4.2 Effects due to Interfering Satellites

We consider the interference arising from an unwanted satellite at an earth station, ordinarily receiving signals from a wanted closer satellite. The depolarization induced by rain is included in the calculation. Rain changes cross polarization partly to direct and vice versa, thereby introducing interference even if the transmitter of the satellite is cross-polarized to that of the receiver. The basic assumption is that the powers of the contributions to the interfering signal can be added, since the relative phases are usually random with respect to each other. This allows us to use the results in Appendix 2 based on the random phase limit. The notation is the same as there and the geometry is that pictured in Fig. 1 with ϕ_T being the off-axis angle of radiation from the interfering satellite and ϕ_R being the off-axis angle of the receiver. Let P_R be the interfering received power on dB, P_T the transmitted power by the unwanted satellite in dB, λ the wavelength and d the satellite to earth distance. As before r is the propagation path through the rain.

Consider first the case of the receiving antenna having nearly the same linear polarization as that of the interfering satellite. From Eqs. [103a,b] we obtain

$$
\begin{aligned}
&(P_R - P_T - G_T' - G_R')_{H,V} + 20\log_{10}(4\pi d/\lambda) + A_c \\
&= 10\log_{10}(F_{Ta}{}^2F_R{}^2P_{c\mp} + f_{Ta}{}^2f_R{}^2P_{c\pm} \\
&+ F_{Ta}{}^2f_R{}^2P_{s\mp} + f_{Ta}{}^2F_R{}^2P_{s\pm}) \\
&= 10\log_{10}[10^{-|F_T'+F_R'|/10}P_{c\mp} + 10^{-|f_T''+f_R'|/10}P_{c\pm} \\
&+ 10^{-|f_T'+f_R'|/10}P_{s\mp} + 10^{-|f_T''+F_R'|/10}P_{s\pm}]
\end{aligned}
\qquad [33]
$$

where the primes and double primes are defined in Eqs. [1] and [2], the subscripts designating receiver channels (a and b) are omitted, A_c is given by Eq. [95] and $P_{c\pm}$ and $P_{s\pm}$ are defined in Eqs. [102a,b]. Also $(P_R - P_T)_{H,V} \equiv 10\log_{10}|E_{Ra,Rb}|^2$. The upper signs refer to H and the lower signs to V polarization.

Consider next the same case with circular polarization. This follows from the above by setting $\Theta = 0$ and $\tau + \xi = 45°$ (see Appendix 2.2(B)) so that $P_{c\pm} = 1$ and $P_{s\pm} = p^2$. However the antenna patterns now refer to those for circular polarization. We obtain the same expression for right- and left-hand circular polarization upon using the assumption of random phases. The formula is now

$$
\begin{aligned}
&(P_R - P_T - G_T' - G_R')_c + 20\log_{10}(4\pi d/\lambda) + A_c \\
&= 10\log_{10}[10^{-|F_T'+F_R'|/10} + 10^{-|f_T''+f_R'|/10} \\
&+ 10^{-(|F_T'+f_R'|+\mathrm{XPD}_c)/10} + 10^{-(|F_R'+f_T''|+\mathrm{XPD}_c)/10}]
\end{aligned}
\qquad [34]
$$

where $\mathrm{XPD}_c = -10\log_{10}p^2$ for perfect antennas.

Consider the situation when the interfering satellite transmits nearly the orthogonal linear polarization to that of the receiving earth antenna. Using Eqs. [104a,b] and $(P_R)_{H,V} - (P_T)_{V,H} \equiv 10\log_{10}|E_{Rax,Rbx}|^2$, we find

$$
\begin{aligned}
&(P_R - G_R')_{H,V} - (P_T + G_T'')_{V,H} + 20\log_{10}(4\pi d/\lambda) + A_c \\
&= 10\log_{10}(f_{Tb}{}^2F_R{}^2P_{c\mp} + F_{Tb}{}^2f_R{}^2P_{c\pm} \\
&+ f_{Tb}{}^2f_R{}^2P_{s\mp} + F_{Tb}{}^2F_R{}^2P_{s\pm}) \\
&= 10\log_{10}[10^{-|f_T'+F_R'|/10}P_{c\mp} + 10^{-|F_T''+f_R'|/10}P_{c\pm} \\
&+ 10^{-|f_T'+f_R'|/10}P_{s\mp} + 10^{-|F_T''+F_R'|/10}P_{s\pm}]
\end{aligned}
\qquad [35]
$$

Finally, we consider the above situation with circular polarization. Again we obtain this result by letting $\Theta = 0$ and $\tau + \xi = 45°$, yielding

$$
\begin{aligned}
&(P_R - G_R')_{r,l} - (P_T + G_T'')_{l,r} + 20\log_{10}(4\pi d/\lambda) + A_c \\
&= 10\log_{10}[10^{-|f_T'+F_R'|/10} + 10^{-|F_T''+f_R'|/10} \\
&+ 10^{-(|f_T'+f_R'|+\mathrm{XPD}_c)/10} + 10^{-(|F_T''+F_R'|+\mathrm{XPD}_c)/10}]
\end{aligned}
\qquad [36]
$$

With the above formulas, one can calculate the signal at the earth receiver for any of the four situations. These expressions include the

dependence of the cross-polarization on the type of incident polarization and also include attenuation due to rain along the path.

4.3 Clear Air Refractive Index Variations as Related to Multipath Effects

Ghobrial and Watson[13] analyze the problem of bulk refractive effects causing ray bending and multipath propagation. Multipath propagation is due to stratification layers of refractive index in the troposphere (e.g. during temperature inversion conditions). An effect, similar to refractive index layers, can also arise due to ray bending from bulk refractive index and humidity variations, if they are large enough. Stutzman et al[14] observe a severe increase in cross polarization due to multipath propagation at low elevation angles in a link from the ATS-6 satellite (at 20 GHz) to earth. The elevation angle was about 5°. The copolarized signal jumped to 5 dB above the clear weather reference level and the XPD ratio became as low as 12 dB.

This effect can be analyzed in terms of our previous considerations on off-axis antenna reception, here due to multipath from rays arriving off-axis from the normal to the antenna. The increase in the copolarized component can be explained as due to an additional ray arriving with nearly the same amplitude as that of the direct signal. As shown for example in Fig. 2, the cross polarized reception pattern of a usual antenna has a minimum on axis. Hence, off-axis rays due to multipath effects can decrease the overall isolation, since they are displaced from the on-axis minimum reception direction.

Consider two rays eminating from the transmitter, one being a more or less direct ray #1 and the other #2 being refracted by the troposphere and let both signals reach the receiver. Let rays #1 and #2 be transmitted with the off-axis angles $\phi_{T1,2}$ and received at the off-axis angles $\phi_{R1,2}$. The signal from either ray upon reception gives rise to an electric field given by the sum of the direct ($\mathbf{i}_H$) and cross ($\mathbf{i}_V$) polarized components. Looking at the worst case of $\delta_{Ta} = \delta_{Ra} = -\delta_{Rb} = \pi/2$, $\Theta = 0$ and using Eqs. [18] and [92a,b] in the case of no rain, we obtain

$$\mathbf{E_D} = E_D \{[F_{Ra}(\phi_{R1})F_{Ta}(\phi_{T1}) + f_{Ra}(\phi_{R1})f_{Ta}(\phi_{T1})]\mathbf{i_H} + [f_{Rb}(\phi_{R1})F_{Ta}(\phi_{T1}) + F_{Rb}(\phi_{R1})f_{Ta}(\phi_{T1})]\mathbf{i_V}\} \quad [37a]$$

and

$$\mathbf{E_{MP}} = E_{MP}e^{i\varphi_E} \{[F_{Ra}(\phi_{R2})F_{Ta}(\phi_{T2}) + f_{Ra}(\phi_{R2})f_{Ta}(\phi_{T2})]\mathbf{i_H} + [f_{Rb}(\phi_{R2})F_{Ta}(\phi_{T2}) + F_{Rb}(\phi_{R2})f_{Ta}(\phi_{T2})]\mathbf{i_V}\} \quad [37b]$$

where $\mathbf{E_D}$ is the field due to the direct ray, $\mathbf{E_{MP}}$ is due to the multipath ray, and φ_E is the phase difference between $\mathbf{E_{MP}}$ and $\mathbf{E_D}$. As for the

constants in front, usually $E_D \approx E_{MP}$ in magnitude. The total field is $\mathbf{E_D} + \mathbf{E_{MP}}$ and the isolation or discrimination in clear weather (CWI) is the ratio in dB of the $\mathbf{i_H}$ to the $\mathbf{i_V}$ components. Thus denoting $F_{Ta1} = F_{Ta}(\phi_1)$, etc., for short, we have

$$\text{CWI} = 20 \log_{10} \times \left| \frac{E_D F_{Ta1} F_{Ra1} + E_{MP} e^{i\varphi_E} F_{Ta2} F_{Ra2}}{E_D (F_{Ta1} f_{Rb1} + F_{Rb1} f_{Ta1}) + E_{MP} e^{i\varphi_E} (F_{Ta2} f_{Rb2} + F_{Rb2} f_{Ta2})} \right| \qquad [38]$$

omiting the negligible $f_T f_R$ products.

Consider the following example. Let the direct ray propagate along the normals to both the transmitter and receiver apertures and let the cross-polarized components for this ray be negligible. Then $F_{Ta1} = F_{Ra1} = 1$ and $f_{Ta1} = f_{Ra1} = f_{Rb1} = 0$, recalling that the on-axis cross-polar pattern has a minimum. This gives

$$\text{CWI} = 10 \log_{10} \times \left[\frac{E_D{}^2 + (E_{MP} F_{Ta2} F_{Ra2})^2 + 2E_D E_{MP} \cos\varphi_E F_{Ta2} F_{Ra2}}{E_{MP}{}^2 (F_{Ta2} f_{Rb2} + F_{Rb2} f_{Ta2})^2} \right]. \qquad [39a]$$

This is the relation for the isolation given by Ghobrial and Watson[13] who assume in addition that $E_{MP} = E_D$ and $F_{Rb2} = F_{Ra2}$. Eq. [39a] reduces to the clear weather isolation due to the finite isolation of the imperfect antennas when $\varphi_E = 0$. Thus, CWI is reduced due to multipath rays which are detected with the phase delay φ_E.

The generalized form of Eq. [39a] for the case of a satellite to earth link where only the receiver plane may be perpendicular to the propagation direction is

$$\begin{aligned} \text{CWI} = 10 \log_{10} \{ & [(E_D F_{Ta1})^2 + (E_{MP} F_{Ta2} F_{Ra2})^2 \\ & + 2E_D E_{MP} \cos\varphi_E F_{Ta1} F_{Ta2} F_{Ra2}] \\ & \times [(E_D F_{Rb1} f_{Ta1})^2 + E_{MP}{}^2 (F_{Ta2} f_{Rb2} + F_{Rb2} f_{Ta2})^2 \\ & + 2E_D E_{MP} \cos\varphi_E F_{Rb1} f_{Ta1} (F_{Ta2} f_{Rb2} + F_{Rb2} f_{Ta2})]^{-1} \} \end{aligned} \qquad [39b]$$

using $F_{Ra1} = 1$ and $f_{Ra1} = f_{Rb1} = 0$. This shows the further reduction in CWI when $F_{Ta1} < 1$ and f_{Ta1} is nonnegligible. A Cutler front-fed paraboloidal antenna, having 45° cross-polar lobes 22 dB below the maximum co-polar value, gives[13] CWI = 14 dB as a worst case.

5. Compensation Methods and Correction Systems

Various compensation techniques have been proposed to correct for the cross talk induced by either Faraday rotation and/or by precipitation. These techniques are quite complex. They can be applied to the rf or to the i-f stage. The theory on rf compensation is given below. A rf correction system requires adjustments of phase, differential phase, and differential attenuation. For Faraday rotation or for low frequencies below 6 GHz, differential attenuation corrections are unnecessary.

An rf method of correcting for Faraday rotation was developed by P. Foldes of RCA Ltd. The system uses program tracking and predetermined calculations of Faraday phase variations that are expected to occur on a diurnal and seasonable basis due to ionospheric changes. The system involves only corrections for phase, which are adequate in the 4–6 GHz frequency range. Two ground stations for the RCA Satcom satellite incorporate such correction systems. To compensate for rain as well, one would require an additional tracking system to monitor the amount of unwanted cross-polarization.

An adaptive interference reduction network has been developed by Comsat to cancel out the cross-polarization (see Tseng[15] and references therein). A manually adjustable cross-polarization cancellation circuit has been incorporated in the forthcoming AT&T domestic satellite ground station (Chu, private communication*). Work is also progressing in England and in Italy to develop cancellation systems. Possible rf networks are discussed by Barton[16,17] and by Kannowade.[18]

In England, Evans and Thompson[19,20] have implemented on their terrestrial link a cancellation technique that increased their clear weather isolation to 60 dB. Barton[16,17] reviews adaptive cancellation techniques for frequency re-use satellite systems. He finds it unnecessary for the up-link in the 11–14 GHz band but desirable for the down-link.

The Italian effort is devoted mainly to provide cancellation in the i-f stage (Paraboni and Rocca[21]; Attisani et al.[22,23]). An electrical matrix is employed which produces a phase shifted and attenuated version of the signal in one channel that is equal in amplitude and in antiphase to the cross-talk in the other. The signal is then added to the other channel. The system provides complete static cancellation only at the fixed beacon frequency at the receiver. However, in a wide-band satellite communication system, the cancellation is incomplete at frequencies removed from the central frequency. This is because the signal passes through

* See also A. E. Williams and F. L. Frey, "Adaptive Polarization Control on a Dual-Polarized 4/6 GHz Satcom Link in the Presence of Rain," Electronics Lett., 2, No. 25, p. 686, Dec. 9, 1976.

filters, amplifiers and other network components that have nonuniform frequency characteristics. Thus the i-f cancellation technique has to be regarded as a narrow-band system. On the other hand, i-f systems have the advantage that the method is applicable to signals received from many satellites, whereas a separate rf system would be required for each satellite link.

In order to achieve compensation over a wide bandwidth, it is necessary to keep the two channels in the same waveguide and travelling at the same phase velocity. Difficulties can arise however with linear polarizations if the angle of polarization of the antenna varies over its design bandwidth and the overall isolation is not maintained at a constant value. Nonetheless, a wider bandwidth is achievable with an rf than with an i-f compensation system.

The theory below provides the analysis on rf compensation and follows the approach of Chu.[24,25] Suppose that the incoming signal consists of two elliptically polarized waves, which have been modified due to precipitation from the two orthogonally polarized waves originally transmitted. If the transmitted signals have linear or circular polarization, the ellipses are respectively slender or fat.

Consider first two linearly polarized waves that arrive as two slender ellipses. The transformation back to their original form is done in four stages. First the polarizations are made linear but not yet orthogonal. This is accomplished in two steps by a coordinate rotation combined with differential phase shift. Then the polarizations are made orthogonal by two more steps, namely another coordinate rotation combined with differential attenuation. Thus one requires two phase shifters such as rotary joints, a differential attenuator, a differential phase shifter and an orthomode transducer to separate the two modes.

Fig. 20a shows the two incoming nonorthogonal elliptically polarized waves 1 and 2. We are given their respective minor and major axes lengths, $B_{01,02}$ and $A_{01,02}$, and the angle θ between their major axes. Referring to Appendix 1, Eqs. [57], [58], and [77], we can represent the polarization ratios of the two ellipses by

$$p_{E1,2} = \frac{E_{oV1,2}}{E_{oH1,2}} = \frac{f_{1,2}}{F_{1,2}} \exp(i\delta_{1,2}) = \tan\gamma_{1,2} \exp(i\delta_{1,2}), \qquad [40]$$

where the significances of $f_{1,2}$ and $F_{1,2}$ are indicated in Fig. 22, Appendix 1.

The first step, involving a coordinate rotation, is to find a coordinate system such that the two ellipses are synchronized with respect to each other. That is, we require

$$\delta_1 = \delta_2 \quad \text{or} \quad \delta_1 + \pi = \delta_2, \qquad [41a]$$

both equivalent to

$$\tan\delta_1 = \tan\delta_2. \qquad [41b]$$

Now δ is related to A_0, B_0, and to the inclination angle σ by Eqs. [66a] and [68], viz

$$\tan\delta = \tan 2\mu/\sin 2\sigma \quad \text{where} \quad \tan\mu \equiv B_0/A_0. \qquad [42]$$

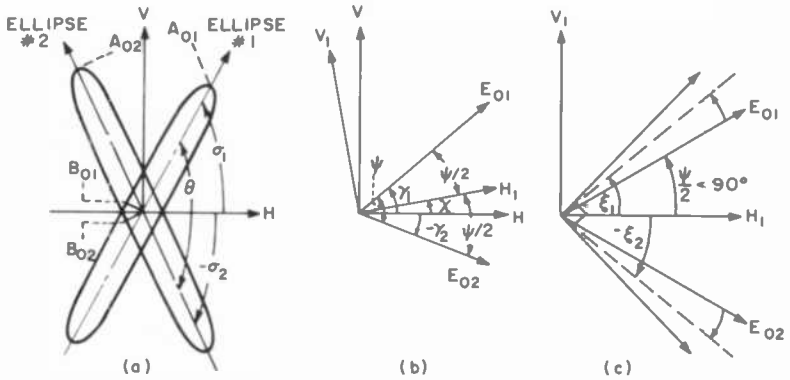

Fig. 20—Steps to recover two orthogonal linear polarizations.

Also note that*

$$\theta = \sigma_1 - \sigma_2, \qquad [43]$$

with σ_1 and σ_2 measured counterclockwise from the H axis. Combining Eqs. [41] and [42] gives

$$\frac{\tan 2\mu_2}{\tan 2\mu_1} = \frac{\sin 2(\sigma_1 - \theta)}{\sin 2\sigma_1} \quad \text{with} \quad 0 < \sigma_1 < \pi/2.$$

This yields the angle σ_1 that the major axis of ellipse 1 subtends with respect to the H-axis, namely

$$\sigma_1 = \frac{1}{2}\cot^{-1}\left[\left(\cos 2\theta - \frac{\tan 2\mu_2}{\tan 2\mu_1}\right)\Big/\sin 2\theta\right]$$

$$= \frac{1}{2}\cot^{-1}\left[\cot 2\theta - \frac{B_{02}A_{02}}{B_{01}A_{01}\sin 2\theta}\left(\frac{A_{01}^2 - B_{01}^2}{A_{02}^2 - B_{02}^2}\right)\right]. \qquad [44]$$

This positions the axes of the H-V coordinate system.

Step two requires applying a differential phase shift in order to

* The symbols θ, ψ, χ, ξ, and α have different meanings in this section from elsewhere in this paper.

transform the ellipses to two linear waves. Eq. [40] shows that this can be accomplished by subtracting from δ_1 a phase equal to δ_1. Then by Eq. [41a], δ_2 becomes automatically 0 or π. Thus both waves are linearized simultaneously by introducing a phase delay equal to δ_1 or δ_2 to the system. Since δ is the phase delay between E_{oH} and E_{oV} (see Eq. [40]), the differential phase shift between E_{oH} and E_{oV} should be applied to E_{oV} if $\delta > 0$ and to E_{oH} if $\delta < 0$. After this step, the angle between the two resulting linear polarizations is not θ but rather ψ, given by (see Fig. 20b)

$$\psi = \gamma_1 \pm \gamma_2 = \tan^{-1}|p_{E1}| \pm \tan^{-1}|p_{E2}|. \qquad [45]$$

The top sign applies if originally $\delta_2 = \delta_1 + \pi$ and the bottom sign if $\delta_2 = \delta_1$. [In the Poincaré sphere representation[25] (see Fig. 24, Appendix 1), by adjusting δ_1 to zero, the arc OP on the sphere has been rotated about 0 to the equator, resulting in $\gamma_{1,2}$ replacing $\sigma_{1,2}$.] From Eqs. [65a,b] and [73], we express $\gamma_{1,2}$ in terms of known quantities.

$$\tan^2\gamma = \frac{A_0^2 + B_0^2 - (A_0^2 - B_0^2)\cos 2\sigma}{A_0^2 + B_0^2 + (A_0^2 - B_0^2)\cos 2\sigma} = \frac{1 - \cos 2\sigma \cos 2\mu}{1 + \cos 2\sigma \cos 2\mu}. \qquad [46]$$

Given $\sigma_{1,2}$ from Eqs. [43] and [44], $A_{01,2}$ and $B_{01,2}$, we can calculate $\gamma_{1,2}$ and then ψ.

The next steps aim at changing ψ to 90° in order to effect orthogonality. First we draw a new coordinate system H_1, V_1, shown in Fig. [20b], which bisects the angle ψ between the two linear polarization vectors, $\mathbf{E}_{01}$ and $\mathbf{E}_{02}$. We rotate the H, V axes using a phase shifter to coincide with the new H_1, V_1 coordinate system. The angle of rotation, χ, is given by

$$\chi = \gamma_1 - \psi/2 = \tfrac{1}{2}(\gamma_1 \mp \gamma_2). \qquad [47]$$

In the last step, differential attenuation is applied to change ψ to 90°. If $\psi < 90°$, the differential attenuation is exerted along the H_1 axis, thereby widening the angle between $\mathbf{E}_{01}$ and $\mathbf{E}_{02}$. The amount of differential attenuation, α, is obtained from the relations for the ratios of the V_1 to H_1 components of $\mathbf{E}_{01}$ and $\mathbf{E}_{02}$ after attenuation (see Fig. 20c). Denoting these ratios by $\tan\xi_{1,2}$ we have

$$\tan\xi_1 = \tan(\psi/2)e^{\alpha} \quad \text{and} \quad \tan\xi_2 = -\tan(\psi/2)e^{\alpha}.$$

The values of $\xi_{1,2}$ are adjusted until $\xi_1 - \xi_2 = 90°$ or $\tan\xi_1 \tan\xi_2 + 1 = 0$ yielding

$$\alpha = \ln[\cot(\psi/2)]. \qquad [48a]$$

If on the other hand, $\psi > 90°$, then the angle between the $\mathbf{E}_{01}$ and $\mathbf{E}_{02}$ vectors is decreased by applying differential attenuation along the V_1

axis. The amount, α, is derived from $\xi_1 - \xi_2 = 90°$ and $\tan\xi_{1,2} = \pm\tan(\psi/2)e^{-\alpha}$ yielding

$$\alpha = \ln[\tan(\psi/2)]. \qquad [48b]$$

Chu[25] shows that the minimum α required to accomplish orthogonality is obtained in the above orientation of the H_1 and V_1 axes which bisects the angle ψ.

Consider now the case of two circularly polarized waves which are transmitted and two fat ellipses that are received as shown in Fig. 21a. The first steps are to transform the two ellipses into oppositely rotating ellipses having parallel major and minor axes and equal axial ratios as shown in Fig. 21b. That is, we want to transform the polarization ratios of the two ellipses to

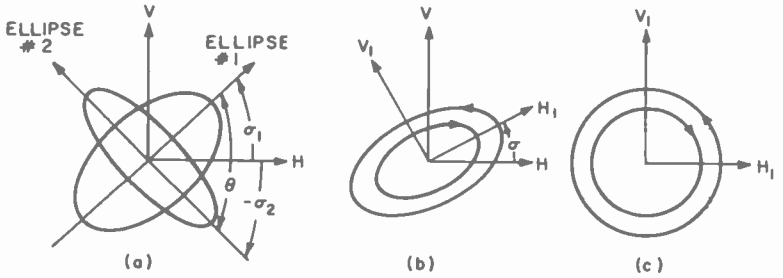

Fig. 21—Steps to recover two orthogonal circular polarizations.

$$p_{E1,2} = \tan\gamma \exp(\pm i\delta). \qquad [49]$$

To accomplish this, we first search for a coordinate system such that $\gamma_1 = \gamma_2 = \gamma$ say. From Eq. [46], we obtain the angle σ_1:

$$\sigma_1 = \frac{1}{2}\tan^{-1}\left\{\left[\frac{\cos2\mu_1}{\cos2\mu_2} - \cos2\theta\right]\Big/\sin2\theta\right\}, \quad 0 < \sigma_1 < \pi/2, \qquad [50]$$

with $\sigma_2 = \sigma_1 - \theta$. This locates the H,V coordinate system in Fig. 21a. Next we have to adjust the δ's by inserting a differential phase delay, equal to say Δ, acting on each of the phases, δ_1 and δ_2 of the ellipses. To satisfy Eq. [49], we require

$$\delta = \delta_1 - \Delta \quad \text{and} \quad -\delta = \delta_2 - \Delta,$$

which gives

$$\Delta = (\delta_1 + \delta_2)/2 \quad \text{and} \quad \delta = (\delta_1 - \delta_2)/2. \qquad [51a]$$

By Eq. [42] we write Δ and δ in terms of known parameters:

$$\begin{bmatrix} \Delta \\ \delta \end{bmatrix} = \frac{1}{2}\left[\tan^{-1}\left(\frac{\tan 2\mu_1}{\sin 2\sigma_1}\right) \pm \tan^{-1}\left(\frac{\tan 2\mu_2}{\sin 2\sigma_2}\right) \right]$$

$$\text{where} \quad \tan\mu_{1,2} = \frac{B_{01,2}}{A_{01,2}}. \qquad [51b]$$

In the modified situation shown in Fig. (21b), the angle σ of both ellipses with respect to the H-axis can be obtained from Eq. [75], namely

$$\tan 2\sigma = \tan 2\gamma \cos\delta. \qquad [52]$$

Also the new ratio of minor to major axes, $\tan\mu$, for either ellipse is calculable from Eq. [74]:

$$\sin 2\mu = \sin 2\gamma \sin\delta. \qquad [53]$$

In Eqs. [52] and [53], δ is given by Eq. [51b] and $\gamma = \gamma_1$ is given by Eq. [46] in terms of μ_1 and σ_1.

The last steps involve reducing the two ellipses to circles as shown in Fig. (21c). For this purpose, we apply a differential attenuation equal to α along the major axis, H_1, of the transformed ellipses to the extent $e^{-\alpha} = \tan\mu$. Thus α is given by

$$\alpha = \ln(\cot\mu)$$

In addition to the above, circular polarization systems also require a polarizer giving a 90° differential phase shift to convert to the final linearly polarized ports. Kannowade[18] points out that dual circular polarizations can be treated similar to linear systems by either inserting a polarizer between the antenna and the compensation network or by using the differential phase shifter in the compensation network itself, provided its range is of the order of 90°.

The above completes the theory on rf compensation systems.

6. Conclusions

To perform proper comparisons with theory or with other experiments on the effect of rain alone, a clear-weather isolation for the antennas of better than 32 dB is desirable. We have modified the theory to include these finite isolation effects so that the results from such imperfect experiments can be analyzed. The parameter have been varied systematically to investigate the various trends. Interesting effects are found due to finite polarization angle, off-axis reception, misalignment in the case of linear polarization, and relative magnitudes of the receiver-to-transmitter isolations in clear weather. Additional causes of depolarization have also been outlined, namely interference resulting from ad-

jacent satellites and from multipath propagation. Finally, compensation systems can be designed either in the rf or in the i-f stage. Each has its own advantages and disadvantages.

7. Acknowledgments

This work was partly sponsored by the Department of Industry, Trade and Commerce, Ottawa, Canada, under DITC Project No. 13ST-67043-4-2139, DITC Serial No. 9SP4-005. The author wishes to acknowledge helpful discussions and consultations with F. J. F. Osborne, H. J. Moody, P. Foldes, A. R. Raab, J. R. G. Cox, C. M. Kudsia, and H. Staras.

Appendix 1—Various Representations of Elliptically Polarized Fields

Consider Fig. 22. Let the signal be elliptically polarized with the H' major axis inclined at an angle σ with respect to the horizontal H-axis. Let A_0 and B_0 be the lengths of the major and minor axes respectively and let F and f be the maximum values of the H and V components respectively attained by the field E. Then we can write

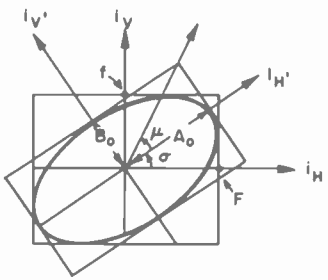

Fig. 22—An elliptically polarized electric field.

$$\mathrm{Re}(E_H) = F\cos(kr - \omega t + \zeta) \quad \text{and}$$
$$\mathrm{Re}(E_V) = f\cos(kr - \omega t + \zeta + \delta) \qquad [54]$$

where δ is the phase difference. Our convention throughout is to adopt an $\exp(-i\omega t)$ time dependence. Let

$$\mathbf{E} = \mathbf{E}_0\exp[i(kr - \omega t + \zeta)], \quad \mathbf{E} = E_H\mathbf{i}_H + E_V\mathbf{i}_V \qquad [55]$$

$$E_H = F\exp[i(kr - \omega t + \zeta)] \quad \text{and}$$
$$E_V = f\exp[i(kr - \omega t + \zeta + \delta)], \qquad [56]$$

so that

$$E_{oH} = F \quad \text{and} \quad E_{oV} = f \exp(i\delta). \tag{57}$$

Define the polarization ratio as

$$p_E \equiv \frac{E_{oV}}{E_{oH}} = \frac{f}{F} e^{i\delta}, \tag{58}$$

and the quantity q as

$$q = \frac{1 - ip_E}{1 + ip_E} = \frac{E_{oH} - iE_{oV}}{E_{oH} + iE_{oV}} = \frac{1 - (ife^{i\delta}/F)}{1 + (ife^{i\delta}/F)}. \tag{59}$$

The values of $\delta = 0$ or π, $p_E = 0, \infty, i, -i$, $\delta > 0$, and $\delta < 0$ correspond respectively to linear, horizontal, vertical, left-hand circular, right-hand circular, left-hand elliptical, and right-hand elliptical for a wave propagating along the positive r direction.

Eliminating $kr - \omega t + \zeta$ from Eq. [55], we obtain the equation for the ellipse

$$\left[\frac{\mathrm{Re}(E_H)}{F}\right]^2 - \frac{2\mathrm{Re}(E_H)\mathrm{Re}(E_V)\cos\delta}{Ff} + \left[\frac{\mathrm{Re}(E_V)}{f}\right]^2 = \sin^2\delta. \tag{60}$$

Rotate the axes through an angle σ (See Fig. 22) to another (H', V') Cartesian coordinate system, such that

$$\mathrm{Re}E_H + i\mathrm{Re}E_V = [\mathrm{Re}(E_{H'}) + i\mathrm{Re}(E_{V'})]e^{i\sigma}$$

$$\text{where} \quad \tan 2\sigma = \frac{2Ff\cos\delta}{F^2 - f^2}. \tag{61}$$

We obtain

$$\left[\frac{\mathrm{Re}(E_{H'})}{A_0}\right]^2 + \left[\frac{\mathrm{Re}(E_{V'})}{B_0}\right]^2 = 1 \tag{62}$$

with

$$A_0{}^2 = \frac{F^2\cos^2\sigma - f^2\sin^2\sigma}{2\cos^2\sigma - 1} = \frac{1}{2}\left[F^2 + f^2 + \frac{F^2 - f^2}{\cos 2\sigma}\right] \tag{63}$$

$$B_0{}^2 = \frac{f^2\cos^2\sigma - F^2\sin^2\sigma}{2\cos^2\sigma - 1} = \frac{1}{2}\left[F^2 + f^2 - \frac{F^2 - f^2}{\cos 2\sigma}\right]. \tag{64}$$

Inverting yields

$$F^2 = \tfrac{1}{2}[A_0^2 + B_0^2 + (A_0^2 - B_0^2)\cos 2\sigma] \quad [65a]$$

$$f^2 = \tfrac{1}{2}[A_0^2 + B_0^2 - (A_0^2 - B_0^2)\cos 2\sigma] \quad [65b]$$

$$F^2 + f^2 = A_0^2 + B_0^2 \quad \text{and}$$

$$F^2 - f^2 = (A_0^2 - B_0^2)\cos 2\sigma. \quad [65c,d]$$

Let us define the angle μ as shown in Fig. 22 and the quantity I as follows:

$$\tan\mu = B_0/A_0 \quad \text{and}$$

$$I \equiv F^2 + f^2 = A_0^2 + B_0^2 = |E_{oH}|^2 + |E_{oV}|^2. \quad [66a,b]$$

Then we obtain

$$A_0 = I\cos\sigma, \quad B_0 = I\sin\sigma \quad [67a,b]$$

$$F^2 = \frac{I}{2}(1 + \cos 2\mu\cos 2\sigma), \quad f^2 = \frac{I}{2}(1 - \cos 2\mu\cos 2\sigma). \quad [67c,d]$$

From Eq. [61] and Fig. 23, we can derive

$$\tan\delta = \tan 2\mu/\sin 2\sigma. \quad [68]$$

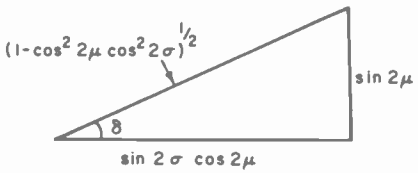

Fig. 23—The angle δ.

Thus Eqs. [57] to [59] become

$$E_{oH} = F = \left[\frac{I}{2}(1 + \cos 2\mu\cos 2\sigma)\right]^{1/2} \quad [69a]$$

$$E_{oV} = f\cos\delta + if\sin\delta = \left[\frac{I}{2(1 + \cos 2\mu\cos 2\sigma}\right]^{1/2}$$

$$\times (\sin 2\sigma\cos 2\mu + i\sin 2\mu) \quad [69b]$$

$$\frac{E_{oV}}{E_{oH}} = \left[\frac{1 - \cos 2\mu\cos 2\sigma}{1 + \cos 2\mu\cos 2\sigma}\right]^{1/2} \exp\left[i\tan^{-1}\left(\frac{\tan 2\mu}{\sin 2\sigma}\right)\right]$$

$$= \frac{\sin 2\sigma\cos 2\mu + i\sin 2\mu}{1 + \cos 2\mu\cos 2\sigma} \quad [70a]$$

$$E_{oV} \pm iE_{oH} = \left[\frac{2I}{1 + \cos 2\mu\cos 2\sigma}\right]^{1/2} \times$$

$$\times (\cos\mu \cos\sigma + i \sin\mu \sin\sigma)(\cos\mu \mp \sin\mu) \exp(\pm i\sigma) \qquad [70b]$$

and

$$q = \frac{E_{oV} - iE_{oH}}{E_{oV} + iE_{oH}} = \tan\left(\mu + \frac{\pi}{4}\right) \exp(-2i\sigma). \qquad [70c]$$

In terms of rotating coordinates, we define

$$E_{or} = \frac{1}{\sqrt{2}}(E_{oV} - iE_{oH}) \quad \text{and} \quad E_{ol} = \frac{1}{\sqrt{2}}(E_{oV} + iE_{oH}). \qquad [71]$$

Right-hand circular polarization is the one rotating clockwise when viewed in the direction of propagation and left-hand circular is the one rotating counterclockwise. Then Eq. [70b] becomes

$$E_{or} = Cm \quad \text{and} \quad E_{ol} = Cn^* \qquad [72a,b]$$

with

$$m = \sin(\mu + \pi/4)e^{-i\sigma}, \quad n = \cos(\mu + \pi/4)e^{-i\sigma} \qquad [72c,d]$$

and

$$C = \left[\frac{2I}{1 + \cos2\mu \cos2\sigma}\right]^{1/2} (\cos\mu \cos\sigma + i \sin\mu \sin\sigma). \qquad [72e]$$

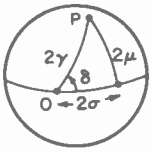

Fig. 24—Poincaré spherical system representation.

There are several other representations of an elliptically polarized field. One is the Poincaré representation which uses the coordinates on a spherical surface as shown in Fig. 24. Let O be a reference point on the equator and let P be the point on the surface designating a given polarization. Let the latitude be 2μ and let the longitude be 2σ. Let δ be the angle to point P at the equator and let 2γ be the distance OP. Using spherical angle relationships, we find that

$$\cos2\gamma = \cos2\sigma \cos2\mu \quad \text{or} \quad 2\cos^2\gamma = 1 + \cos2\sigma \cos2\mu$$
$$\text{or} \quad 2\sin^2\gamma = 1 - \cos2\sigma \cos2\mu \qquad [73]$$

$$\sin2\mu = \sin2\gamma \sin\delta \qquad [74]$$

$$\tan2\sigma = \tan2\gamma \cos\delta \qquad [75]$$

and

$$\sin 2\sigma \cos 2\mu = \sin 2\gamma \cos\delta. \qquad [76]$$

We also have as in Eq. [68] or from Eqs. [74] and [76]

$$\tan 2\mu = \tan\delta \sin 2\sigma.$$

Using these relations, Eqs. [57] and [67c,d] become

$$E_{oH} = F = \sqrt{I}\cos\gamma, \quad f = \sqrt{I}\sin\gamma \quad \text{and}$$
$$2Ff = I \sin 2\gamma = I \sin 2\mu/\sin\delta$$

$$E_{oV} = \sqrt{I}\sin\gamma\,(\cos\delta + i\sin\delta) \quad \text{and}$$
$$E_{oV}/E_{oH} = \tan\gamma \exp(i\delta). \qquad [77]$$

Another representation uses the Stokes parameters, denoted by I, Q, U, and V. (Do not confuse the latter three with their meanings elsewhere.) The parameters are defined by

$$I = E_H E_H^* + E_V E_V^*, \quad Q = E_H E_H^* - E_V E_V^* \qquad [78a,b]$$

$$U = E_H E_V^* + E_V E_H^* \quad \text{and}$$
$$V = i(E_H E_V^* - E_V E_H^*). \qquad [78c,d]$$

Using Eqs. [56], [65c,d], [67c,d], [73], [74], [76], and [77] we obtain

$$I = F^2 + f^2 = A_0^2 + B_0^2, \quad \text{as in Eq. [66b]}$$

$$Q = F^2 - f^2 = (A_0^2 - B_0^2)\cos 2\sigma = I \cos 2\mu \cos 2\sigma = I \cos 2\gamma \qquad [79a]$$

$$U = 2Ff\cos\delta = I \sin 2\gamma \cos\delta = I \cos 2\mu \sin 2\sigma = Q \tan 2\sigma \qquad [79b]$$

$$V = 2Ff \sin\delta = I \sin 2\gamma \sin\delta = I \sin 2\mu$$
$$= Q \tan 2\mu/\cos 2\sigma = Q \tan 2\gamma \sin\delta. \qquad [79c]$$

Note that

$$I^2 = Q^2 + U^2 + V^2. \qquad [80]$$

Also, inverting yields

$$F^2 = (I + Q)/2, \quad f^2 = (I - Q)/2, \quad 2Ff = (I^2 - Q^2)^{1/2} \qquad [81a,b,c]$$

$$\cos\delta = U/(I^2 - Q^2)^{1/2}, \quad \sin\delta = V/(I^2 - Q^2)^{1/2},$$
$$\tan\delta = V/U \qquad [81d,e,f]$$

$$E_{oV} = f \exp(i\delta) = (U + iV)/[2(I + Q)]^{1/2} \quad \text{and}$$
$$E_{oH} = [(I + Q)/2]^{1/2}. \qquad [82a,b]$$

The power detected by two orthogonal receivers can be represented

in terms of the Stokes parameters (I_0, Q_0, U_0, V_0) associated with an incident field. Let x_0, x_1, x_2, and x_3 be parameters to be determined for feed a, and y_0, y_1, y_2, and y_3 be corresponding parameters for feed b, such that

$$\begin{pmatrix} |E_{Ra}|^2/|\kappa_{Ra}|^2 \\ |E_{Rbx}|^2/|\kappa_{Rb}|^2 \end{pmatrix} = \begin{pmatrix} x_0\, x_1\, x_2\, x_3 \\ y_0\, y_1\, y_2\, y_3 \end{pmatrix} \begin{pmatrix} I_0 \\ Q_0 \\ U_0 \\ V_0 \end{pmatrix} \qquad [83]$$

where $\kappa_{Ra,b}$ is given in Eq. [19] in the text. From Eqs. (5) in the text and with Eqs. [82a,b] we have

$$\begin{pmatrix} E_{Ra}/\kappa_{Ra} \\ E_{Rbx}/\kappa_{Rb} \end{pmatrix} = \Lambda_R^{-1} \cdot \begin{pmatrix} E_{oH} \\ E_{oV} \end{pmatrix}$$

$$= \begin{pmatrix} F_{Ra} & f_{Ra} \exp(-i\delta_{Ra}) \\ if_{Rb} \exp(i\delta_{Rb}) & -iF_{Rb} \end{pmatrix} \begin{pmatrix} 1 \\ \dfrac{U_0 + iV_0}{I_0 + Q_0} \end{pmatrix}$$

$$\times \left(\frac{I_0 + Q_0}{2}\right)^{1/2} \qquad [84]$$

where I_0, Q_0, U_0, and V_0 are the Stokes parameters for E_{RH} and E_{RV}. From Eq. [84] we obtain

$$|E_{Ra}|^2/|\kappa_{Ra}|^2 = \frac{1}{2} F_{Ra}{}^2(I_0 + Q_0) + \frac{1}{2} f_{Ra}{}^2 \left(\frac{U_0{}^2 + V_0{}^2}{I_0 + Q_0}\right)$$

$$+ F_{Ra} f_{Ra}(U_0 \cos\delta + V_0 \sin\delta). \qquad [85]$$

For the middle term, using Eq. [80], we have $(U_0{}^2 + V_0{}^2)/(I_0 + Q_0) = I_0 - Q_0$. Thus comparing Eqs. [83] and [85] we obtain

$$x_0 = \tfrac{1}{2}(F_{Ra}{}^2 + f_{Ra}{}^2), \quad x_1 = \tfrac{1}{2}(F_{Ra}{}^2 - f_{Ra}{}^2),$$
$$x_2 = F_{Ra} f_{Ra} \cos\delta_{Ra} \quad \text{and} \quad x_3 = F_{Ra} f_{Ra} \sin\delta_{Ra}. \qquad [86]$$

Similarly for E_{Rbx}, we can deduce

$$y_0 = \tfrac{1}{2}(F_{Rb}{}^2 + f_{Rb}{}^2), \quad y_1 = -\tfrac{1}{2}(F_{Rb}{}^2 - f_{Rb}{}^2),$$
$$y_2 = -F_{Rb} f_{Rb} \cos\delta_{Rb} \quad \text{and} \quad y_3 = -F_{Rb} f_{Rb} \sin\delta_{Rb}. \qquad [87]$$

Inverting these relations gives

$$F_{Ra} = (x_0 + x_1)^{1/2}, \quad f_{Ra} = (x_0 - x_1)^{1/2} \qquad [88a,b]$$

$$F_{Rb} = (y_0 - y_1)^{1/2}, \quad f_{Rb} = (y_0 + y_1)^{1/2} \qquad [88c,d]$$

$$\cos\delta_{Ra} = x_2/(x_0^2 - x_1^2)^{1/2}, \quad \sin\delta_{Ra} = x_3/(x_0^2 - x_1^2)^{1/2} \quad [89a,b]$$

$$\cos\delta_{Rb} = -y_2/(y_0^2 - y_1^2)^{1/2} \quad \text{and}$$

$$\sin\delta_{Rb} = -y_3/(y_0^2 - y_1^2)^{1/2}. \quad [89c,d]$$

The matrix Λ_R^{-1} becomes

$$\Lambda_R^{-1} = \begin{pmatrix} (x_0 + x_1)^{1/2} & & \\ & i(y_0 + y_1)^{1/2} \exp\left[i \tan^{-1}\left(\frac{y_3}{y_2}\right)\right] & \\ & & (x_0 - x_1)^{1/2} \exp\left[-i \tan^{-1}\left(\frac{x_3}{x_2}\right)\right] \\ -i(y_0 - y_1) & & \end{pmatrix}. \quad [90]$$

Relations similar to these are given by Bostian,[1] but several errors of his are corrected here. The former representation is used in the text.

Appendix 2—Matrix Elements Including Propogation and Antenna Effects

A2.1 Theory for Linear Polarization

For predominantly linearly polarized waves, the result of the matrix multiplications in Eq. [18] in the text can be written

$$\Lambda_R^{-1} \cdot \Psi_R \cdot V^{-1} \cdot B \cdot V \cdot \Psi_T \cdot \Lambda_T = \Upsilon \left\{ \frac{\exp\left[-\frac{r}{2}(\alpha_1 + \alpha_2) + \frac{ir}{2}(\beta_1 + \beta_2)\right]}{[1 - p^2 \exp(-2i\chi)]^{1/2}} \right\}. \quad [91]$$

The matrix elements are

$$\begin{aligned} \Upsilon_{11,22} &= [F_{Ra,b}F_{Ta,b} + f_{Ra,b}f_{Ta,b} \exp(\pm i(\delta_{Ta,b} - \delta_{Ra,b}))] \cos\Theta \\ &\mp [F_{Ra,b}F_{Ta,b} - f_{Ra,b}f_{Ta,b} \exp(\pm i(\delta_{Ta,b} - \delta_{Ra,b}))] \\ &\times pe^{-i\chi} \cos(2\tau + 2\xi + \Theta) \\ &+ [F_{Ta,b}f_{Ra,b} \exp(\mp i\delta_{Ra,b}) - F_{Ra,b}f_{Ta,b} \exp(\pm i\delta_{Ta,b})] \sin\Theta \\ &\mp [F_{Ta,b}f_{Ra,b} \exp(\mp i\delta_{Ra,b}) + F_{Ra,b}f_{Ta,b} \exp(\pm i\delta_{Ta,b})] \\ &\times pe^{-i\chi} \sin(2\tau + 2\xi + \Theta) \end{aligned} \quad [92a]$$

and

$$
\begin{aligned}
\Upsilon_{12,21} = i\{&[F_{Tb,a}f_{Ra,b}\exp(\mp i\delta_{Ra,b}) \\
&- F_{Ra,b}f_{Tb,a}\exp(\mp i\delta_{Tb,a})]\cos\Theta \\
&\pm [F_{Tb,a}f_{Ra,b}\exp(\mp i\delta_{Ra,b}) + F_{Ra,b}f_{Tb,a}\exp(\mp i\delta_{Tb,a})] \\
&\times pe^{-ix}\cos(2\tau + 2\xi + \Theta) \\
&- [F_{Tb,a}F_{Ra,b} + f_{Tb,a}f_{Ra,b}\exp(\mp i(\delta_{Ra,b} + \delta_{Tb,a}))]\sin\Theta \\
&\mp [F_{Tb,a}F_{Ra,b} - f_{Tb,a}f_{Ra,b}\exp(\mp i(\delta_{Ra,b} + \delta_{Tb,a}))] \\
&\times pe^{-ix}\sin(2\tau + 2\xi + \Theta)\}
\end{aligned}
\qquad [92b]
$$

To apply these relations, we require a knowledge of the phase angles $\delta_{Ta,b}$ and $\delta_{Ra,b}$. Two alternate limits are sometimes adopted. The first limit looks for the worst case of clear weather isolation which is obtained by setting $\delta_{Ta} = \delta_{Tb} = \pi/2$ and $\delta_{Ra} = \delta_{Rb} = -\pi/2$. Then for $p = 0$, $\Upsilon_{11,22}$ are minimized and $\Upsilon_{12,21}$ are maximized. The second limit assumes random phases for δ, as in arbitrarily modulated signals.

(A) Worst Phase Limit

Consider limit 1 with $\delta_{Ta,b} = -\delta_{Ra,b} = \pi/2$. Define $D_{T'}(\phi_T)$ and $D_{T''}(\phi_T)$ in dB to be the clear weather finite discrimination or isolation of the transmitter antenna in the two orthogonal directions given by

$$
D_{T'} = F_{T'} - f_{T''} \quad \text{and} \quad D_{T''} = F_{T''} - f_{T'} \quad \text{in dB} \qquad [93a]
$$

or

$$
\begin{aligned}
&D_{Ta} \equiv 10^{D_{T'}/20} = F_{Ta}/f_{Ta} \quad \text{and} \\
&D_{Tb} \equiv 10^{D_{T''}/20} = F_{Tb}/f_{Tb}
\end{aligned}
\qquad [93b]
$$

where the patterns F and f are defined in the text, Eq. [1]. Similarly, define $D_{R'}(\phi_R)$ and $D_{R''}(\phi_R)$ in dB to be corresponding quantities for the receiver given by

$$
D_{R'} = F_{R'} - f_{R'} \quad \text{and} \quad D_{R''} = F_{R''} - f_{R''} \quad \text{in dB} \qquad [94a]
$$

or

$$
\begin{aligned}
&D_{Ra} \equiv 10^{D_{R'}/20} = F_{Ra}/f_{Ra} \quad \text{and} \\
&D_{Rb} \equiv 10^{D_{R''}/20} = F_{Rb}/f_{Rb}.
\end{aligned}
\qquad [94b]
$$

Finally define the attenuation quantity, A_c in dB, by

$$
\begin{aligned}
A_c &= 10\log_{10}\left\{\frac{\exp[-r(a_1 + a_2)]}{[(1 - p^2\cos 2\chi)^2 + p^4\sin^2 2\chi]^{1/2}}\right\} \\
&= 8.686(\alpha_1 + \alpha_2)\frac{r}{2} + 5\log_{10}[(1 + p^2)^2 - 4p^2\cos^2\chi].
\end{aligned}
\qquad [95]
$$

Using Eqs. [18] and [19] in the text, the square of the magnitudes of the electric field components are given by

$$|E_{Ra,Rb}|^2 = \left(\frac{\lambda}{4\pi d}\right)^2 G_{Ta,b} G_{Ra,b}\, 10^{-A_c/10} F_{Ta,b}{}^2 f_{Ra,b}{}^2 N_{\mp} \quad [96a]$$

where

$$\begin{aligned} N_{\mp} \equiv\ & [(D_{Ra,b} - D_{Ta,b}{}^{-1})\cos\Theta \\ & \mp (D_{Ra,b} + D_{Ta,b}{}^{-1}) p \cos\chi \cos(2\tau + 2\xi + \Theta) \\ & - (1 + D_{Ra,b} D_{Ta,b}{}^{-1}) p \sin\chi \sin(2\tau + 2\xi + \Theta)]^2 \\ & + [(1 - D_{Ra,b} D_{Ta,b}{}^{-1}) \sin\Theta \\ & + (D_{Ra,b} + D_{Ta,b}{}^{-1}) p \sin\chi \cos(2\tau + 2\xi + \Theta) \\ & \mp (1 + D_{Ra,b} D_{Ta,b}{}^{-1}) p \cos\chi \sin(2\tau + 2\xi + \Theta)]^2. \end{aligned} \quad [96b]$$

$$|E_{Rax,Rbx}|^2 = \left(\frac{\lambda}{4\pi d}\right)^2 G_{Tb,a} G_{Ra,b} \times 10^{-A_c/10} F_{Tb,a}{}^2 f_{Ra,b}{}^2 D_{\pm} \quad [97a]$$

where

$$\begin{aligned} D_{\pm} \equiv\ & [(1 + D_{Ra,b} D_{Tb,a}{}^{-1})\cos\Theta \\ & \pm (1 - D_{Ra,b} D_{Tb,a}{}^{-1}) p \cos\chi \cos(2\tau + 2\xi + \Theta) \\ & + (D_{Ra,b} - D_{Tb,a}{}^{-1}) p \sin\chi \sin(2\tau + 2\xi + \Theta)]^2 \\ & + [(D_{Ra,b} + D_{Tb,a}{}^{-1}) \sin\Theta \\ & - (1 - D_{Ra,b} D_{Tb,a}{}^{-1}) p \sin\chi \cos(2\tau + 2\xi + \Theta) \\ & \pm (D_{Ra,b} - D_{Tb,a}{}^{-1}) p \cos\chi \sin(2\tau + 2\xi + \Theta)]^2. \end{aligned} \quad [97b]$$

The respective values of $XPD_{H,V}$ and $XPI_{H,V}$ are given by

$$XPD_{H,V} = 20 \log_{10} \left|\frac{E_{Ra,Rb}}{E_{Rbx,Rax}}\right| \quad [98a]$$

and

$$XPI_{H,V} = 20 \log_{10} \left|\frac{E_{Ra,Rb}}{E_{Rax,Rbx}}\right|. \quad [98b]$$

This yields

$$\begin{aligned} XPD_{H,V} = & 10 \log_{10} \left(\frac{N_{\mp}}{D_{\mp}}\right) + f_{R'',''}(\phi_R) \\ & - f_{R'',''}(\phi_R) + G_{R',''} - G_{R'',''} \end{aligned} \quad [99a]$$

and

$$\mathrm{XPI}_{\mathrm{H,V}} = 10 \log_{10}\left(\frac{N_{\mp}}{D_{\pm}}\right) + F_{T}{}^{\prime,\prime\prime}(\phi_T)$$
$$- F_{T}{}^{\prime\prime,\prime}(\phi_T) + G_{T}{}^{\prime,\prime\prime} - G_{T}{}^{\prime\prime,\prime} \qquad [99b]$$

where the prime and double prime quantities above are in dB (see Eqs. [1] and [2] in the text).

Examples are now given. In the absence of rain, $p = \chi = 0$ and for $F' = F''$, $f' = f''$, and $G' = G''$, the above reduces to

$$\mathrm{CWI} = \mathrm{XPD} = \mathrm{XPI} = 10 \log_{10}$$
$$\times \left[\frac{(D_R - D_T{}^{-1})^2 - (D_R{}^2 - 1)(1 - D_T{}^{-2}) \sin^2\Theta}{(1 + D_R D_T{}^{-1})^2 + (D_R{}^2 - 1)(1 - D_T{}^{-2}) \sin^2\Theta}\right]. \qquad [100]$$

This gives the worst case for various δ phase values. This formula includes the reduction in isolation due to the following causes: (a) off-beam axis effects, (b) D_T, (c) D_R, and (d) misalignment effects. The more general formulas, Eqs. [96] and [97], include rain effects as well.

The attenuations in dB with respect to their values in free space are obtainable from the 11 and 22 elements. We find respectively for horizontal and vertical polarization:

$$(\mathrm{ATT})_{\mathrm{H,V}} = A_c - 10 \log_{10} N_{\mp} + 10 \log_{10}[(D_{Ra,b}$$
$$- D_{Ta,b}{}^{-1})^2 \cos^2\Theta + (1 - D_{Ra,b} D_{Ta,b}{}^{-1}) \sin^2\Theta]. \qquad [101]$$

Although results based on the above relations can readily be calculated, we limit our illustrations to those based on the random phase limit, given next.

(B) Random Phase Limit

We separate Eqs. [92a,b] into real and imaginary parts and obtain the square of their magnitudes. Cross-product terms involving the δ phases are zero unless the cosine or sine products are identical and then the contribution is ½. The results can be expressed in terms of $P_{s\pm}$ and $P_{c\pm}$ factors, defined as follows:

$$P_{c\pm} = \cos^2\Theta + p^2 \cos^2(2\tau + 2\xi + \Theta)$$
$$\pm 2p \cos\Theta \cos\chi \cos(2\tau + 2\xi + \Theta) \qquad [102a]$$

$$P_{s\pm} = \sin^2\Theta + p^2 \sin^2(2\tau + 2\xi + \Theta)$$
$$\pm 2p \sin\Theta \cos\chi \sin(2\tau + 2\xi + \Theta). \qquad [102b]$$

We obtain

$$|E_{Ra,Rb}|^2 = (\lambda/4\pi d)^2 G_{Ta,b} G_{Ra,b}$$
$$\times 10^{-A_c/10} F_{Ta,b}{}^2 f_{Ra,b}{}^2 N_{\mp}, \qquad [103a]$$

where now

$$N_{\mp} = D_{Ra,b}{}^2 P_{c\mp} + D_{Ta,b}{}^{-2} P_{c\pm} + P_{s\mp} + D_{Ra,b}{}^2 D_{Ta,b}{}^{-2} P_{s\pm}. \quad [103b]$$

Also

$$|E_{Rax,Rbx}|^2 = (\lambda/4\pi d)^2 G_{Tb,a} G_{Ra,b} \times 10^{-A_c/10} F_{Tb,a}{}^2 f_{Ra,b}{}^2 D_{\pm}, \quad [104a]$$

where now

$$D_{\pm} = P_{c\pm} + D_{Ra,b}{}^2 D_{Tb,a}{}^{-2} P_{c\mp} + D_{Ra,b}{}^2 P_{s\pm} + D_{Tb,a}{}^{-2} P_{s\mp}. \quad [104b]$$

It is interesting to note that Eqs. [102a] to [104b] are invariant if the signs of Θ and $\tau + \xi$ are changed simultaneously. The values of $XPD_{H,V}$ and $XPI_{H,V}$ are given again by Eqs. [98] and [99] with the new expressions for $N_{\mp}$ and $D_{\pm}$ in Eqs. [103b] and [104b]. The attenuations in dB with respect to their values in free space are

$$(ATT)_{H,V} = A_c - 10 \log_{10} N_{\mp} + 10 \log_{10}[(D_{Ra,b}{}^2 + D_{Ta,b}{}^{-2}) \cos^2\Theta + (1 + D_{Ra,b}{}^2 D_{Ta,b}{}^{-2}) \sin^2\Theta] \quad [105]$$

where A_c is defined in Eq. [95].

Graphs based on these relations are given in this paper. Next, we provide relations corresponding to the above for circular polarization.

A2.2 Theory for Circular Polarization

Circular polarization is insensitive to angular rotations of the polarization vector (imposed by Faraday rotation), misalignment, or off-axis rotation of the polarization. The angles χ and τ, associated with the mean position of the raindrops, remain to be considered. The matrix multiplication in Eq. [28] in the text can be denoted as:

$$\mathbf{M_R}^{-1} \cdot \mathbf{R}^{-1} \cdot \mathbf{V}^{-1} \cdot \mathbf{B} \cdot \mathbf{V} \cdot \mathbf{R} \cdot \mathbf{M_T} \equiv \Upsilon \left\{ \frac{\exp\left[-\frac{r}{2}(\alpha_1 + \alpha_2) + \frac{ir}{2}(\beta_1 + \beta_2) \right]}{[1 - p^2 \exp(-2i\chi)]^{1/2}} \right\} \quad [106]$$

From Eqs. [19] and [24], we note that

$$|\kappa_{a,b} C_T C_{Ra,b}^*| = \frac{\lambda}{4\pi d} (G_{Ta} G_{Ra,b})^{1/2} (F_{Ta}^2 + f_{Ta}^2)^{1/2} (F_{Ra,b}^2 + f_{Ra,b}^2)^{1/2} \quad [107a]$$

or

$$|\kappa_{a,b} C_T C_{Ra,b}^*| = \frac{\lambda}{4\pi d} (G_{Tb} G_{Ra,b})^{1/2} (F_{Tb}^2 + f_{Tb}^2)^{1/2} (F_{Ra,b}^2 + f_{Ra,b}^2)^{1/2}, \quad [107b]$$

depending on whether the wave is predominantly right-hand or left-hand circular. All F and f's here refer to the circular antenna patterns whereas previously they referred to linear antenna patterns. The four Υ elements are given by:

$$\begin{aligned}
\Upsilon_{11} &= m_{Ta} m_{Ra}^* + n_{Ta}^* n_{Ra} \\
&\quad - p e^{-i\chi} (m_{Ta} n_{Ra} e^{2i\tau} + n_{Ta}^* m_{Ra}^* e^{-2i\tau}) \\
\Upsilon_{22} &= m_{Tb}^* m_{Rb} + n_{Tb} n_{Rb}^* \\
&\quad + p e^{-i\chi} (m_{Tb}^* n_{Rb}^* e^{-2i\tau} + n_{Tb} m_{Rb} e^{2i\tau}) \\
\Upsilon_{12} &= n_{Tb} m_{Ra}^* - m_{Tb}^* n_{Ra} \\
&\quad - p e^{-i\chi} (n_{Tb} n_{Ra} e^{2i\tau} - m_{Tb}^* m_{Ra}^* e^{-2i\tau}) \\
\Upsilon_{21} &= m_{Ta} n_{Rb}^* - n_{Ta}^* m_{Rb} \\
&\quad - p e^{-i\chi} (n_{Ta}^* n_{Rb}^* e^{-2i\tau} - m_{Ta} m_{Rb} e^{2i\tau}).
\end{aligned} \quad [108]$$

It is more convenient to express m and n in terms of μ and σ through Eq. [23] in the text. We find:

$$\begin{aligned}
\Upsilon_{11,22} &= \cos(\mu_{Ta,b} - \mu_{Ra,b}) \cos(\sigma_{Ta,b} - \sigma_{Ra,b}) \\
&\quad \mp p \cos\chi \cos(\mu_{Ta,b} + \mu_{Ra,b}) \cos(2\tau - \sigma_{Ta,b} - \sigma_{Ra,b}) \\
&\quad - p \sin\chi \sin(\mu_{Ta,b} - \mu_{Ra,b}) \sin(2\tau - \sigma_{Ta,b} - \sigma_{Ra,b}) \\
&\quad + i[\mp \sin(\mu_{Ta,b} + \mu_{Ra,b}) \sin(\sigma_{Ta,b} - \sigma_{Ra,b}) \\
&\quad \pm p \sin\chi \cos(\mu_{Ta,b} + \mu_{Ra,b}) \cos(2\tau - \sigma_{Ta,b} - \sigma_{Ra,b}) \\
&\quad - p \cos\chi \sin(\mu_{Ta,b} - \mu_{Ra,b}) \sin(2\tau - \sigma_{Ta,b} - \sigma_{Ra,b})]
\end{aligned} \quad [109a]$$

$$\begin{aligned}
\Upsilon_{12,21} &= \mp \sin(\mu_{Tb,a} - \mu_{Ra,b}) \cos(\sigma_{Tb,a} - \sigma_{Ra,b}) \\
&\quad + p \cos\chi \sin(\mu_{Tb,a} + \mu_{Ra,b}) \cos(2\tau - \sigma_{Tb,a} - \sigma_{Ra,b}) \\
&\quad \mp p \sin\chi \cos(\mu_{Tb,a} - \mu_{Ra,b}) \sin(2\tau - \sigma_{Tb,a} - \sigma_{Ra,b}) \\
&\quad - i[\cos(\mu_{Tb,a} + \mu_{Ra,b}) \sin(\sigma_{Tb,a} - \sigma_{Ra,b})
\end{aligned}$$

$$+ p \sin\chi \sin(\mu_{Tb,a} + \mu_{Ra,b}) \cos(2\tau - \sigma_{Tb,a} - \sigma_{Ra,b})$$
$$\pm p \cos\chi \cos(\mu_{Tb,a} - \mu_{Ra,b}) \sin(2\tau - \sigma_{Tb,a} - \sigma_{Ra,b})]. \quad [109b]$$

The factors involving $\mu_T \pm \mu_R$ can be related to the ellipticities e_R and e_T (see Eqs. [21] and [22]) by

$$\sin(\mu_T \pm \mu_R) = \frac{e_R \pm e_T}{[(1 + e_T{}^2)(1 + e_R{}^2)]^{1/2}} \quad \text{and}$$
$$\cos(\mu_T \pm \mu_R) \frac{e_T e_R \mp 1}{[(1 + e_T{}^2)(1 + e_R{}^2)]^{1/2}} \quad [110]$$

and

$$\sin^2(\mu_T + \mu_R) - \sin^2(\mu_T - \mu_R) = \frac{4 e_T e_R}{(1 + e_T{}^2)(1 + e_R{}^2)}$$
$$= \frac{F_T{}^2 F_R{}^2 + f_R{}^2 f_T{}^2 - F_T{}^2 f_R{}^2 - F_R{}^2 f_T{}^2}{(F_T{}^2 + f_T{}^2)(F_R{}^2 + f_R{}^2)}. \quad [111]$$

In the following, we again adopt the two methods concerning the phases σ_T and σ_R, namely the limits of worst phase and of random phase.

(A) Worst Phase Limit

The worst clear weather isolation* is obtained by letting $\sigma_{Ta,b} = 0$ and $\sigma_{Ra,b} = \pi/2$ so that the axes of the received elliptical field are orthogonal to the axes of the transmitted field. From Eqs. [95], [106] to [109b] and [110] and Eq. [28] in the text, we obtain the following results for the square of the magnitude of the received electric field components:

$$|E_{Ra,Rb}|^2 = \left(\frac{\lambda}{4\pi d}\right)^2 G_{Ta,b} G_{Ra,b}\, 10^{-A_c/10}$$
$$\times (F_{Ta,b}{}^2 + f_{Ta,b}{}^2)(F_{Ra,b}{}^2 + f_{Ra,b}{}^2) N_{\mp}{}^c \quad [112a]$$

where

$$N_{\mp}{}^c = \sin^2(\mu_{Ta,b} + \mu_{Ra,b})$$
$$\pm 2p \cos\chi \cos 2\tau \sin(\mu_{Ta,b} - \mu_{Ra,b}) \sin(\mu_{Ta,b} + \mu_{Ra,b})$$
$$+ 2p \sin\chi \sin 2\tau \sin(\mu_{Ta,b} + \mu_{Ra,b}) \cos(\mu_{Ta,b} + \mu_{Ra,b})$$
$$+ p^2[\cos^2 2\tau \sin^2(\mu_{Ta,b} - \mu_{Ra,b}) + \sin^2 2\tau \cos^2(\mu_{Ta,b} + \mu_{Ra,b})]$$
$$= \{(e_{Ra,b} + e_{Ta,b})^2 \pm 2p \cos\chi \cos 2\tau (e_{Ra,b}{}^2 - e_{Ta,b}{}^2)$$

* In the presence of rain, the limit may in fact not represent the true worst case, especially for the right-hand circular polarization.

$$+ 2p \sin\chi \sin 2\tau(e_{Ra,b} + e_{Ta,b})(e_{Ta,b}e_{Ra,b} - 1)$$
$$+ p^2[\cos^2 2\tau(e_{Ra,b} - e_{Ta,b})^2 + \sin^2 2\tau(e_{Ta,b}e_{Ra,b} - 1)^2]\}$$
$$\times [(1 + e_{Ta,b}{}^2)(1 + e_{Ra,b}{}^2)]^{-1}. \qquad [112b]$$

Also

$$|E_{Rax,Rbx}|^2 = \left(\frac{\lambda}{4\pi d}\right)^2 G_{Tb,a}G_{Ra,b}\, 10^{-A_c/10}$$
$$\times (F_{Tb,a}{}^2 + f_{Tb,a}{}^2)(F_{Ra,b}{}^2 + f_{Ra,b}{}^2)D_{\pm}{}^c, \qquad [113a]$$

where

$$D_{\pm}{}^c = \cos^2(\mu_{Tb,a} + \mu_{Ra,b})$$
$$\pm 2p \cos\chi \cos 2\tau \cos(\mu_{Tb,a} - \mu_{Ra,b}) \cos(\mu_{Tb,a} + \mu_{Ra,b})$$
$$- 2p \sin\chi \sin 2\tau \sin(\mu_{Tb,a} + \mu_{Ra,b}) \cos(\mu_{Tb,a} + \mu_{Ra,b})$$
$$+ p^2[\cos^2 2\tau \cos^2(\mu_{Tb,a} - \mu_{Ra,b}) + \sin^2 2\tau \sin^2(\mu_{Tb,a} + \mu_{Ra,b})]$$
$$= \{(e_{Tb,a}e_{Ra,b} - 1)^2 \pm 2p \cos\chi \cos 2\tau(e_{Tb,a}{}^2 e_{Ra,b}{}^2 - 1)$$
$$- 2p \sin\chi \sin 2\tau(e_{Ra,b} + e_{Tb,a})$$
$$\times (e_{Tb,a}e_{Ra,b} - 1) + p^2[\cos^2 2\tau(e_{Tb,a}e_{Ra,b} + 1)^2$$
$$+ \sin^2 2\tau(e_{Ra,b} + e_{Tb,a})^2]\}/[(1 + e_{Tb,a}{}^2)(1 + e_{Ra,b}{}^2)]. \qquad [113b]$$

The values of $XPD_{r,l}$ and $XPI_{r,l}$ follow and are given by

$$XPD_{r,l} = 10 \log_{10}(N_{\mp}{}^c/D_{\mp}{}^c)$$
$$\pm 10 \log_{10}\left[\frac{10^{F_R'/10} + 10^{f_R'/10}}{10^{F_R''/10} + 10^{f_R''/10}}\right] + G_R{}'{}'' - G_R{}''{}' \qquad [114a]$$

$$XPI_{r,l} = 10 \log_{10}\left(\frac{N_{\mp}{}^c}{D_{\pm}{}^c}\right)$$
$$\pm \left[\frac{10^{F_T'/10} + 10^{f_T''/10}}{10^{F_T''/10} + 10^{f_T'/10}}\right] + G_T{}'{}'' - G_T{}''{}'. \qquad [114b]$$

The top signs refer to right-hand circular and the bottom signs to left-hand circular.

Examples are now given. In the absence of rain, $p = \chi = 0$ and for $e_{Ta} = e_{Tb}$, $e_{Ra} = e_{Rb}$, and $G_R{}' = G_R{}''$, the above reduces to

$$CWI = XPD = XPI = 10 \log_{10}[\tan^2(\mu_T + \mu_R)]$$
$$= 10 \log_{10}[(e_R + e_T)^2/(e_T e_R - 1)^2]$$
$$\approx 24.797 - 20 \log_{10}(e_T{}' + e_R{}')$$
$$+ 0.009594[(e_T{}')^2 + (e_R{}')^2 - 4e_T{}'e_R{}'], \qquad [115]$$

where the approximation holds for $e_T{}'/20 \ll 1$ and $e_R{}'/20 \ll 1$. For the situation of perfect antennas, $e_T{}' = e_R{}' = 0$, $e_T = e_R = 1$ and the relations

reduce to XPD = $-20 \log_{10} p$, (See McCormick and Hendry[2]) for circular polarization. It is independent of τ and the same for right and left-hand circular. The more general formulas in Eqs. [112] and [113] include all causes and, for this "worst phase limit," they depend on τ.

The attenuations in dB with respect to their values in free space are obtained from the 11 and 22 elements, thus:

$$(\mathrm{ATT})_{r,l} = A_c - 10 \log_{10} N_{\mp}{}^{c} + 10 \log_{10}[\sin^2(\mu_{Ta,b} + \mu_{Ra,b})]. \quad [116]$$

(B) Random Phase Limit

In Eqs. [109a,b] we sum the squares of the real and imaginary parts. Only products of identical σ factors, or factors independent of σ, contribute. The results simplify to the following expressions for $N_{\mp}{}^{c}$ and $D_{\pm}{}^{c}$ to be inserted into Eqs. [112a] and [113a], respectively:

$$N_{\mp}{}^{c} = \tfrac{1}{2}(1 + p^2) + \tfrac{1}{2}(1 - p^2)[\sin^2(\mu_{Ta,b} + \mu_{Ra,b}) - \sin^2(\mu_{Ta,b} - \mu_{Ra,b})] \quad [117a]$$

$$D_{\pm}{}^{c} = \tfrac{1}{2}(1 + p^2) - \tfrac{1}{2}(1 - p^2)[\sin^2(\mu_{Tb,a} + \mu_{Ra,b}) - \sin^2(\mu_{Tb,a} - \mu_{Ra,b})]. \quad [117b]$$

The results are identical for right and left-hand circular upon changing a and b and we can drop the $\pm$ subscripts. For example, using Eqs. [111] and [114b], XPI_c can be written in any one of the following forms:

$$\mathrm{XPI}_c = G_T' - G_T'' + 10 \log_{10}\left[\frac{F_{Ta}{}^2 + f_{Ta}{}^2}{F_{Tb}{}^2 + f_{Tb}{}^2}\right] + 10 \log_{10}\left\{\frac{1 + \left(\frac{1 - p^2}{1 + p^2}\right)[\sin^2(\mu_{Ta} + \mu_{Ra}) - \sin^2(\mu_{Ta} - \mu_{Ra})]}{1 - \left(\frac{1 - p^2}{1 + p^2}\right)[\sin^2(\mu_{Tb} + \mu_{Ra}) - \sin^2(\mu_{Tb} - \mu_{Ra})]}\right\}$$

$$= G_T' - G_T'' + 10 \log_{10}\left[\frac{F_{Ta}{}^2 + f_{Ta}{}^2}{F_{Tb}{}^2 + f_{Tb}{}^2}\right] + 10 \log_{10}\left[\frac{1 + \left(\frac{1 - p^2}{1 + p^2}\right)\frac{4 e_{Ta} e_{Ra}}{(1 + e_{Ta}{}^2)(1 + e_{Ra}{}^2)}}{1 - \left(\frac{1 - p^2}{1 + p^2}\right)\frac{4 e_{Tb} e_{Ra}}{(1 + e_{Tb}{}^2)(1 + e_{Ra}{}^2)}}\right]$$

$$= G_T' - G_T'' + 10 \log_{10}$$
$$\times \left[\frac{F_{Ta}{}^2 F_{Ra}{}^2 + f_{Ta}{}^2 f_{Ra}{}^2 + p^2(F_{Ta}{}^2 f_{Ra}{}^2 + f_{Ta}{}^2 F_{Ra}{}^2)}{f_{Tb}{}^2 F_{Ra}{}^2 + F_{Tb}{}^2 f_{Ra}{}^2 + p^2(f_{Tb}{}^2 f_{Ra}{}^2 + F_{Tb}{}^2 F_{Ra}{}^2)}\right]. \quad [118]$$

We note that the above results can also be derived from the case of linear polarization upon setting in Eqs. [103] and [104], $\tau + \xi = \pi/4$ and $\Theta = 0$, or $P_{c\pm} = 1$ and $P_{s\pm} = p^2$. However the interpretations for F and f differ, there referring to linear and here to circular antenna patterns. We also note that these results for the "random phase limit" are independent of the angles τ and χ.

The attenuations in dB relative to free space are given by

$$(\mathrm{ATT})_{r,l} = A_c - 10 \log_{10} N_{\mp}{}^c + 10 \log_{10}$$
$$\times [\tfrac{1}{2} \sin^2(\mu_{Ta,b} + \mu_{Ra,b}) + \tfrac{1}{2} \cos^2(\mu_{Ra,b} - \mu_{Ra,b})]. \quad [119]$$

For perfect antennas, $e' = 0$, $e = 1$, $\mu = \pi/4$, $N_{\pm}{}^c = 1$ and $(\mathrm{ATT})_{r,l} = A_c$. Thus A_c is the actual relative attenuation of circularly polarized waves in the presence of rain for perfect antennas.

References:

[1] C. W. Bostian, "Antenna and Path Interaction in Rain Depolarization," *IEEE/AP Int. Symp. Digest*, p. 392 (1974).

[2] G. C. McCormick and A. Hendry, "Method for Measuring the Anisotropy of Precipitation Media," *Electronics Lett.*, **9**, No. 10, p. 216, May 17 (1973).

[3] "Polarization Discrimination by Means of Orthogonal Circular and Linear Polarization," *CCIR Report 555*, March (1974).

[4] I. P. Shkarofsky and H. J. Moody, "Performance Characteristics of Antennas for Direct Broadcasting Satellite Systems Including Effects of Rain Depolarization," *RCA Review*, **37**, No. 3, p. 279, Sept. (1976).

[5] D. J. Fang, "Attenuation and Phase Shift of Microwaves Due to Canted Raindrops," *Comsat Tech. Rev.*, **5**, No. 1, p. 135, Spring (1975).

[6] T. Oguchi and Y. Hosoya, "Scattering Properties of Oblate Raindrops and Cross Polarization of Radio Waves Due to Rain (Part II): Calculations at Microwave and Millimeter Wave Regions," *J. Radio Res. Labs.* (Japan), **21**, No. 105, p. 191 (1974).

[7] P. A. Watson and M. Arbabi, "Semiempirical Law Relating Cross-Polarization Discrimination to Fade for Rainfall," *Electronics Lett.*, **11**, No. 2, p. 42, January 23 (1975).

[8] D. J. Fang and J. Jih, "A Model for Microwave Propagation Along an Earth-Satellite Path," *Comsat Tech. Rev.*, **6**, No. 2, p. 379, Fall (1976).

[9] "Reference Diagrams for Antennas to be used in Systems for Broadcasting from Satellites," *EBU Proposal Report (K3) 139—Rev. E. to CCIR*, Jan. (1976).

[10] K. G. Johannsen, "Ground Station Tracking of Dual Linearly Polarized Satellites," *Trans. IEEE*, **AES-11**, No. 6, p. 1333, Nov. (1975).

[11] D. J. Fang, "On the Determination of Cumulative Attenuation Statistics," *Comsat Tech. Mem. CL-45-76*, July 27 (1976).

[12] L. J. Ippolito, "Characterization of the CTS 12 and 14 GHz Communication Links," Presented at Int. Conf. on Communications, Phil., June (1976).

[13] S. I. Ghobrial and P. A. Watson, "Cross-Polarization During Clear Weather Conditions," IEE Publ. 98, *Propagation of Radio Waves at Frequenices Above 10 GHz*, p. 179, April (1973).

[14] W. L. Stutzman, C. W. Bostian, E. A. Manus, P. H. Wiley, and R. E. Marshall, "Results from the ATS-6 20 GHz Depolarization Experiment," 18th URSI General Assembly, Com II, Lima, Peru, Aug. (1975); see also, "ATS-6 Satellite 20 GHz Propogation Measurements at Low Elevation Angles," *Electronics Lett.*, **11**, Nos. 25/26, p. 635, Dec. 11, 1975.

[15] F. T. Tseng, "Effective Spectrum Utilization in Satellite Communications by Improving Antenna Radiation Performance," IEEE Publ. 75-CH-0971-2CSCB, Int. Conf. on Communications, p. 10–16 (1975).

[16] S. K. Barton, "Adaptive Compensation for Polarization Distortion in Systems Employing Orthogonal Polarization Frequency Re-Use," GEC-Marconi Electronics Ltd., Res. Labs., Chelmsford, Tech. Rep. MTR.74/66, Sept. (1974).

[17] S. K. Barton, "Adaptive Cancellation in Orthogonal Polarization Frequency Re-Use Satellite Communication Systems," IEEE Publ. 126, *Satellite Communication Systems Technology*, p. 195, April (1975).

[18] H. Kannowade, "Automatic Compensation of Cross Polarization Coupling in Communication Systems Using Orthogonal Polarizations," AIAA/CASI Paper 76-304, Montreal, April (1976).

[19] B. G. Evans and P. T. Thompson, "Use of Cancellation Techniques in the Measurement of Atmospheric Cross Polarization," *Electronics Lett.*, **9**, No. 19, p. 447, Sept. 20 (1973).

[20] B. G. Evans and P. T. Thompson, "Cross Polarization Due to Precipitation at 11.6 GHz," *J. Recherches Atmospheriques*, **8**, Nos. 1–2, p. 129, Jan.–June (1974).

[21] A. Paraboni and F. Rocca, "An Orthogonality Restoring System," Instituto Di Electrotechnica Ed Electtronica Del Politechnico Di Milano, Lab. di Com. Elettriche, Rep. 73-6, Oct. (1973).

[22] A. Attisani, C. Capsoni, and M. Mauri, "Rigenerazione di Orthogonalita in Sistemi Operanti in Frequency Re-Use per Diversita di Polarizzazione," *Alta Frequenza*, **42**, No. 12, p. 703 (1973).

[23] A. Attisani, C. Capsoni, and A. Paraboni, "Effects of Non-Spherical Hydrometeors on EM Propagation Through Atmospheric Precipitation," *J. Recherches Atmospheriques*, **8**, Nos. 1–2, p. 137, Jan.–June (1974).

[24] T. S. Chu, "Restoring the Orthogonality of Two Polarizations in Radio Communication Systems, I," *Bell System Tech. J.*, **50**, No. 9, p. 3063, Nov. (1971).

[25] T. S. Chu, "Restoring the Orthogonality of Two Polarizations in Radio Communication Systems, II," *Bell System Tech. J.*, **52**, No. 3, p. 319, March (1973).

Recent Papers by RCA Authors

Listing is alphabetical by name of primary author. For copies of reprints, the reader should contact the publication directly.

B. Abeles, "Effect of Charging Energy on Superconductivity in Granular Metals," **Phys. Rev. B,** Vol. 15, No. 5, p. 2828, March 1, 1977.

G. A. Alphonse, D. H. R. Vilkomerson, and B. Hurley, "Random Phase Diffuser for Ultrasonic Imaging Systems," **Ultrasound in Medicine,** Vol. 3B, p. 1823, 1977.

G. A. Alphonse, "The Wedged Transducer: An Improved Transducer Design for Broad Band Characteristics and Low Insertion Loss," **Ultrasound in Medicine,** Vol. 3B, p. 1851, 1977.

P. K. Baltzer, "Fun and Games with COSMAC," Presented at **ELECTRO 77,** p. 1, April 21, 1977.

E. Belohoubek, J. Cusack, J. Risko, and J. Rosen, "Microcomputer Controlled Radar and Display System for Cars," Soc. of Automotive Engrs., Intl. Automotive Engring. Congress and Exposition, Detroit, Mi., 2/28/77 to 3/4/77.

J. Blanc and M. S. Abrahams, "Early Growth of Silicon-on-Sapphire II. Models," **J. Appl. Phys.,** Vol. 47, No. 12, p. 5151, Dec. 1976.

W. J. Burke, "Crosstalk Noise from Multiple Thick-Phase Holograms," **J. Appl. Phys.,** Vol. 48, No. 2, p. 681, Feb. 1977.

C. Calderon, D. Vilkomerson, R. Mezrich, K. F. Etzold, B. Kingsley, and M. Haskin, "Differences in the Attenuation of Ultrasound by Normal, Benign, and Malignant Breast Tissue," **J. Clinical Ultrasound,** Vol. 4, No. 4, p. 249, 1976.

D. E. Carlson, "Amorphous Silicon Solar Cells," **IEEE Trans. on Electron Devices,** Vol. 24, No. 4, p. 449, April 1977.

D. E. Carlson and C. R. Wronski, "Solar Cells Using Discharge-Produced Amorphous Silicon," **J. Electronic Materials,** Vol. 6, No. 2, p. 95, 1977.

C. R. Carlson, R. W. Cohen, and I. Gorog, "Visual Processing of Simple Two-Dimensional Sine-Wave Luminance Gratings," **Vision Research,** Vol. 17, No. 3, p. 351, 1977.

R. B. Comizzoli, "Aluminum Corrosion in the Presence of Phosphosilicate Glass and Moisture," **RCA Review,** Vol. 37, No. 4, p. 483, Dec. 1976.

R. B. Comizzoli, "Surface and Bulk Electrical Conduction in Low-Deposition-Temperature Si_3N_4 and Al_2O_3 Films for Silicon Devices," **RCA Review,** Vol. 37, No. 4, p. 473, Dec. 1976.

V. L. Dalal and A. R. Moore, "Design Consideration for High-Intensity Solar Cells," **J. Appl. Phys.,** Vol. 48, No. 3, p. 1244, March 1977.

M. Ettenberg, "The Effect of Reabsorbed Radiation on the Minority Carrier Diffusion Length in GaAs," **Appl. Phys. Lett.,** Vol. 30, No. 4, p. 207, Feb. 1977.

M. Ettenberg, C. J. Nuese, and G. H. Olsen, "Interfacial Recombination Velocity Determination in $In_{.5}Ga_{.5}P/GaAs$," **J. Appl. Phys.,** Vol. 48, No. 3, p. 1288, March 1977.

M. T. Gale and K. Knop, "Color-Encoded Focused Image Holograms," **Appl. Optics,** Vol. 15, No. 9, p. 2189, Sept. 1976.

J. I. Gittleman and B. Abeles, "Comparison of the Effective Medium and the Maxwell-Garnett Predictions for the Dielectric Constants of Granular Metals," **Phys. Rev. B,** Vol. 15, No. 6, p. 3273, March 15, 1977.

J. Goel, "7.9–8.4 GHz GaAs MESFET. Amplifier," **Electronics Lett.,** Vol. 12, No. 19, p. 493, Sept. 16, 1977.

A. M. Goodman and C. E. Weitzel, "The Effects of Oxidation and Hydrogen Annealing on the Silicon-Sapphire-Interface Region of SOS," **Trans. on Electron Devices,** Vol. 24, No. 3, p. 1599, Dec. 1976.

A. M. Goodman, "Safe Operation of Capacitance Meters Using High Applied-Bias Voltage," **RCA Review,** Vol. 37, No. 4, p. 491, Dec. 1976.

P. D. Griffis and J. Shefer, "Kinescope Spot Size as it Relates to Picture Quality," **IEEE Trans. on Consumer Electronics,** p. 14, Feb. 1977.

W. E. Ham and S. S. Eaton, "Anomalous Electrical Gate Conduction in Self-Aligned MOS Structures," **Tech. Digest 1976 Intl. Electron Devices Meeting,** p. 324.

W. E. Ham, M. S. Abrahams, C.J. Bulocchi, and J. Blanc, "Direct Observation of the Structure of Thin, Commercially, Useful Silicon-on-Sapphire Films by Cross Section Transmission Electron Microscopy," **Electroch. Soc.,** Vol. 124, No. 4, p. 634, April 1977.

G. W. Hughes and R. J. Powell, "MOS Hardness Characterization and its Dependence Upon Some Process and Measurement Variables," **IEEE Trans. on Nuclear Science,** Vol. 23, No. 6, p. 1596, Dec. 1976.

W. Kern and R. B. Comizzoli, "New Method for Detecting Structural Defects in Glass Passivation Films," **J. Vacuum Sci. and Technology,** Vol. 14, No. 1, p. 32, Jan/Feb 1977.

H. Kressel, G. H. Olsen, and C. J. Nuese, "Visible GaAs $_{.7}$P $_{.3}$CW Heterojunction," **Appl. Phys. Lett.**, Vol. 30, No. 5, p. 249, March 1977.
I. Ladany and H. Kressel, "Visible CW (AlGa)As Heterojunction Laser Diodes," **1976 IEDM Tech. Digest**, p. 130.
S. Larach, B. Kingsley, and M. E. Haskin, "Rapid Clinical Echocardiographic Diagnosis of Myocardial Disease by A-Wave Quantification," **Ultrasound in Medicine**, Vol. 3A, p. 203, 1977.
H. W. Lehmann, L. Krausbauer, and R. Widmer, "Redeposition–A Serious Problem in RF-Sputter Etching of Structures with Micron Dimensions," **J. Vac. Sci. and Tech.**, Vol. 14, No. 1, p. 281, Jan/Feb 1977.
R. U. Martinelli, "The Effects of Emitter Impurity Concentration on the High-Current Gain of Silicon NPN Power Transistors," **1976 IEDM Tech. Digest**, p. 163.
D. Meyerhofer, "Optical Transmission of Liquid-Crystal Field-Effect Cells," **J. Appl. Optics**, Vol. 48, No. 3, p. 1179, March 1977.
R. Mezrich, "High Resolution, High Sensitivity Ultrasonic C-Scan Imaging Systems," **Ultrasound in Medicine**, Vol. 3B, p. 1845, 1977.
M. D. Miller, "Limitations on the Use of Platinum in Power Devices," **1976 IEDM Tech. Digest**, p. 492.
C. J. Nuese, "Diode Sources for 1.0 to 1.2 μm Emission," **1976 IEDM Tech. Digest**, p. 125.
C. J. Nuese, "III-V Alloys for Optoelectronic Applications," **J. Electronic Materials**, Vol. 6, No. 3, p. 253, 1977.
G. H. Olsen and D. J. Szostak, "High-Performance GaAs Photocathodes," **J. Appl. Phys.**, Vol. 48, No. 3, p. 1007, March 1977.
J. I. Pankove, "Phenomena Useful for Display," **1976 IEDM Tech. Digest**, p. 622.
D. H. Pritchard and T. M. Wagner, "Color Signal Inphase and Quadrature Distortion Measurement and Evaluation," **RCA Review**, Vol. 38, No. 1, p. 3, March 1977.
W. Rehwald, "Critical Behaviour of Strontium Titanate Under Stress," **Solid State Communications**, Vol. 21, p. 667, 1977.
A. Rosen, Pang-Ting Ho, and J. B. Klatskin, "Fabrication and Thermal Performance of a Novel TRAPATT Diode Structure," **IEEE Trans. on Electron Devices**, p. 160, Feb. 1977.
L. Schiff, "Compensatory Pre-emphasis," **RCA Review**, Vol. 37, No. 4, p. 515, Dec. 1976.
K. M. Schlesier and C. W. Benyon, "Processing Effects on Steam Oxide Hardness," **IEEE Trans. on Nuclear Science**, Vol. 23, No. 6, p. 1599, Dec. 1976.
E. K. Sichel and J. I. Pankove, "Thermal Conductivity of GaN, 25-360K," **J. Phys. Chem. Solids**, Vol. 38, p. 330, 1977.
T. Takahashi and O. Yamada, "Switching in Cadmium Boracite Single Crystals," **J. Appl. Phys.**, Vol. 48, No. 3, p. 1258, March 1977.
J. L. Vossen, J. J. O'Neil, Jr., O. R. Mesker, and E. A. James, "Extremely High Stress in Graded Interfacial Layers: Thin Films of Hf on Sapphire," **J. Vacuum Sci. and Tech.**, Vol. 14, No. 1, p. 85, Jan/Feb 1977.
R. Williams, "The Advancing Front of a Spreading Liquid," **Nature**, Vol. 266, No. 5598, p. 153, March 10, 1977.
C. R. Wronski, D. E. Carlson, R. E. Daniel, and A. R. Triano, "Electrical Properties of a-Si Solar Cells," **1976 IEDM Tech. Digest**, p. 76.
C. R. Wronski, "Electronic Properties of Amorphous Silicon in Solar Cell Operation," **IEEE Trans. on Electron Devices**, Vol. 24, No. 4, p. 351, April 1977.

Patents Issued to RCA Inventors First Quarter, 1977

January

J. B. Beck Magnetic Recording and Reproducing System with Tape-to-Head Speed Control (4,003,090)
R. R. Carbonetta, Jr. Gas Laser (4,001,720)
J. K. Clemens, J. S. Fuhrer, and M. D. Ross Defect Detection and Compensation Apparatus for Use in an FM Signal Translating System (4,001,496)
J. C. Coffin Photodetector Non-Responsive to Cerenkov Radiation (4,002,901)
B. Crowle Phase-Splitter Circuits (4,004,240)
R. H. Dawson Planar Voltage Variable Tuning Capacitors (4,005,466)
W. Den Hollander Synchronized and Regulated Power Supply (4,002,965)
R. C. Demmy Shadow Mask Cathode Ray Tube Shield (4,002,941)
W. F. Dietz Drive Cirucit for a Gate Semiconductor Device (4,001,607)
A. G. Dingwall Electrical Circuit (4,001,606)
J. G. Endriz and C. A. Catanese Modulation Mask for an Image Display Device (4,001,619)
J. G. Endriz Modulation Mask for an Image Display Device (4,001,620)
R. W. Etter Silver Plating Bath (4,003,806)
I. Gorog Optical Communication and Display System (4,004,078)
J. B. Halter Triangular Piezoelectric Transducer for Recording Video Information (RE29,113)
W. J. Hannan, E. M. Fulcher, R. D. Rhodes, and R. G. Saenz Credit Card Containing Electronic Circuit (4,004,133)
G. M. Harayda and W. M. Austin Heat-Sink Assembly for High-Power Stud-Mounted Semiconductor Device (4,004,195)
V. E. Hills and L. Wu Proximity Sensing Circuit (4,001,613)
P. Ho and A. Rosen Frequency Tunable Microwave Apparatus Having a Variable Impedance Hybrid Idler Circuit (4,005,372)
C. L. Jones, G. L. Hopkins, and W. L. Schulte, Jr. Time Division Multiplex Switching System (4,004,099)
P. W. Kaseman Electron Discharge Image Tube with Electrostatic Field Shaping Electrode (4,001,618)
E. O. Keizer Recording Apparatus and Methods for a Color Picture/Sound Record (4,005,474)
H. Khajezadeh High-Reliability Plastic-Packaged Semiconductor Device (4,001,872)
H. P. Kleinknecht and H. G. Kiess Apparatus for Making a Recording of an Electrostatic Charge Pattern (4,005,436)
A. Mack and C. C. Schweitzer Method and Apparatus for Compensation of Doppler Effects in Satellite Communication Systems (4,001,690)
R. U. Martinelli and H. Kressel Lateral Current Device (4,005,451)
J. E. Miller Full Range Correlator for Use in a Collision Avoidance System (4,003,050)
D. K. Morgan Keyed Comparator (4,004,158)
A. F. McDonie and C. M. Tomasetti Method of Sensitizing Electron Emissive Surfaces of Antimony Base Layers with Alkali Metal Vapors (4,002,735)
J. T. O'Neil, A. Pelios, A. H. Simon, and F. G. Nicki Article Carrying Coded Indicia (4,004,131)
D. L. Ross and L. A. Barton Method of Recording Information in Which the Electron Beam Sensitive Material Contains 4,4-BIS(3-Diazo-3-4-OXO-1-Naphthalene Sulfonyloxy)Benzil (4,005,437)
O. H. Schade, Jr. Dynamic Current Supply (4,004,244)
J. Schiess and T. E. Bart Color Correction Circuit for Video Recordings (4,001,876)
A. C. Sheng and M. E. Malchow Oscillator Circuit (4,001,723)
A. C. N. Sheng Amplifier with Current Gain Inversely Proportional to Transistor HFE (4,004,243)
T. F. Simpson Method of Measuring Color Purity Tolerance of a Color Display Tube (4,001,877)
H. Sorkin Liquid Crystal Devices (4,003,844)
P. Sterzer Electronic License Plate for Motor Vehicles (4,001,822)
F. Sterzer and G. S. Kaplan Dual Mode Automobile Collision Avoidance Radar (4,003,049)
D. R. Tshudy and T. W. Edwards Method of Selective Growth of Microcrystalline Silicon (4,004,954)
J. L. Vossen, Jr., F. R. Nyman, D. G. Fisher, and G. F. Nichols Metal Coating for Video Discs (4,004,080)
C. C. Wang, T. C. Lausman, and R. F. Bates Photosensitive Camera Tube Target Primarily of Lead Monoxide (4,001,099)

P. K. Weimer Signal Processing Circuits for Charge-Transfer Image-Sensing Arrays (4,001,501)
P. K. Weimer Charge Transfer Color Images (4,001,878)
C. F. Wheatley, Jr. Apparatus for Supplying Symmetrically Limited Bidirectional Signal Currents (4,004,242)
C. T. Wu Self-Clocking, Error Correcting Low Bandwidth Digital Recording System (4,003,085)
B. Zuk ECL Switching Circuit for Producing Noncomplementary, Time Coincident Signals (4,001,608)

February

L. R. Avery Automatic Noise Gate for a Synchronizing Signal Amplifier (4,008,370)
W. Bohringer Voltage Regulator for a Deflection System (4,009,426)
J. R. Burns Charge-Coupled Memory System (4,009,473)
W. L. Cable Spacecraft Structure (4,009,851)
W. J. Derenbecher, Jr. Blanking Generator for PAL Sync Signals (4,009,487)
F. R. Dimeo and W. J. Bachman Antenna Construction (4,010,473)
A. G. Dingwall and B. D. Rosenthal Current Mirror Amplifier (4,010,425)
A. G. Dingwall and B. D. Rosenthal Constant Current Supply (4,009,432)
B. W. Faughnan and R. S. Crandall Electrochromic Device Having a Dopant Therein to Improve its Color Center Absorption Characteristics (4,009,935)
R. D. Faulkner and R. E. McHose Phototube Having Improved Electron Collection Efficiency (4,006,376)
A. H. Firester Polarization-Selective Laser Mirror (4,009,933)
A. H. Firester Optical Element for a Laser (4,011,524)
J. R. Hall and J. J. Lyon Correlator to Reduce Bin Straddle in a Collision Avoidance System (4,008,471)
H. E. Haslau and W. E. Rigsbee Coil Winding Machine (4,007,881)
K. G. Hernqvist Laser Alignment System (4,010,363)
K. G. Hernqvist Ultra-Violet Gas Laser (4,008,445)
E. O. Johnson Electronic Timepiece (4,007,583)
H. C. Johnson Stabilizing and Calibration Circuit for FM-CW Radar Ranging System (4,008,475)
A. J. Leidich Cascaded Transistor Amplifier Stages (4,007,427)
P. A. Levine Smear Reduction in CCD Imagers (4,010,319)
M. P. Mills Method of Fabricating Large Area, High Voltage Pin Photodiode Devices (4,009,058)
J. Ollendorf and F. J. Cestone Semiconductor Wafer Chuck with Built-in Standoff for Contactless Photolithography (4,006,909)
H. L. Pinch, B. Abeles, and J. I. Gittleman High Resistance Cermet Film and Method of Making the Same (4,010,312)
E. S. Poliniak, R. J. Himics, and H. Wielicki Olefin-SO2 Copolymer Film Adhesion to a Substitute (4,007,295)
R. M. Rast Programming Unit for a Television Tuning Phase Locked Loop (4,009,439)
G. H. Riddle Probe Forming Electron Optical Column Having Means for Examining Magnified Image of the Probe Source (4,010,318)
P. H. Robinson and R. S. Ronen Method of Treating Semiconductor Device to Improve its Electrical Characteristics (4,007,297)
L. R. Salvatore Transistor Circuits (4,010,418)
D. J. Sauer Charge-Coupled Device Input Circuits (4,010,485)
O. H. Schade, Jr. Current Amplifier (4,008,441)
H. G. Seer, Jr. Negative Color Film Mask Correction (4,009,489)
E. S. Thall CRT with Thermally-Set Getter Spring (4,006,381)
M. H. Woods and R. Williams Method of Treating a Layer of Silicon Dioxide (4,007,294)

March

O. Ben-Dov Circularly Polarized, Broadside Firing, Multihelical Antenna (4,011, 567)
W. Den Hollander High Voltage Regulation System (4,013,923)
N. Disanti and F. Oster Narrow-Band Eight-Phase Modem (4,011,407)
G. E. Eiwen Method for Devacuating a Vacuum Tube (4,010,991)
A. H. Firester Optical Element for a Laser (4,011,524)
R. A. Gange Holographic Recording Medium (4,012,253)
A. Garcia Directional Power Detector for Propagating Waves (4,011,529)

D. M. Gavrilovic Liquid Crystal Compounds and Electro-Optic Devices Incorporating Them (4,013,582)
W. E. Ham Edgeless Transistor (4,015,279)
A. G. Lazzery Liquid Crystal Module (4,012,117)
A. W. Levine and M. Kaplan Electron Beam Recording Medium Comprising 1-Methylvinyl Methyl Ketone (4,012,536)
H. L. Pinch and H. I. Moss Video Disc Stylus (4,013,830)
W. R. Roach Deformable Mirror Light Valve and Method of Operating the Same (4,013,345)
A. D. Robbi Low Energy Switching Circuit (4,011,464)
A. D. Robbi Variable Range Automotive Radar System (4,011,563)
J. R. Sandercock High Resolution, High Contrast Fabry-Perot Spectrometer (4,014,614)
O. H. Schade, Jr. Voltage Regulator Circuit with FET and Bipolar Transistors (4,012,684)
I. Shidlovsky Hafnium Pyrophosphate Phosphors and Methods of Preparation (4,014,813)
M. Vanrenssen and M. H. Wardell, Jr. Electron Tube Socket Having Spring-Wire Contacts (4,012,094)
H. A. Wittlinger Ground Fault and Neutral Fault Detection Circuit (4,012,668)
M. H. Woods and R. Williams Method of Radiation Hardening Semiconductor Devices (4,014,772)

AUTHORS

David E. Carlson received the B.S. in Physics from Rennsselaer Polytechnic Institute in 1963 and the Ph.D. in Physics from Rutgers University in 1968. He worked as a Research and Development Physicist at the U. S. Army Nuclear Effects Laboratory, Engewood Arsenal, Maryland, in 1968 and 1969. He received the Bronze Star Medal in 1969 while serving in Vietnam as a U. S. Army Captain in charge of the Pleiku ICS Communications Site. In 1970 he joined RCA Laboratories where he has worked in the areas of ion motion in glasses and insulators, glow-discharge deposition of films, and thin film photovoltaic devices. Dr. Carlson received an RCA Laboratories Outstanding Achievement Award in 1973, for his work on ion depletion of glasses and one in 1976 for the development of amorphous silicon devices. He was awarded the Ross Coffin Purdy Award by the American Ceramic Society "in recognition of his outstanding contribution to ceramic literature in the year 1974." He was appointed Group Head, Photovoltaic Device Development in 1977.

Dr. Carlson is a member of the American Physical Society, the American Ceramic Society, the Electrochemical Society, and Sigma Xi.

Jitendra Goel received the B.S. degree in Physics in 1961 from Agra University and the B.E. degree in Communications in 1964 from the University of Roorkee, India. From 1964 to 1969, Mr. Goel was involved with radio receiver design at Murphy India Ltd., and with communication circuits design with Brown Boveri Corporation. From 1969 to 1971, he attended the University of Lowell, Mass. on a teaching fellowship and also received the M.S.E.E. in 1971. In 1971 he joined Tucker Electronics as a chief engineer and was responsible for the development of the new products and test setups for instruments. In 1973 he joined RCA Laboratories where he is presently engaged in the study and development of GaAs MESFETs and amplifier circuits. He is currently working toward a Ph.D. degree in Electrical Engineering at Rutgers University.

Mr. Goel is a Member of the Institute of Electrical and Electronics Engineers

Sheng T. Hsu received the B.S. degree in electrical engineering from National Taiwan University, Taipei, Taiwan, in 1958; the M.S.E.E. degree from National Chiao-Tung University, Hsienchu, Taiwan, in 1960 and the Ph.D. degree in electrical engineering from the University of Minnesota, Minneapolis, in 1966. From 1966 to 1970, he was with Fairchild Semiconductor Research and Development Laboratory, Palo Alto, California, as a Member of the Technical Staff. From 1970 to 1972, he was an Assistant Professor of the Department of Electrical Engineering, University of Manitoba, Winnipeg, Man., Canada. He is now a staff member of RCA Laboratories, Princeton, N. J., working on semiconductor devices and integrated circuit technologies.

Myung-Ki Lee graduated in 1967 from Hanyang University, Seoul, Korea, with a B.S. degree and first class honor in electrical engineering. In 1969 and 1973, he obtained M.S. and Ph.D. degrees in electrical engineering, conducting his research at the Ionosphere Research Laboratory, Pennsylvania State University, in the field of radio wave propagation in the ionosphere. After six months' research work as a post doctoral associate, he joined the Fairchild Space and Electronics Company, Germantown, Maryland, where he worked on various interference analysis such as intermodulation distortion due to TWT nonlinearity, cross talk, intermodulation noise due to transmission deviation, PSK signal power spectrum spread, and performance of PSK system in gaussian noise and intersymbol interference. In 1974 he joined RCA American Communications, Inc., where he has been contributing to the development of the RCA Satcom system. His main interest in the development of the RCA Satcom system is to define and evaluate the crosspolarization performance of spectrum reuse system. He has participated in various studies, such as that on transponder loading to meet the Alaskan traffic requirement and a study related to the RCA Satcom TV distribution system, e.g., for CATV. He is currently involved in the study of multiple video transmission per transponder.

Daniel D. Mawhinney received his B.E.E. from the Polytechnic Institute of Brooklyn in 1957, and his M.S.E.E. from the Newark College of Engineering in 1965. He was in military service from 1948 to 1952. In 1952 Mr. Mawhinney joined the RCA Microwave Tube Operations Department where he contributed to the development of special microwave equipment used for the test and evaluation of microwave tubes. In 1959 he became Engineering Leader of Microwave Equipment Design with the responsibility for the planning and development of test equipment as part of an integrated manufacturing system. In 1965 he became Engineering Leader of Solid State Systems Development and was assigned to the Lunar Module (LM) team engaged in the design and fabrication of solid state multiplier units. He developed a tunnel diode amplifier system for a commercial aircraft radar system and worked on other tunnel diode and parametric amplifier devices. Later, as Manager of Solid State Product Design, he was

responsible for product development of various types of microwave solid-state devices including transferred electron oscillators, ferrite components, and microwave integrated circuits. In this position, he directed the design of a series of a solid-state TR switches for a high-reliability commercial radar system, an integrated circuit version of a meteorological telemetry oscillator, and an X-band transferred electron oscillator for a lightweight military doppler radar system, and several voltage controlled oscillator subsystems. In 1975 he was transferred to the Microwave Technology Center at RCA Laboratories in Princeton, where he has continued to work on advanced VCO subsystems, hyperabrupt varactor tuned VCO's, frequency memory systems for ECM applications, and FET discriminators.

Mr. Mawhinney is a member of the IEEE and a licensed professional engineer in the State of New Jersey.

Louis S. Napoli received his B.S. in 1959 and the M.S. in 1961 in Electrical Engineering, both from Rutgers University. He has pursued further studies in plasma physics at Princeton University and in electro-physics at the Polytechnic Institute of Brooklyn. Since joining the technical staff of RCA Laboratories in June 1959 he has specialized in research relating to microwave phenomena in gaseous plasmas, solid-state microwave devices, and microwave integrated circuits. He is presently Head of the Microwave Components Technology Group in the Microwave Technology Center at RCA Laboratories. His work in collaboration with Dr. George Swartz on amplification at 24 Gc by the interaction of an electron beam with a cesium plasma was cited by industrial Research Magazine as one of the 100 most important achievements in 1963. He is the recipient of RCA Laboratories Achievement Awards in 1963, 1965 and 1968.

Mr. Napoli is a member of Sigma Xi, IEEE, Tau Beta Pi, and Eta Kappa Nu

Jacques I. Pankove obtained his B.S. (1944) and M.S. (1948) degrees from the University of California and a doctorate from the University of Paris (1960). He joined the RCA Laboratories in 1948 where he has made many contributions to the understanding, technology and evolution, of various semiconductor devices, including large-area photocells, transistors, tunnel diodes, injection lasers and LED's. Dr. Pankove, a Fellow of RCA's Technical Staff, is a member of the American Association for the Advancement of Science, Sigma Xi, and Fellow of both the American Physical Society and Institute of Electrical and Electronics Engineers. He is an associate editor of the Journal of Quantum Electronics and a member of the editorial board of Solid State Electronics.

Arye Rosen received the B.S.E.E. degree cum laude from Howard University in 1963 and the M.Sc.E. degree from Johns Hopkins University (which he attended on a Gillman Fellowship) in 1965. He was an instructor at Johns Hopkins during 1963–64. From 1964 to 1967, Mr. Rosen was concerned with systems design at General Telephone and Electronics International, and with antenna and circuit design at Channel Master, Inc., and American Electronics Laboratories, Inc. In 1967 Mr. Rosen joined RCA Laboratories where he is presently engaged in the study and development of microwave circuits and devices. He is the recipient of a 1972 RCA Laboratories Outstanding Achievement Award for a team effort in the development of S-band Trapatt amplifiers. From 1970 to 1971, on leave of absence from RCA, Mr. Rosen engaged in research in the Division of Cardiology at Jefferson Medical College in Philadelphia, Pa., where he received the degree of M.Sc. in Physiology.

Mr. Rosen is a member of Tau Beta Pi, Sigma Xi, and the Association of Professional Engineers of British Columbia.

Issie P. Shkarofsky graduated in 1952 from McGill University, Montreal with a B.Sc. degree and first class honours in physics and mathematics. In 1953 he obtained his M.Sc. degree, conducting his research at the Eaton Electronics Research Laboratory, McGill University, in the fields of microwave optics and antennas. He then joined the microwave tube and noise group at the Eaton Electronics Research Laboratory, McGill University, and received his Ph.D. degree in 1957 with a thesis on modulated electron beams in space-charge-wave tubes and klystrons. After graduation, he joined the Research Laboratories of RCA Limited, Montreal, where he participated in research on microwave diffraction, millimetre waves, obstacle gain, laser applications, electromagnetic wave interaction with plasmas, plasma kinetics, and plasmas in space. From 1973 until 1977, he was R&D Fellow at the RCA Research and Development Laboratories. In the field of plasma and space studies his particular interest has been in the following topics: plasma transport coefficients, collisional effects in plasmas (slightly, partially and strongly ionized), Boltzmann and Fokker-Planck theory and appropriate expansions, bremsstrahlung, magneto-hydrodynamics, re-entry plasma physics, generalized Appleton-Hartree equation for the ionosphere, laboratory simulation of geophysical phenomena such as the interaction between the solar wind and the magnetosphere and the sheaths around satellites, cyclotron harmonic resonances and related dispersion effects, diagnostics of plasmas by laser scattering, nonlinear mixing of plasma modes, the accuracy of Langmuir probes on satellites, VLF sheath admittance of antennas in the ionosphere, high power laser interaction with matter, turbulence (such as radar scattering from turbulent plasmas, laser propagation through a turbulent atmosphere, microwave propagation through a turbulent plasma, hydrodynamic flow turbulence, and arc turbulence), probe diagnostics of anisotropic laser plasmas, spacecraft charging/arcing/radiation, rain depolarization in satellite communications, and fusion, having been a co-leader of the Task Force on Toroidal Machines for Project Fusion Canada.

Dr. Shkarofsky is a member of the Canadian Association of Physicists and its Plasma Physics Division, of the American Physical Society and its Plasma Physics Division, and of the American Geophysical Union. He has served on the National Research Council Advisory Committee on Physics, and as professeur invité du Centre de Recherche INRS—Energie, Université du Québec.

David L. Staebler received his B.S.E.E. with distinction, and M.S.E.E. degree from the Pennsylvania State University in 1962 and 1963, respectively, and his Ph.D. in Electrical Engineering from Princeton University in 1970. His doctoral research involved optical studies of photochromic CaF_2, and resulted in the identification of an important class of photochromic color centers. In 1963, he joined RCA Laboratories where he has contributed to the understanding and development of photochromic and electrochromic phenomena and hologram storage in electro-optic crystals. He is presently involved in the study of amorphous silicon solar cells. He received RCA achievement awards for team research in photochromic materials (1967) and in hologram storage media (1972) and was a visiting professor at the Instituto de Fisica e Quimica de Sao Carlos, Brazil, during a leave of absence from RCA Laboratories (1974–1975).

Dr. Staebler is a member of Eta Kappa Nu, Tau Beta Pi, IEEE, and the AAAS.

Herbert J. Wolkstein received his BSEE in 1953 and has completed his work toward an MSEE at the Newark College of Engineering. From 1948 to 1955, he worked in the Research Laboratories of National Union Electric Corporation as Project Engineer on the design of special-purpose beam-deflection and computer-switching tubes. He joined RCA's Microwave Tube Operations Department in 1955 where he designed and developed traveling-wave tubes. In 1958 he became Engineering Leader in charge of the development of low-noise TWTs. He was promoted to the position of Manager, TWT Design and Development in 1961. In 1964 he directed a group in advanced development and application work on TWTs and Pencil Tubes and in 1965 became Manager of TWT Product Design. In 1972 he was named Manager of the Advanced Programs and Application Engineering group, a position he held until 1975, when he joined the Microwave Technology Center, RCA Laboratories, Princeton, N. J. Mr. Wolkstein has made many contributions to the design of TWTs, periodic permanent-magnet focusing structures, slow-wave structures, and electron guns. He was particularly instrumental in the development of ultra low-noise TWTs, memory-storage tubes, and the RCA tri-coupler and miniature traveling wave tubes for phased arrays.

Mr. Wolkstein is a member of the IEEE, the Professional Group on Electron Devices, and the Professional Group of Microwave Theory and Techniques.

Christopher R. Wronski obtained his B.Sc. (First Class Honors) in 1963 and Ph.D. in 1963 in Physics, both at Imperial College, London University. His thesis was concerned with the study of melting phenomena in submicron crystallites. From 1963 to 1966, Dr. Wronski was Research Scientist at 3M Research Laboratories in St. Paul, Minnesota. His work there was in the area of photoconductivity in thin films. Since joining RCA Laboratories in 1966, Dr. Wronski has been engaged in areas related to semiconductor cold cathodes, television pick-up tubes, and photovoltaic devices. He has worked in the area of heterojunction vidicons formed between a semiconductor or photoconductor and thin insulating films or granular metals. His work involved the characterization of these photosensitive heterojunctions and the understanding of their operation as vidicons, as well as the development of novel semiconductor–insulator vidicons, an improved antimony trisulfide vidicon, and a granular metal–semiconductor vidicon. Since 1974 Dr. Wronski has been involved in the development of thin film ($\sim$1 μm thick) photovoltaic cells. After working on the development of an $\sim$1% efficient polycrystalline CdSe/thin insulator/metal solar cell, he has been engaged in the development of amorphous silicon solar cells. He has carried out investigations of amorphous silicon and its junction properties, working toward a fundamental understanding of these photoconductive solar cells and the novel cell parameters that determine their characteristics.

Dr. Wronski is a member of the American Physical Society.

Peter J. Zanzucchi received his B.S. honors degree in chemistry from Le Moyne College, Syracuse, N. Y., in 1963 and his M.S. and Ph.D. degrees in chemistry from the University of Illinois in 1965 and 1967, respectively. Since 1967 he has been a member of the Materials Research Laboratory at the RCA Laboratories. He is engaged in the identification of molecular species by instrumental methods, in particular, optical methods. Since 1969 he has been investigating the molecular properties of materials in thin film form, e.g., a-Si solar cell material, using primarily optical measurements in the infrared. Most recent work concerns the application of light scattering techniques, such as Raman scattering, to the characterization of the molecular properties of semiconductor and related materials.

Dr. Zanzucchi is a member of the Optical Society of America, the Electrochemical Society and the ASTM, serving on Committee E-2 on Emission Spectroscopy. He is currently on the board of editors for the journal *Chemical Instrument*.